Chromospheric modeling of M-dwarf stars

Dissertation
zur Erlangung des Doktorgrades
an der Fakultät für Mathematik, Informatik und Naturwissenschaften
des Fachbereichs Physik
der Universität Hamburg

vorgelegt von

Dominik Hintz

Hamburg
2020

Gutachter der Dissertation:	Prof. Dr. Jürgen H. M. M. Schmitt Prof. Dr. Travis Barman
Zusammensetzung der Prüfungskommission:	Prof. Dr. Jochen Liske Prof. Dr. Jürgen H. M. M. Schmitt Prof. Dr. Peter H. Hauschildt Prof. Dr. Robi Banerjee Prof. Dr. Dieter Horns
Vorsitzender der Prüfungskommission:	Prof. Dr. Jochen Liske
Datum der Disputation:	29.10.2020
Vorsitzender Fach-Promotionsausschusses PHYSIK:	Prof. Dr. Günter Hans Walter Sigl
Leiter des Fachbereichs PHYSIK:	Prof. Dr. Wolfgang Hansen
Dekan der Fakultät MIN:	Prof. Dr. Heinrich Graener

Abstract

Since the discovery of the solar activity cycle by Schwabe in the 19th century, the research of stellar activity has made enormous advances. However, since the Sun is the only star whose surface we can resolve in detail, solar-like activity phenomena in stars other than the Sun can mostly be observed indirectly through photometric and spectroscopic observations. These activity phenomena, such as starspots and plages, are attributed to different layers of the stellar atmosphere. Between the photosphere and corona, the chromosphere constitutes the part of a stellar atmosphere where temperature starts to outwardly increase again, while density strongly declines. It is very sensitive to changes in magnetic activity, as material in the chromosphere appears to be strongly connected to the magnetic field lines. Therefore, spectral lines arising in the chromosphere represent reliable indicators of stellar activity. Constituting the cool end of the main sequence, M-dwarf stars have become a focus of astrophysical research, as they are a spectral type exhibiting strong activity features. Modeling chromospheric temperature structures of M dwarfs allows us to approach the nature and behaviour of stellar atmospheres by comparing synthetic spectral lines to observed lines.

The first part of this thesis is dedicated to the creation of one-dimensional PHOENIX model chromospheres that are able to simultaneously reproduce the three chromospheric lines of Na I D_2, Hα, and the bluest Ca II infrared triplet line in CARMENES observations in an adequate manner. The modeling is conducted for a sample of 50 M2–3 V stars observed by the CARMENES spectrograph and the temperature structures of the model chromospheres follow the one-dimensional approach of the classical structure of the average quiet Sun. In the chromosphere models, arbitrarily linear temperature rises are attached to an underlying photosphere model. A parameterization of the temperature structure is then used to divide the upper atmosphere into three different sections: the lower and upper chromosphere and the lower transition region. The free parameters are adjusted to fit the investigated chromospheric lines. While inactive stars of the stellar sample are well fitted by single-model fits, active stars need to be modeled by linear combinations of an inactive and an active model component. The latter method also accesses the possibility to derive surface filling factors. Investigating the variable stars of the stellar sample by applying linear-combination fits shows that increasing activity states lead to a stronger contribution of the active model component.

The second part deals with a model investigation of the behavior of the He I infrared (IR) line at 10 833 Å in the same stellar sample as in the first part of this thesis. Previous best-fit models also predict absorption within the He I IR line. Furthermore, the existing model set is extended by models of systematic series varying in activity to examine the line in terms of activity states more precisely. The He I IR line is very sensitive to variations in stellar activity. The formation of He I IR absorption strongly depends on the photoionization and recombination mechanism and its evolution with increasing activity is similar to that of the Hα line. The research of the He I IR line strength as a function of the extreme ultraviolet radiation reveals that increasing activity first strengthens the absorption and eventually leads the line to fill in due to an increasing contribution of collisional excitation.

The studies performed in the course of this thesis indicate that one-dimensional PHOENIX models of M-dwarf chromospheres with parameterized temperature structures are capable of reproducing shapes and strengths of spectral lines arising in the chromosphere. Furthermore, these models offer the possibility to access detailed information about line formation mechanisms by simulating variations in magnetic activity.

Zusammenfassung

Seit der Entdeckung des solaren Aktivitätszyklus von Schwabe im 19. Jahrhundert hat die Erforschung stellarer Aktivität enorme Fortschritte gemacht. Da die Sonne der einzige Stern ist, den wir detailliert auflösen können, können sonnenartige Aktivitätsphänomene auf anderen Sternen indessen hauptsächlich indirekt durch photometrische und spektroskopische Beobachtungen beobachtet werden. Diese Aktivitätsphänomene, wie Sternflecken und Plages, werden unterschiedlichen Schichten einer Sternatmosphäre zugeschrieben. Zwischen Photosphäre und Korona stellt die Chromosphäre den Teil der Sternatmosphäre dar bei der sich die Temperatur nach außen wieder erhöht, während die Dichte stark abnimmt. Sie ist sehr sensitiv auf Veränderungen der magnetischen Aktivität, da sich das Chromosphärenmaterial als eng gebunden an die Magnetfeldlinien erweist. Daher repräsentieren Spektrallinien, die in der Chromosphäre entstehen, zuverlässige Indikatoren stellarer Aktivität. M-Zwerg Sterne befinden sich am kühlen Ende der Hauptreihe und sind in einen Fokus astrophysikalischer Forschung gelangt, weil sie einem Spektraltyp mit starken Aktivitätseigenschaften angehören. Modelle chromosphärischer Temperaturstrukturen von M Zwergen erlauben es sich der Natur und dem Verhalten von Sternatmosphären mithilfe von Vergleichen zu beobachteten Spektrallinien anzunähern.

Der erste Teil dieser Arbeit widmet sich der Erzeugung von eindimensionalen PHOENIX Modellchromosphären, die dazu in der Lage sind, simultan die drei chromosphärischen Linien von Na I D_2, Hα und der blauesten Linie des Ca II Infrarot-Tripletts in CARMENES Beobachtungen adäquat zu reproduzieren. Die Modelle werden für eine Auswahl von 50 M2 – 3 V Sternen erstellt, die von CARMENES beobachtet wurden. Die Temperaturstrukturen der Modellchromosphären folgen dem eindimensionalen Ansatz der klassischen Struktur der durchschnittlich ruhigen Sonne. Beliebige lineare Temperaturanstiege werden in den Chromosphärenmodellen auf ein darunter liegendes Photosphärenmodell aufgesetzt. Eine Parametrisierung der Temperaturstruktur wird benutzt, um die obere Atmosphäre in drei unterschiedliche Sektionen zu unterteilen: Die untere und obere Chromosphäre sowie die untere Transition Region. Die freien Parameter werden angepasst, um die untersuchten chromosphärischen Linien zu reproduzieren. Während die Inaktiven der untersuchten Sterne gut durch Einzelmodelle repräsentiert werden, ist es notwendig die aktiven Sterne durch Linearkombinationen aus jeweils einer inaktiven und einer aktiven Modellkomponente zu modellieren. Letztere Methode ermöglicht es auch Füllfaktoren der Sternoberfläche abzuleiten. Die Untersuchung der variablen Sterne aus der Stichprobe unter Anwendung von Linearkombinationen von Modellen zeigt, dass ansteigende Aktivitätszustände zu einem stärkeren Beitrag der aktiven Modellkomponente führen.

Der zweite Teil der Arbeit beschäftigt sich mit einer Modelluntersuchung des Verhaltens der He I Infrarot (IR) Linie bei 10 833 Å in derselben Auswahl an Sternen wie im ersten Teil der Arbeit. Die Modelle mit der besten Übereinstimmung zu den beobachteten Sternen aus dem vorherigen Teil sagen ebenfalls Absorption innerhalb der He I IR Linie vorher. Darüberhinaus wird der existierende Modellsatz durch Modelle mit systematischen Modellserien erweitert, die in ihrer Aktivität variieren, um die Linie genauer im Hinblick auf Aktivitätszustände zu untersuchen. Die He I IR Linie ist sehr sensitiv auf Aktivitätsveränderungen in Sternen. Die Bildung von He I IR Absorption hängt stark vom Photoionisations- und Rekombinationsmechanismus ab. Die Entwicklung der He I IR Linie mit zunehmender Aktivität ist mit derjenigen der Hα Linie vergleichbar. Die Untersuchung der He I IR Linienstärke als Funktion der extremen Ultraviolettstrahlung offenbart, dass steigende Aktivität die Absorption zunächst verstärkt und die Linie schließlich auffüllt aufgrund eines ansteigenden Beitrags der Kollisionsanregung.

Die im Laufe dieser Arbeit durchgeführten Studien zeigen, dass eindimensionale PHOENIX Modelle von M-Zwerg Chromosphären mit parametrisierten Temperaturstrukturen dazu fähig

sind, die Formen und Stärken von Spektrallinien aus der Chromosphäre zu reproduzieren. Außerdem bieten diese Modelle die Möglichkeit an detaillierte Informationen über Formationsmechanismen von Spektrallinien mithilfe von Simulationen unterschiedlicher magnetischer Aktivität zu gelangen.

Contents

Chapter 1

Introduction

The Sun and other stars have fascinated mankind from the very beginning. Since we began using telescopes, we have strongly refined the methods to observe the Sun and continuously increased our knowledge about it. Observations of the Sun revealed that the sunlight we perceive is variable in time and space, which is an expression of the magnetic activity of the Sun. Samuel Heinrich Schwabe was the first to investigate the periodic variations of dark spots on the solar surface (see e. g., Arlt 2011) in the 19th century. We learned that magnetic activity actually influences what we see on the Sun's surface. Studying other stars than the Sun showed that variability is not unique for the Sun. In the middle of the 20th century, Kron (1952) was one of the first who observed periodic variations in brightness out of eclipsing events of the binary system YY Geminorum consisting of two early M-dwarf stars. He concluded that heterogeneously distributed dark and bright patches are responsible for this sort of brightness variation. The term stellar activity covers a large range of phenomena occurring on the surface of stars with strong magnetic fields. Generated by convective motions below the stellar surface, magnetic field lines are responsible for e. g., starspots, plages, and flares. Observations of stellar activity phenomena by themselves do not provide sufficient information about their physical nature because the light we measure is primarily emitted from the surface of the star. For this reason, scientists came up with ideas to model the structure of stars in the second half of the 20th century. On the basis of model assumptions about the stellar interior, modelers assessed the possibility to compute synthetic spectra of the emergent light. The comparison between synthetic and observed spectra allowed astrophysicists to accurately derive stellar parameters and obtain insights into the stellar structure.

This introduction is structured in the following manner. In Sect. 1.1, I give an overview of stellar activity. Various sorts of activity phenomena originate from different atmospheric layers. Therefore, the layers of the stellar atmosphere are introduced. In the following, observations of the Sun and other main-sequence stars are presented to show that solar-like activity is a common property of stars on the cool main-sequence. The He I infrared (IR) triplet line at 10 833 Å (hereafter He I IR line for short)[1] is an effective tool to measure stellar activity and is a central theme of this thesis. I therefore highlight the term scheme of the neutral helium atom and introduce the formation of the He I IR line. Furthermore, effects of strong stellar activity on Earth-like planets around active stars are depicted. Since analyzing stellar spectra provides important insights into stellar activity, I highlight the tool of Echelle spectroscopy in Sect. 1.2, which allows us to divide and investigate the distinct light components at high resolution. I then introduce the CARMENES spectrograph (Quirrenbach et al. 2018), whose spectra of M-

[1] The wavelengths in this thesis are given for vacuum conditions, deviations from this proceeding are labeled accordingly.

dwarf stars contribute to the results of this thesis. From modeling stellar structures, scientists obtain essential conclusions on stellar activity. Some milestones and basic assumptions of stellar atmosphere models are therefore described in Sect. 1.3. The atmosphere code PHOENIX is used during the course of this work to find model atmospheres capable of reproducing chromospheric lines of stars of spectral types M2 – M3 V and to investigate the behavior of the He I IR line with increasing activity. The PHOENIX code is briefly introduced towards the end of this section. At the end of this chapter, I outline the further structure of this thesis (Sect. 1.4).

1.1 Overview of stellar activity

Activity phenomena cause temporal variations in the brightness and spectra of active stars depending on the activity state. By investigating such variations, we can interpret the occurring phenomena. The magnetic field of a star is generated by a dynamo process and determines its activity state. Parker (1955a) introduced a theory for the occurrence of a self-sustaining magnetic dynamo in the Sun – the so-called $\alpha\Omega$-dynamo. The generation of the solar-type dynamo is supposed to originate at the transition between the rigidly rotating radiative zone and the differentially rotating convective zone. The seeding field in the model of a self-sustaining $\alpha\Omega$-dynamo (Babcock 1961) is a dipole magnetic field, whose field lines are aligned meridionally. Differential rotation causes a shearing of the field lines and wraps them into a toroidal magnetic field with approximately horizontal field lines. This is the so-called Ω-effect. Within convective turbulent motions, plasma blobs rise and are stressed by Coriolis force due to stellar rotation. Therefore, the turbulent velocity field of the plasma causes a helical twist on the toroidal field lines and leads to a poloidal field – the α-effect. Such $\alpha\Omega$-dynamos are assumed to generate the magnetic fields in solar-like stars. Around the spectral types of M3/M4 stars become fully convective and a change of the acting dynamo process is suggested to take place (Houdebine et al. 2017). In M-dwarf stars of spectral types later than this boundary, turbulent convective motions are expected to solely sustain a magnetic field. However, fully convective stars also show magnetic activity features (e. g., Pizzolato et al. 2003; Hussain 2011).

Magnetic activity is observable by miscellaneous phenomena such as the following:

- Starspots are regions on a stellar surface where the convection of material is suppressed by magnetic field lines and these areas therefore appear darker than the average stellar surface (Parker 1955b). Starspots occur in the photosphere, which is the bottom layer of a stellar atmosphere.
- Plage regions are bright areas at distinct wavelengths of various emission lines arising from the overlying chromosphere. They are connected to strong magnetic fields (Leighton 1959).
- Flares are outbreaks of massive radiation at various frequencies of light and can last minutes or even hours (e. g., Benz 2017).

Such phenomena occur in different parts of the stellar atmosphere and are heterogeneously distributed over the stellar surface.

1.1.1 Structuring the stellar atmosphere

The stellar atmosphere begins where photons have a nonnegligible probability not to be absorbed by overlying material and to escape into the interstellar medium (e. g., Hubeny & Mihalas 2014). Setting up different physical assumptions for different parts of a stellar atmosphere led to a very productive procedure in obtaining knowledge about the origins of what we observe. A stellar atmosphere consists of a photosphere, chromosphere, transition region and corona.

Photosphere

Located at the bottom of the atmosphere, the photosphere is its densest layer and dominates stellar radiation in the optical range. There, the temperature is of the order of the stellar effective temperature. Assuming a star is approximated by an adiabatic cavity in thermodynamic equilibrium, its spectrum would correspond to a black-body spectrum. The distribution of spectral density of the electromagnetic spectrum of a black-body at a temperature T is given by the Planck function (Planck 1901; Planck & Masius 1914):

$$B_\nu(T) = \frac{2h\nu^3}{c^2}\frac{1}{\exp(h\nu/kT) - 1}, \tag{1.1}$$

where ν is the frequency of light, h is Planck's constant, c is the speed of light, and k designates the Boltzmann constant. Of course, a star is not a closed system in thermodynamic equilibrium. Nevertheless, a black-body is a good approximation for the effective temperature T_{eff} of a star, which is defined from its total luminosity L following the Stefan-Boltzmann law (Stefan 1879; Boltzmann 1884):

$$L = 4\pi\, R^2\, \sigma\, T_{\mathrm{eff}}^4, \tag{1.2}$$

where R is the stellar radius and σ denotes the Stefan-Boltzmann constant. Applying T_{eff} to Wien's displacement law (Wien 1893)

$$\lambda_{\mathrm{max}} = \frac{2897.8\,\mu\mathrm{m\,K}}{T_{\mathrm{eff}}} \tag{1.3}$$

yields the wavelength λ_{max} at the flux maximum, which is the color that dominates the spectrum of the star. For example, the sunlight in the visible is seen in yellow. An M dwarf is cooler than the Sun and thus emits redder light compared to the Sun (see the comparison of PHOENIX model photospheres for stars of two different effective temperatures in Fig. 1.7).

Chromosphere

Generally, the chromosphere is characterized by lower density and increasing temperatures in comparison to the underlying photosphere. However, there exist different approaches to define the chromospheric boundaries on a physical base. For instance, Linsky (1980) defines the beginning of the chromosphere where the atmosphere attains its temperature minimum. Because of decreasing density in the chromosphere, the radiative cooling declines and is no longer in balance with the nonradiative heating causing the temperature increase. On the other hand, Linsky (2017) refers the height where the optical depth becomes $\tau_{500\,\mathrm{nm}} < 0.001$, as the lower boundary of the chromosphere. For these depths, optical emission lines arise at the stellar limb. Above, temperature steadily increases with height. The upper boundary of the chromosphere is the height where hydrogen is partially ionized marking the beginning of the transition region with its steep temperature incline. In the model structure of the average quiet Sun (Fig. 1.1, Vernazza et al. 1981), the lower chromosphere exhibits a steeper temperature gradient than the upper chromosphere, which reveals a plateau-like structure instead. The underlying mechanism responsible for the heating of the upper atmosphere remains controversial to this date. A promising explanation is, however, that the heating arises from magnetohydrodynamic and acoustic shockwaves, which are generated in the convection zone and propagate to the outermost

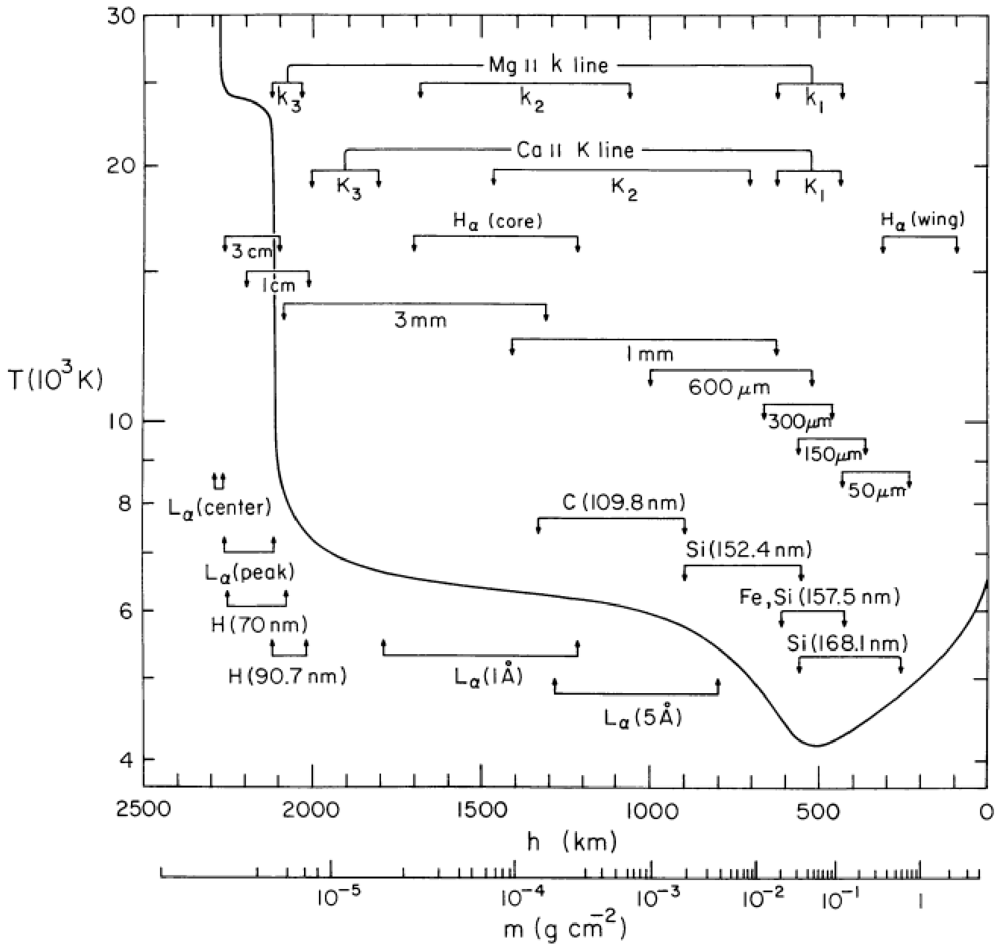

Figure 1.1: Classical temperature structure of the Sun's quiet atmosphere as a function of the column mass density and the corresponding height of the atmosphere taken from Vernazza et al. (1981). In addition, formation regions of some spectral lines are given.

atmospheric layers (e. g., Ulmschneider 1971; Ulmschneider & Kalkofen 1977; Wedemeyer et al. 2004).

The chromosphere of the Sun can be seen with naked eyes as a reddish edge above the obscured photospheric disk during a total solar eclipse. Out of a total solar eclipse, a filter (e. g., for Hα light at a wavelength of $\lambda = 6564.6$ Å) is necessary to obscure the overwhelming photospheric light. Such a filter allows only light from spectral regions dominated by chromospheric emission to pass through. Besides the Hα line, there are also several other lines that are established as chromospheric indicators. For instance, Ca II H and K line (3934.8 and 3969.6 Å) emission is considered as an outstanding evidence for the chromosphere in stars of spectral types later than mid-F (e. g., Wilson 1973; Cram & Mullan 1979).

Transition region and corona

The outermost part of the stellar atmosphere consists of the transition region and corona. From the upper chromosphere, the temperature sharply increases in the transition region from $\sim 10^4$ K to $\sim 10^6$ K (e. g., Linsky 1980). The temperature rise of the transition region becomes sharp because of the strong decline of density and the ionization of hydrogen. Consequently, the

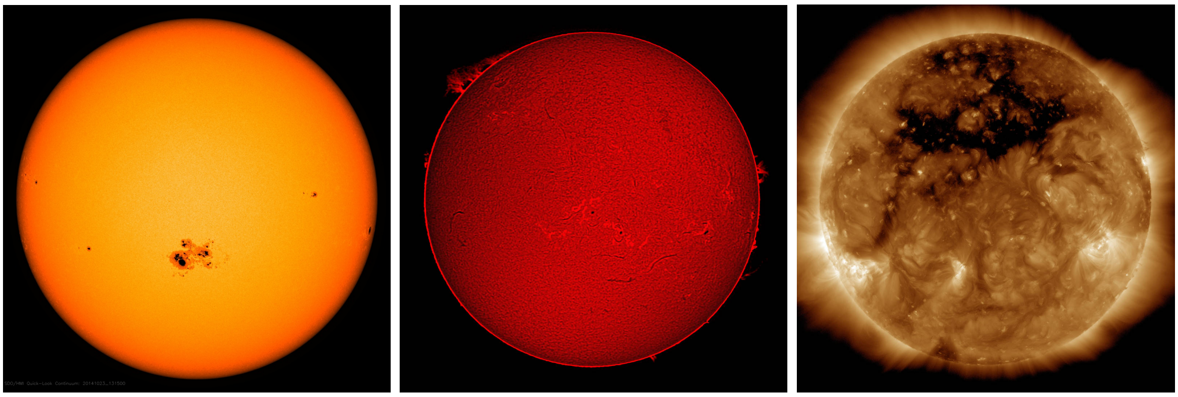

Figure 1.2: *Left panel*: A white-light image of the Sun observed by the NASA Solar Dynamics Observatory (SDO) telescope in the visible continuum on October 23rd, 2014. *Middle panel*: The Sun observed with an Hα filter on April 23rd, 2015. This image is kindly provided by Jean-Claude Merlin.[3] *Right panel*: The Sun observed at 193 Å on October 10th, 2015 by the NASA SDO telescope.

radiative cooling of hydrogen drops off (Ayres 1979). The transition region ends and the corona starts where the temperature rise flattens (e. g., Linsky 1980). Temperatures in the solar corona can reach values of 3×10^6 K. Due to the hot temperatures in the outermost atmosphere, the majority of light is emitted in the high-energy ultraviolet (UV) and X-ray wavelength range (e. g., Del Zanna & Mason 2018). Most of the gas is ionized and follows the magnetic flux tubes. Constituting the transition to outer space, stellar winds carry material away from the star to outer space (e. g., Wood 2004). During solar eclipses, the corona is visible via the hot plasma moving in loops along the magnetic field lines. Strong increases of radiation, especially from the high-energy spectral range of the extreme ultraviolet (EUV) and X-ray over relatively short timescales occur during flaring events (e. g., Foukal 2004).

1.1.2 Activity observations

Observations of the Sun

Figure 1.2 (left panel) shows a white-light (visible light) image of the Sun. A few sunspots are clearly visible, and there is a region containing several sunspots. One can even observe this activity phenomenon by eye, when solar activity state is at high level. The image also shows some bright spots near the limb, which appear hotter than the surrounding surface. These bright spots are called faculae. Sunspots and faculae originate in the solar photosphere revealing its heterogeneity. They occur in regions on the solar surface where the magnetic field lines emerge and penetrate the surface. Solar observations over decades have proven that the variability of the irradiated solar flux is connected to the appearance of sunspots (e. g., Fröhlich 2002). Furthermore, the occurrence and strength of sunspots varies according to the activity cycle of the Sun, which has been studied for centuries. By counting sunspots over decades, it was Samuel Heinrich Schwabe who detected the 11-year solar cycle (observations between 1825–1867, see e. g., Arlt 2011). With his discovery, the research of solar activity gained important publicity.

The image in the middle panel of Fig. 1.2 shows the Sun observed in Hα light. and illustrates the chromospheric inhomogeneities across the whole solar disk. Studying spectral lines such as Hα revealed the spatial and temporal evolution of the chromosphere (e. g., Kuridze et al.

[3] Image credit: `https://station504.pagesperso-orange.fr/`.

2015). Plages of Hα light indicate hot and dense regions of neutral hydrogen. On the other hand, dark areas occur where Hα light is absorbed in the line of sight. Secchi (1877) was the first who observed thread-like structures at the limb of the Sun that were later designated as spicules, which are called fibrils when they appear on the solar disc. They are plasma jets originating in the chromosphere (Beckers 1972) and can extend to ~10 000 km in atmospheric height (Lorrain & Koutchmy 1996). Hale & Ellerman (1904) discovered that chromospheric emission arises preferably in clouds above photospheric faculae by investigating Ca II H and K and Hβ (4862.7 Å) lines. Moreover, Leighton (1959) found that bright Ca II emission in plage regions is essentially connected with strong magnetic fields and mostly located in the vicinity of sunspots.

The right panel of Fig. 1.2 shows an image of the corona of the Sun. Some bright coronal loops are visible on the disk and, in particular, there is a very bright region on the left limb exhibiting many loops. Another distinctive feature of this image is a very dark region in the upper part of the solar disk. This feature is a coronal hole, where open magnetic field lines lead solar material to outer space (e. g., Cranmer 2009). The escaping particles are the stellar winds responsible for causing auroras when hitting and exciting Earth's atmosphere (e. g., Wood 2004).

Observations of other main-sequence stars

As illustrated above, we know magnetic activity from various phenomena observed on the Sun, yet it is not unique for the Sun. Extending the view to other main-sequence stars, we see that they can exhibit very similar behavior in activity indicators. For example, Ca II H and K emission occurs in all main-sequence stars of spectral types from mid-F to late-M (Linsky 2017). Following the definition of Linsky (1985), solar-like stars exhibit magnetic fields, which overcome thermal and turbulent pressure and in turn control fluid motions and heat transfer in the atmosphere. These magnetic fields are hence capable of generating activity phenomena that we observe on the surface of the Sun. On the other hand, the magnetic fields in stars of types O to A are not strong enough to generate activity like in the case of the Sun (e. g., Linsky 1985, and references therein). Typical indicators of solar-like activity in observations of other main-sequence stars are variable measurements of photometry and spectral indicators. Inhomogeneously distributed over the stellar surface, active regions cause time-dependent variability with stellar rotation. For instance, the chromospheric lines of Hα, Ca II H and K, the Ca II IR triplet (at 8500.4 Å, 8544.4 Å, and 8664.5 Å, hereafter Ca II IRT for short) and He I IR lines as well as emission from the UV and X-ray range spectroscopically indicate stellar activity. I here report some important findings of solar-like activity in main-sequence stars.

Investigating a sample of main-sequence stars in the spectral range of F to M, Wilson (1978) detected chromospheric activity variations throughout the observed sample by measuring the emission in Ca II H and K lines. Some of them also showed solar-like cycles within the observational time span of around ten years. Furthermore, the chromospheres of such cool stars exhibit some lower limit of activity that arises from the lower chromosphere – the so-called basal chromospheric flux (Schrijver 1987; Schrijver et al. 1989; Mittag et al. 2013). Thus, we see that chromospheric activity is common among main-sequence stars in the spectral range later than A.

In addition, stellar activity was also measured observing indicators, which originate from other atmospheric layers than the chromosphere. Observing solar-like stars of spectral types F to K over more than ten years, Lockwood et al. (1997) and Radick et al. (1998) found evidence for photometric variability, on both short-term and long-term timescales. Moreover, analyzing the photometric variability with respect to the mean chromospheric activity as measured in the Mount Wilson HK program (Wilson 1978), the research of Lockwood et al. (1997) and Radick et al. (1998) revealed that photometric variations are even correlated to mean chromospheric activity. Active stars are also known to exhibit hot coronae and are thus X-ray emitters (e. g., Schmitt et al. 1995; Schmitt & Liefke 2004). Emission from the high energy wavelength range was also found to correlate with chromospheric emission (e. g., Ayres et al. 1981). Such observations show that we can recognize stellar activity from different indicators and activity varies over the main-sequence.

Observing active stars other than the Sun also enabled the investigation of activity with respect to the age of a star. The analysis of chromospheric Ca II H and K emission from a sample of main-sequence stars in comparison to their age led Andrew P. Skumanich to the discovery of a law about rotational braking – the Ca II H and K emission decreases with stellar age (t) according to $\sim t^{-1/2}$ (Skumanich 1972). Transferring angular momentum into stellar winds decreases the stellar rotational velocity (Schatzman 1962; Weber & Davis 1967; Mestel 1968). Furthermore, studies such as Pizzolato et al. (2003) found that X-ray luminosity decreases with increasing rotation period. They also showed that the rotation period can even predict the X-ray luminosity within the nonsaturated X-ray regime, e. g., for stars of solar mass with rotation periods longer than 1.5 days.

Stellar activity in M dwarfs

Dwarf stars of spectral type M constitute the most common spectral type in the solar neighborhood. Within 10 pc around the Sun nearly 70 % of stars are classified as M dwarfs (Henry et al. 2006). Stars of this type are located on the coolest part of the main-sequence. They vary from $0.08\,M_\odot$ to $0.5\,M_\odot$ in stellar mass and from 2500 K – 4000 K in effective temperature (e. g., Berdyugina 2005). In particular, M dwarfs are a spectral type of stars that tends to exhibit strong stellar activity. To cite a few studies, Stauffer & Hartmann (1986), Gizis et al. (2002) and Rauscher & Marcy (2006) observed chromospheric activity in different spectral lines (e. g., in Hα, or Ca II H and K) in samples of more than 100 M dwarfs, respectively. Rauscher & Marcy (2006) also observed Ca II H and K emission to correlate with Hα measurements for high activity states. Evidence for strong stellar activity in a sample of M3 dwarfs was also measured in the chromospheric lines of Ca II K and Hα by Walkowicz & Hawley (2009). Moreover, the authors of this study found a positive correlation to coronal emission for M3 dwarfs with intermediate and high activity. In the context of magnetic activity on long-term timescales, Gomes da Silva et al. (2011) investigated 30 M0 – M5 dwarfs and found significant variability in Ca II H and K, Hα, and Na I D lines (D_1 at 5897.6 Å and D_2 at 5891.6 Å) for a fraction of the sample stars (30 % – 40 %). Besides, coronal activity in M-dwarf stars was observed in X-ray observations (e. g., Pizzolato et al. 2003; Robrade & Schmitt 2005). Robrade & Schmitt (2005) found that M dwarfs' coronae exhibit temperatures about 7×10^6 K and that strong flares are connected with higher temperatures in the corona. In spite of its relatively long rotation period of 83 days (Suárez Mascareño et al. 2016), our closest neighbor Proxima Centauri is one example for an active M-dwarf star, which shows activity-related phenomena such as chromospheric Ca II emission (e. g., Cincunegui et al. 2007; Suárez Mascareño et al. 2015; Youngblood et al. 2017) and flaring (e. g., Howard et al. 2018).

1.1.3 The He I IR line

Some current spectrographs such as CARMENES (described in Sect. 1.2) cover wavelength ranges in the near-infrared and, today, the He I IR line receives more attention in the light of measuring stellar activity. The second part of this work is on the He I IR line. Therefore, I

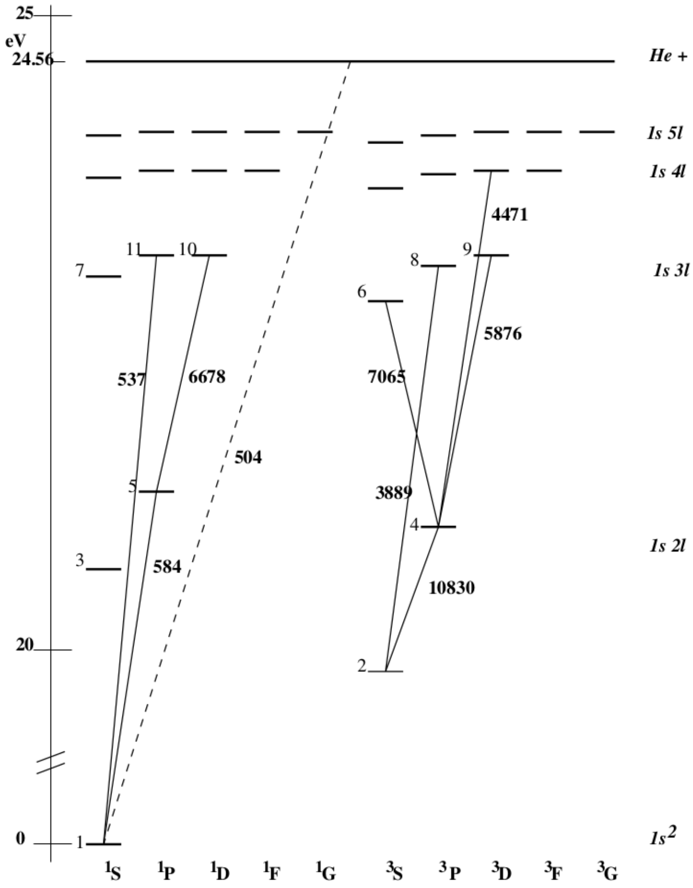

Figure 1.3: Term scheme of neutral helium. This term scheme concentrates on the first energy levels of the para- and orthohelium. The energy range between 0 and 20 eV is shortened. Transitions and wavelengths of corresponding energies of some helium lines are given by solid lines. The wavelength of the required energy to ionize neutral helium from the ground state (504 Å) is depicted by the dashed line. The shown wavelengths are given for air conditions, under which the wavelength of the He I IR line is 10 830 Å. The image is taken from Labrosse & Gouttebroze (2001) (Fig. 2 therein).

here introduce its physical background and give some important findings. The atomic model of neutral helium provides two branches, the para- and orthohelium (e. g., Labrosse & Gouttebroze 2001). For parahelium, the electron spins are in opposite directions with a total spin of $S = 0$. On the other hand, orthohelium exhibits aligned spins with a total spin of $S = 1$. The spin-orbit coupling causes the fine structure splitting and results in triplet lines in the case of the orthohelium (e. g., Foukal 2004). Figure 1.1.3 depicts a term scheme of the neutral helium atom showing wavelengths of various lines of the neutral helium atom as well as the ionization continuum at 504 Å for the ground state. The first excited energy levels of neutral helium lie $\sim$20 eV above the ground state. Temperatures higher than photospheric temperatures of cool main-sequence stars are required to raise or ionize bound electrons from the ground state. Furthermore, the photosphere is optically thick and thus does not allow photons from the hot, upper atmosphere to penetrate downwards and excite ground-state neutral helium atoms of the photosphere. Consequently, the formation of neutral helium lines has to take place in the chromosphere or above, where the temperatures increase and the material becomes optically thin (e. g., Milkey et al. 1973; Andretta & Jones 1997).

The He I IR line is a triplet line of the orthohelium at the wavelengths of 10 832.057 Å, 10 833.217 Å, and 10 833.306 Å. The lower level of the He I IR line is the metastable 2^3S level, which has to be populated in the first place to form a spectral line at 10 833 Å. Since radiative transitions from the ground state (the 1^1S singlet level) to the metastable level of the orthohelium are unlikely, the level population has to occur in a different manner. Direct excitations by collisions or photoionization and recombination (PR) followed by an electron-downward cascade are two possible population scenarios. The collisional-excitation scenario requires high densities at temperatures above 20 000 K in the transition region (Milkey et al. 1973), while the PR mechanism needs irradiation from the EUV spectral range and operates at temperatures below 10 000 K in the chromosphere (Andretta & Jones 1997). The PR mechanism in the He I IR line formation was first proposed by Goldberg (1939). In this scenario, high-energy EUV photons with wavelengths shortward of 504 Å from the transition region penetrate downwards into the chromosphere and encounter He I atoms in the ground state, which are subsequently photoionized. Then, a He II ion recombines with a free electron, which cascades down to the metastable 2^3S level, where it can absorb photospheric radiation at a wavelength of 10 833 Å and is excited to the 2^3P triplet level. Therefore, higher 2^3S level populations strengthen the He I IR line absorption. The PR mechanism is consistent with observations that showed weakening of He I IR signals in coronal holes on the Sun, where X-ray radiation declines (Zirin 1975; Sheeley & Harvey 1981). Furthermore, there are He I IR line observations of stars in the spectral range between F and K (e. g., Sanz-Forcada & Dupree 2008) and solar model studies (e. g., Andretta & Jones 1997) that suggest a contribution of both mechanisms to the formation of the line. However, there is a lack of investigations into the He I IR line in M-dwarf stars. Therefore, the second part of this thesis is dedicated to the investigation of the He I IR line behavior in chromospheric models of M dwarfs.

1.1.4 Impact of stellar activity on the habitability of exoplanets around M dwarfs

Today, more and more astrophysicists concentrate on the search of Earth-like planets around M dwarfs. Kasting et al. (1993) introduced the concept of habitable zones for main-sequence stars. The habitable zone is the volume around a star where temperatures are moderate enough to allow for the existence of liquid water on planetary surfaces. All definitions of the habitable zone are based on the requirements for life on Earth, as it is the only way of life we know. The habitable zone of the Sun is estimated to range between 0.95 and 1.37 AU. Due to the lower effective temperature and lower energy output of M dwarfs, their habitable zones are located much closer to the star. Planets within these habitable zones have much closer orbits around their host stars compared to the Earth's orbit around the Sun (Kopparapu et al. 2013). An example for such a system is Teegarden's Star. According to the Earth Similarity Index (ESI; Schulze-Makuch et al. 2011), Teegarden's Star b is currently the most similar exoplanet to the Earth with an ESI = 0.94 (Zechmeister et al. 2019). The semi-major axis of this exoplanet is about 0.02 AU with an insolation flux of $F = 1.15\,F_{\oplus}$ from its M7 V host star. Thus, Teegarden's Star b's insolation is comparable to the one of Earth, while its semi-major axis is almost two orders of magnitude smaller than the semi-major axis of the Earth in its orbit around the Sun. Therefore, the impact of stellar activity of M-dwarf stars on exoplanets in their habitable zones strongly increases.

For instance, the moderately active M dwarf TRAPPIST-1, where Gillon et al. (2016) recently detected three possible Earth-like exoplanets, emits strong X-ray radiation that could threaten possible life on these exoplanets (Wheatley et al. 2017). Peacock et al. (2019a) computed models to predict the EUV radiation of TRAPPIST-1, and they suggested that high-energy radiation could indeed lead to significant losses of water on the surfaces of these Earth-like planets. In the case of the M dwarf Proxima Centauri, a superflare with an apparent brightness of $m_V = 6.8$ mag (Howard et al. 2018) was recently detected that could be devastating to all kinds of life on its orbiting exoplanet Proxima b (Anglada-Escudé et al. 2016). The exoplanet orbits Proxima Centauri in a distance of 0.05 AU semi-major axis (Anglada-Escudé et al. 2016), which is within the habitable zone of Proxima Centauri. Segura et al. (2010) investigated the impact of a flare observed on the active M dwarf AD Leo on a possible planet in its habitable zone. Although the authors showed that the incident UV radiation during the flare should not strongly threaten life on such an exoplanet, they concluded that ionized particle beams emitted during flares carry high amounts of energy. If such a flare hits the planet, it could be dangerous for life. These examples show that the stellar activity of an M-dwarf host star can be decisive whether an orbiting exoplanet in the habitable zone is capable of hosting life or not. In this context, it is essential to understand the stellar activity of M dwarfs to improve the prediction of the habitability of life on an Earth-like exoplanet.

1.2 Spectroscopy - access to observations of chromospheres

From Earth, we can resolve the surface of the Sun very well with currently available telescopes. On the other hand, the surfaces of other stars, which are far more distant from Earth than the Sun, are not resolvable in detail. This raises the question as to which kind of observations can improve our knowledge about the activity of low-mass stars. One way is to divide the surface integrated stellar light into its color constituents – this method is called spectroscopy. This section constitutes a short outline of the history of stellar spectroscopy, and illustrates some basic operational concepts of echelle spectrographs. Finally, I describe the CARMENES spectrograph, whose observations of M dwarfs strongly contributed to my research in the course of this thesis.

1.2.1 Historical context of spectroscopy

It was Sir Isaac Newton who first introduced the fundamentals of spectroscopy with the publication of his book "*Opticks*" (Newton 1704) at the beginning of the 18th century. This book describes how the white-light of the Sun is split into its color constituents via diffraction when passing through media such as glass. Another milestone in astronomical history was the work of Joseph von Fraunhofer (Fraunhofer 1817). He developed the optical spectrograph, which was first capable of observing detailed spectra of the Sun. Using this spectrograph, he discovered dark lines in the solar spectrum and studied the spectral positions of more than 500 such dark lines at the beginning of the 19th century. A few decades later, Gustav Kirchhoff and Robert Bunsen connected the dark lines in the solar spectrum with atomic light absorption (Kirchhoff & Bunsen 1860). Furthermore, Kirchhoff developed the three laws of thermal radiation describing light emissivity and absorptivity of a gaseous body, which could explain the origin of the dark Fraunhofer lines in the spectrum of the Sun (Kirchhoff 1860). Analyzing spectra of some stars other than the Sun, Huggins & Miller (1864) recognized that other stars consist of elements also found on the Sun.

In the following decades, scientists could expand spectra to wavelengths beyond the optical range, improved the resolution of spectrographs, and the ongoing development of photography enabled the recording of spectra in a reproducible, objective manner. Johann Balmer found a formula describing four spectral lines of hydrogen occurring within the optical wavelength range of the electromagnetic spectrum (later designated as the Balmer series; Balmer 1885), which were later discovered to be a special case of the Rydberg formula (the formal description of wavelengths of the whole hydrogen line spectrum; Rydberg 1893). The early 20th century marks the beginning of quantum theory (e. g., Planck 1901; Bohr 1913; Pauli 1925; Heisenberg 1925; Schrödinger 1926; Dirac 1928), which is capable of theoretically describing the origin of atomic and molecular lines in stellar spectra. In addition, several important discoveries of stellar activity phenomena were conducted during the 20th century as described in Sect. 1.1.2.

Systematic advances of spectroscopic observation techniques strongly contributed to obtain knowledge about stellar properties and evolution throughout the 20th century. However, while the existence of planets orbiting stars other than the Sun had been postulated in 1584 by Giordano Bruno (e. g., Bettex 1965; Valentinuzzi 2019), it was only in 1995 that Michel Mayor and Didier Queloz discovered the first planet outside the solar system (Mayor & Queloz 1995), subsequently earning the Nobel Prize. They detected the exoplanet 51 Pegasi b by measuring periodic velocity shifts of spectral lines within observed spectra of its host star due to the planet's orbital motion. This exoplanet detection technique is called the radial velocity method, which nowadays has become one of the most successful methods to detect exoplanets. All these successful efforts and much more discoveries based on spectroscopy have fundamentally influenced our current perception and knowledge of the Universe.

1.2.2 Echelle spectrographs

Spectrographs use diffraction gratings to split the superimposed light of a star into its color constituents. A modern type of spectrographs is the echelle spectrograph (e. g., Schroeder 1967, 1970; Eversberg & Vollmann 2015). The big advantage of an echelle spectrograph compared to a classical one is the possibility to obtain a large wavelength coverage with comparably high resolution. The general principle of an echelle spectrograph is as follows: first, the collimated light from the telescope is diffracted by an echelle grating, and subsequently diffracted a second time perpendicular to the first diffraction. The top-left panel of Fig. 1.4 illustrates a typical structure of an echelle spectrograph.

In the top-right panel of Fig. 1.4, a sketch of an echelle grating is shown. The echelle grating consists of grooves of triangular shape in the grating plane. The tilt of the grooves corresponds to the blaze angle, which is usually large in echelle spectrographs in order to be able to resolve the higher orders. The cross disperser is necessary to separate the overlapping higher orders before entering the recording device – a CCD camera (Charged-Coupled Device). The cross disperser can be a prism, for instance. Entering the camera, the different orders are arranged next to each other as schematically depicted in the bottom panel of Fig. 1.4. This raw spectrum of an M-dwarf star shows the wavelength ranges observed in different orders of the visible and near-infrared channels of the CARMENES spectrograph.

1.2.3 The CARMENES instrument

In the course of this thesis, model spectra of M-dwarf chromospheres are compared to spectra acquired by the Calar Alto high-Resolution search for M dwarfs with Exo-earths with Near-infrared and optical Echelle Spectrographs (CARMENES; Quirrenbach et al. 2018). The CARMENES spectrograph is mounted on the 3.5 m telescope at the Calar Alto Observatory. The observatory is located in the Sierra de Los Filabres, Southern Spain. Fibers feed light from the telescope focus to two different spectrograph channels. The CARMENES instrument operates in a visible channel (VIS) in the wavelength range of 5200 – 9600 Å with a resolving power of 94 600 and in a near-infrared (NIR) channel with the spectral range between 9600 and 17 100 Å at a resolution of about 80 400. The spectrograph is designed to work with high precision, i. e., measuring radial velocity signals to an order of $1\,\mathrm{m\,s^{-1}}$, and long-term stability (Reiners et al. 2018; Ribas et al. 2018). CARMENES started its regular observations at the beginning of 2016.

The data reduction pipeline (Caballero et al. 2016b; Zechmeister et al. 2018) reduces the observed data, which are afterwards provided within the CARMENES archive. Due to its high spectral resolution and wavelength coverage in both channels, CARMENES is suitable to well

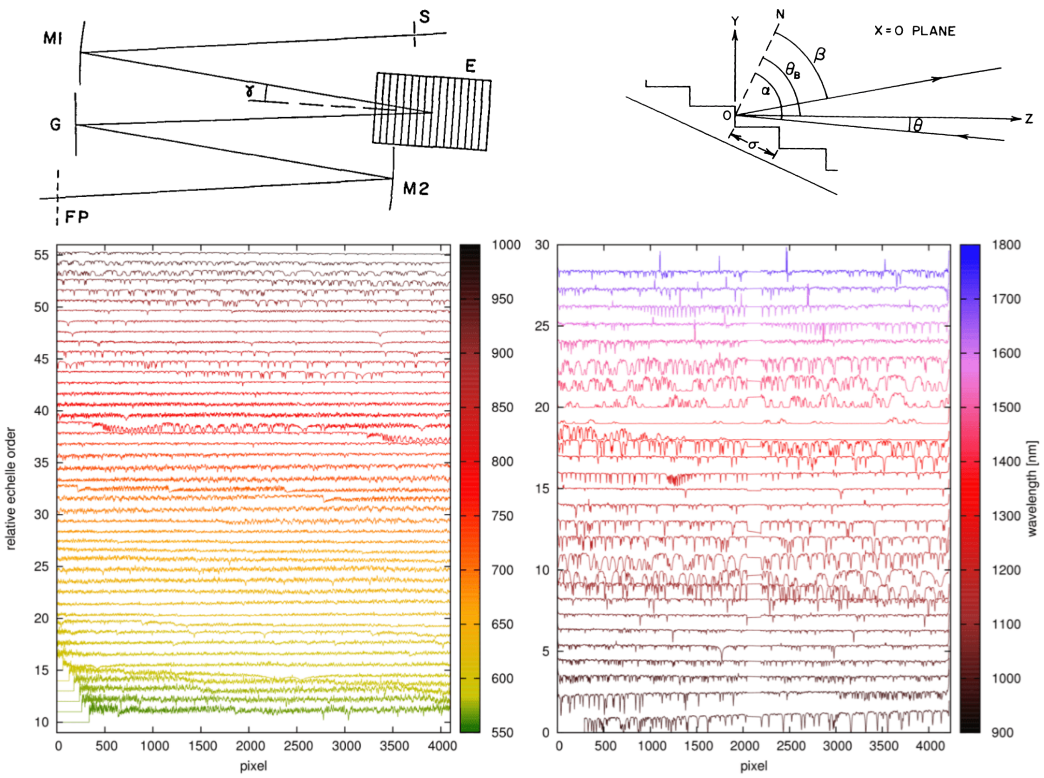

Figure 1.4: *Top-left panel*: sketch of an echelle spectrograph taken from Schroeder (1967). The incident light enters through the slit S. The light passes the collimator M1, and is diffracted by the echelle grating E, and the standard grating G. M2 is the mirror of the camera and FP is the focal plane. *Top-right panel*: sketch of echelle grating taken from Schroeder (1970). The arrows indicate the path of the light. The shown angles are as follows: Θ_B corresponds to the blaze angle, Θ is the angle between the incident light and the normal of the groove, α is the angle between the grating normal and the incident light, and β is the angle between the grating normal and the exiting light. *Bottom panel*: Exemplary spectrum of an M dwarf observed by CARMENES taken from Amado & CARMENES Consortium (2017). On the left hand side the visible spectrum, and on the right hand side the near-infrared spectrum is shown, indicating the wavelength coverage of the orders of both channels.

resolve the shape of spectral lines like Hα and the Ca II IRT lines in the VIS as well as the He I IR line in the NIR channel. Therefore, the instrument is appropriate for investigating small variations in the different spectral lines caused by the current level of activity of an observed star. Since CARMENES is attached to a ground-based telescope, telluric contamination from Earth's atmosphere is also captured in a stellar observation. For instance, molecules of oxygen (O_2), water (H_2O), and carbon dioxide (CO_2) are absorbing light from an observed star. While the optical range of CARMENES is less contaminated, the NIR channel is affected by broad contamination bands. In order to remove the telluric absorption lines, Nagel (2019) developed a method capable of erasing this contamination within the CARMENES data reduction pipeline. In Fig. 1.5, an exemplary CARMENES spectrum of the M2.5 V star GJ 671 is shown. The merged spectrum from both CARMENES channels indicates the whole spectral wavelength range of CARMENES.

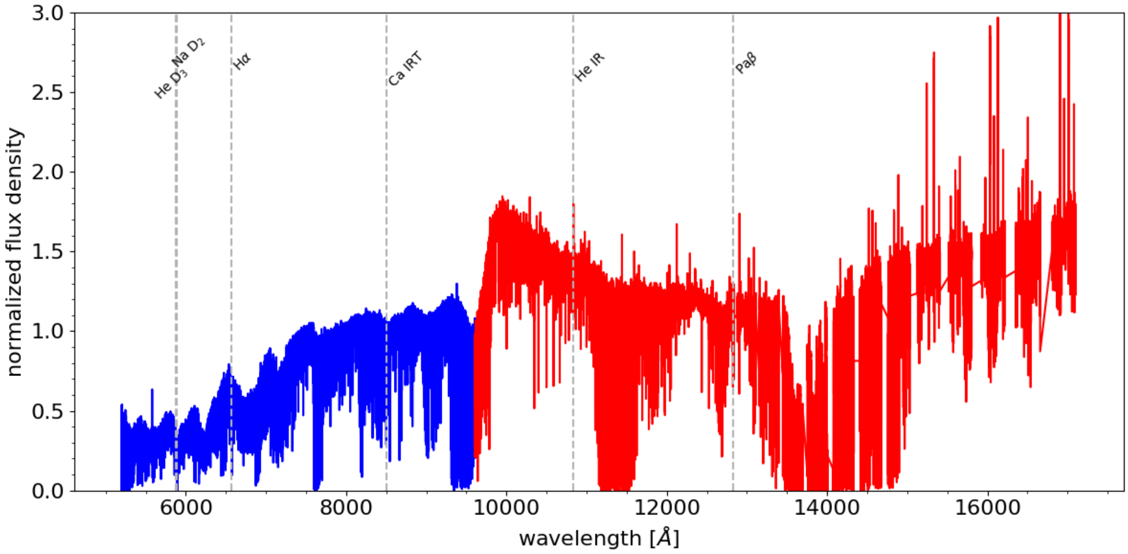

Figure 1.5: Example spectrum of GJ 671 in the whole spectral coverage of the CARMENES spectrograph. The spectrum was observed on April 11th, 2016. The spectral range of the CARMENES VIS channel is plotted as the blue solid line and the NIR range is shown in red. Additionally, the wavelengths of the chromospheric lines of He I D_3, Na I D_2, Hα, the bluest Ca II IRT line, the He I IR line, and Paβ are indicated by the dashed gray lines.

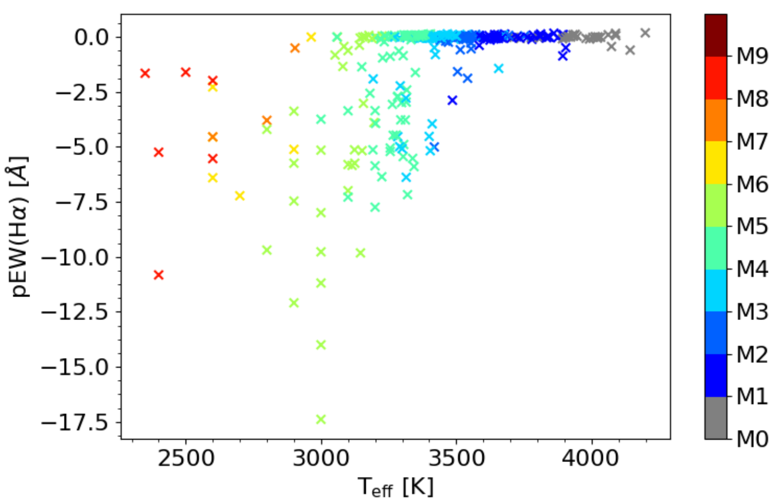

Figure 1.6: Distribution of the effective temperature against pEW(Hα) measurements of the CARMENES M dwarf survey. The color-coding corresponds to the respective spectral types. The effective temperatures were measured by Schweitzer et al. (2019). The pEW(Hα) data and the spectral types are taken from the CARMENES Cool dwarf Information and daTa Archive (Carmencita; Caballero et al. 2016a).

1.2.4 The CARMENES survey

The CARMENES spectrograph is mainly dedicated to the search of Earth-like exoplanets in the habitable zones of M dwarfs. To date, it detected several exoplanets (e. g., Ribas et al. 2018; Zechmeister et al. 2019; Nagel et al. 2019). However, the spectroscopic research that is done using CARMENES spectra also covers fields such as planetary atmospheres (e. g., Nortmann et al. 2018; Salz et al. 2018), stellar parameters (e. g., Passegger et al. 2019; Schweitzer et al. 2019), and stellar activity (e. g., Schöfer et al. 2019; Fuhrmeister et al. 2019). The survey encompasses about 340 M dwarfs in the solar neighborhood in the spectral range between M0 and M9 (Alonso-Floriano et al. 2015; Reiners et al. 2018) with an average distance of 12 pc. Figure 1.6 gives an overview of the stellar sample with regard to effective temperatures and pseudo-equivalent width (pEW) measurements of Hα. The color-coding designates the spectral types. A decrease of pEW(Hα) indicates an increase of the level of activity (Cram & Mullan 1979). This graph indicates that the stellar activity obviously tends to increase for later spectral types than M1 or, in other words, for effective temperatures lower than ~ 3700 K. Furthermore, the scattering of the pEW(Hα) values increases towards lower T_{eff}. Investigating these stars in the light of stellar activity allows astrophysicists to improve the understanding of its physical background and therefore to obtain valuable information on whether the investigated stars are capable of hosting life on exoplanets in their habitable zones.

1.3 Modeling stellar atmospheres

The performance of astronomical instruments quickly increases. However, spatially well resolved observations of stars other than the Sun are still not accessible with present instruments. Models of stellar atmospheres help to approximate the nature of real stellar structures that produce the integrated light we measure. Furthermore, models are necessary to fully understand the physical processes in stellar atmospheres. At the beginning of this section, I give a short outline of some important historical and general physical aspects of one-dimensional modeling of stellar atmospheres. Modeling atmospheres of stars is based on hydrostatic and thermodynamic equilibrium equations as well as on assumptions for the radiative transfer between different layers of the stellar atmosphere. In the following, this section deals with some of these basic assumptions. The descriptions mainly follow the explanations given by Rutten (2003), Foukal (2004), Pradhan & Nahar (2011), and Hubeny & Mihalas (2014). The use of the atmosphere code PHOENIX is essential in the course of this work. At the end of this section, I give an overview of the previous use of PHOENIX and an insight into its computational process.

1.3.1 A short introduction to one-dimensional stellar atmosphere models

A corner stone in the historical development of stellar atmosphere models is the mixing length theory (Böhm-Vitense 1958). This theory is a basic assumption for stellar one-dimensional models to roughly describe the energy transport within the stellar convection zone. The properties of moving fluid elements (temperature, density, pressure) are conserved over a distance called mixing length, meaning these elements are adiabatic within the mixing length. Beyond the mixing length, material of a fluid element is blended with its surroundings and excess energy is exchanged. The calibration of the mixing length is made with respect to solar observations. In stellar atmospheres, the gas is less dense than in the convection zone, so that radiative transport determines the energy transport within.

The first stellar atmosphere codes capable of modeling stellar spectra, such as ATLAS (Kurucz 1970) and MARCS (Gustafsson et al. 1975), were developed in the 1970s. These codes are based on several simplifications, e. g., atmospheres consisting of plane-parallel layers, which are assumed to be static, and horizontally homogeneous. Furthermore, the emitted total flux is determined by the effective temperature of the modeled star following the Stefan-Boltzmann law, and the upper atmosphere, where temperature increases, is totally neglected. Finally, they generally computed the photospheric spectrum of the considered stars in hydrostatic and radiative equilibrium according to prescribed effective temperatures, surface gravities, and chemical compositions. Radiative equilibria were generated with respect to the assumption of local thermodynamic equilibrium (LTE).[4] Although these codes strongly simplified the actual physical processes working within stellar atmospheres, they enabled the determination of approximations of temperature structures as a function of atmospheric height for different spectral types.

Vernazza et al. (1981) incorporated a few atomic species in non-local thermodynamic equilibrium (NLTE) (inter alia H, C, and Ca II) to compute plane parallel models representing different parts of the solar atmosphere including a temperature increase up to the chromosphere and transition region – the so-called VAL models. The classical, semi-empirical atmospheric structure of the average quiet Sun is called VAL C model and is depicted in Fig. 1.1, which shows the atmospheric temperature structure as a function of column mass density and atmospheric height. This static one-dimensional model includes the photosphere, chromosphere, and lower transition region. The VAL models were computed using the PANDORA code (Avrett & Loeser 1992), one of the first stellar atmosphere codes capable of taking NLTE species into account for the computation of model spectra.

Similarly to the approach of the VAL models, there were also efforts to compute model atmospheres for M-dwarf stars that include layers of the upper atmosphere. For example, Cram & Mullan (1979) investigated the activity-related evolution of Balmer line profiles. They recognized that the Balmer lines first deepen their absorption before they form peaks in the wings, and subsequently show strong emission lines, with increasing material in the electron temperature range between 5500 and 50 000 K. Taking different species into account for their chromospheric modeling (such as Ca II K, Hα, and Mg II h and k), Giampapa et al. (1982) found that the temperature gradient of the lower chromosphere behaves similar in the M dwarf-type range, which turns out to be necessary to reproduce the typical Ca II K emission in M dwarfs. The upper chromosphere turned out to be decisive for the formation of the Hα line. On the other hand, they could not simultaneously bring together Ca II K and Mg II k line profiles, particularly with increasing activity. In modeling two different states of activity of the active M3 V star AD Leo it was possible to distinguish between its quiescent (Mauas & Falchi 1994) and flaring temperature structure (Mauas & Falchi 1996). In principle, these studies scaled VAL models. Another approximation to model the upper atmosphere is the parameterization of the temperature structure such as done by Fuhrmeister et al. (2005) for a sample of mid- to late-M-dwarf stars. Using the atmosphere code PHOENIX (Hauschildt & Baron 1999), the model calculations of Fuhrmeister et al. (2005) indicated that the incorporation of C, N, O species in NLTE strongly influences the Balmer and Na I D lines for these kinds of stars.

Investigating common assumptions in such chromospheric models of M-dwarf stars, Falchi & Mauas (1998) found that the resulting spectra of low-activity dwarfs are more influenced by the tested assumptions than active dwarfs. The testing was conducted using the PANDORA code. Complete frequency redistribution (CRD) treatment for Lyα (1215.7 Å) and LTE treatment in the line blanketing of species with minor importance to the emergent spectrum were among these tested assumptions. The consequence of LTE treatment of minor important species is an underestimation of low-chromosphere electron densities affecting the emissivity of the continuum shortward of 2600 Å. Otherwise, the consequences are negligible. The term CRD means, in general, that frequencies of emitted and absorbed photons are uncorrelated. Using the CRD approximation for Lyα leads to lower ionization rates of hydrogen than in the case of partial frequency redistribution (PRD) and the electron density in the upper atmosphere is consequently underestimated. A further paper in this series (Mauas 2000) looked carefully at how changes in

[4] The concepts of a local and non-local thermodynamic equilibrium are discussed in Sect. 1.3.3.

temperature structures affect the chromospheric lines of Ca II K, Na I D, Hα, and Lyα. While the Ca II K and Na I D lines are appropriate to estimate the lower chromosphere at the temperature minimum, Hα and Lyα are good indicators for structuring the chromosphere and transition region.

Besides these classical, semi-empirical models that give an average, static picture of the atmosphere, hydrodynamical models of atmospheres are capable of simulating shocks originating in the convection zone. The resulting acoustic waves propagate through the atmosphere and, in turn, can cause strong temperature fluctuations. For instance, Carlsson & Stein (1992, 1995) took a VAL C-like chromospheric temperature structure and additionally implemented acoustic shock waves propagating upwards through the chromosphere. From their hydrodynamical time-dependent ansatz, they suggested that the semi-empirically determined temperature rise in the upper atmosphere is rather an artifact of time-averaged inhomogeneities in temperature. Their results showed that the chromospheric structure mainly indicates a decreasing temperature structure, yet the temperature fluctuations are strong. Conducting a three-dimensional, hydrodynamical simulation of the atmosphere up to the middle chromosphere with the CO^{5}BOLD code (Freytag et al. 2002, 2012), Wedemeyer et al. (2004) verified the spatial and temporal bifurcation of cold and hot gas in the solar chromosphere.

Of course, dynamical, three-dimensional models yield more realistic results and are therefore desirable for the reproduction of observed spectra. However, three-dimensional models capable of simulating the complex spatially and temporally inhomogeneous structure of the chromosphere require tremendous computational effort; the computational costs are still too large to even handle larger grids of atmosphere models (De Gennaro Aquino 2016). However, one-dimensional chromospheric models are appropriate to investigate and compare chromospheric lines in a sample of stars. In this thesis, I investigate a sample of 50 stars. In order to reproduce observed chromospheric lines I calculate static, one-dimensional, semi-empirical models of chromospheres including several lines in NLTE (see Chapter 2). In total, I computed a set of more than 150 chromospheric models, the calculation of each one of which took at least time in the order of tens of CPU hours.

1.3.2 Hydrostatic equilibrium

A star is usually assumed to be a gaseous sphere. Self-gravity holds the stellar matter together and outward-directed pressure gradients prevent the collapse of the star. Furthermore, the force compensation within the sphere of a star is assumed to be static, i. e., the sphere is considered to be intrinsically constant. The static balance between self-gravity and pressure gradients yields the hydrostatic equilibrium. Therefore, the hydrostatic equation

$$\frac{\mathrm{d}P}{\mathrm{d}r} = -\frac{G\,M(r)\,\rho(r)}{r^2} \tag{1.4}$$

of a layer of thickness dr describes the balance between the pressure gradient $\mathrm{d}P/\mathrm{d}r$ of the gas of density ρ and the gravitational acceleration $g(r) = \frac{G\,M(r)}{r^2}$ as a function of radius r, where G is the gravitational constant and M is the spherical stellar mass. Solving the hydrostatic equation yields the pressure stratification in a model atmosphere. Real stellar atmospheres exhibit different branched stratifications. However, the resulting pressure stratification represents an average approximation to reality.

1.3.3 Radiative transfer

If a star were to be approximated as an adiabatic cavity in thermodynamic equilibrium, it would only emit thermal radiation according to a black-body spectrum. In thermodynamic equilibrium, the gas and radiation within a closed system are in balance and do not exchange energy with the exterior. The system achieves its equilibrium through randomly occurring particle collisions. Of course, the measured stellar spectrum deviates from this approximation since a star is not a closed system. The atmosphere becomes optically thinner with increasing height allowing for the escape of radiation. Emanating photons pervade the overlying atmospheric layers and the escaping radiation is influenced by material within the outer atmosphere. Radiative transport thus plays a decisive role for the emerging spectrum.

Propagating through the atmosphere, the photons encounter electrons, atoms, ions and molecules in the stellar atmosphere that influence the light an observer receives from a star. The particles occurring in the atmosphere absorb, emit and scatter radiation in the line of sight. Such processes lead to obvious deviations from the spectrum of a pure Planck radiator. Therefore, density, temperature, and the species of particles occurring in the atmosphere affect the propagating radiation.

Radiative transfer equation

In the following, I briefly introduce the formal radiative transfer and some important state variables within. Considering the energy budget $\mathrm{d}E_\nu$ of the frequency interval $\mathrm{d}\nu$ that is radiatively transported through a surface element of area $\mathrm{d}A$ in a solid angle $\mathrm{d}\Omega$ at location $\mathbf{r}$ in the time interval $\mathrm{d}t$, the specific intensity I_ν is defined as the corresponding proportionality coefficient in

$$\mathrm{d}E_\nu = I_\nu(\mathbf{r}, \mathbf{n}, t)\,\cos\theta\,\mathrm{d}A\,\mathrm{d}\Omega\,\mathrm{d}t\,\mathrm{d}\nu, \tag{1.5}$$

where $\mathbf{n}$ is the propagation direction and θ indicates the polar angle between $\mathbf{n}$ and the normal to the surface element. The mean intensity J_ν over all solid angles is then given by

$$J_\nu(\mathbf{r}, t) = \frac{1}{4\pi}\oint I_\nu\,\mathrm{d}\Omega. \tag{1.6}$$

While radiation propagates through the atmosphere, the intensity of the radiation varies according to the radiative transport equation:

$$\frac{\mathrm{d}I_\nu}{\mathrm{d}z} = \eta_\nu - \kappa_\nu\,I_\nu, \tag{1.7}$$

where $\mathrm{d}z$ is the atmospheric height interval, κ_ν designates the monochromatic linear extinction coefficient, and η_ν gives the monochromatic emissivity coefficient.[5] In terms of radiative propagation, the optical depth is essential to measure variation in the specific intensity. The optical depth τ_ν of a frequency ν in $\mathrm{d}z$ is defined by

$$\mathrm{d}\tau_\nu = -\kappa_\nu\,\mathrm{d}z. \tag{1.8}$$

The ratio between the monochromatic emissivity and extinction

$$S_\nu = \frac{\eta_\nu}{\kappa_\nu} \tag{1.9}$$

gives the source function S_ν. Applying the definitions of Eqs. (1.8) and (1.9) to (1.7), one can derive the radiative transfer equation as

$$\frac{\mathrm{d}I_\nu}{\mathrm{d}\tau_\nu} = I_\nu - S_\nu. \tag{1.10}$$

[5] The coefficients of absorption, emission, and scattering are discussed below.

Thus, the specific intensity can be determined from the absorption (κ_ν) and emission (η_ν) coefficients.

From integrating the intensity I_ν over all solid angles, one obtains the radiative flux at a distinct wavelength from

$$\mathbf{F}_\nu(\mathbf{r}, \mathbf{n}, t) = \oint I_\nu \, \mathbf{n} \, \mathrm{d}\Omega. \tag{1.11}$$

Regarding one-dimensional atmospheres of plane-parallel shape or in spherically symmetry, we have only one flux component to be nonzero, which is the height or radial component, respectively. The total radiative flux is then $\mathbf{F}_\nu$ integrated over all frequencies. In radiative equilibrium, it holds that

$$\nabla \cdot \mathbf{F} = 0. \tag{1.12}$$

Coefficients of absorption, emission, and scattering

As mentioned above, the treatment of absorption, emission, and scattering contains different sorts of atomic transitions. Here, I briefly introduce the corresponding coefficients affecting e. g., the source function (1.9), and the radiative transfer equation (1.10).

Absorption or emission of light at discrete spectral wavelengths occurs when a photon is absorbed or emitted by a transition of a bound electron, which is excited to a higher or de-excited to a lower energy level. Therefore, the constituents of bound-bound transitions are photons and bound electrons. The photons from such transitions carry discrete energy amounts

$$E_u - E_l = h \, \nu_{lu} = hc/\lambda_{lu}, \tag{1.13}$$

where E_l and E_u are the energies of levels l and u, and λ_{lu} ($\nu_{lu} = c/\lambda_{lu}$) designates the wavelength (frequency) of light from a transition from the lower level l to the upper level u. The bound-bound transitions affect the formation of spectral lines in stellar spectra. For this sort of transitions, one can express the monochromatic emissivity coefficient as

$$\eta_{\nu,bb} = \frac{h \, \nu_{lu}}{4\pi} \, n_u \, A_{ul} \, \psi(\nu), \tag{1.14}$$

and the monochromatic absorption coefficient as

$$\kappa_{\nu,bb} = \frac{h \, \nu_{lu}}{4\pi} (n_l \, B_{lu} - n_u \, B_{ul}) \, \phi(\nu), \tag{1.15}$$

where A_{ul} is the Einstein coefficient of spontaneous emission between levels u and l, B_{lu} is the corresponding Einstein coefficient of absorption, and B_{ul} that of induced emission, while n_l and n_u are the population densities of the respective levels. Induced emission requires another photon, which stimulates the excited atom to de-excite and emit a photon of respective energy. The line profile functions $\phi(\nu)$ and $\psi(\nu)$ taking into account line broadening are equal in the assumption of CRD. The Einstein relations for bound-bound transitions state that

$$\begin{aligned} A_{ul} &= \frac{2h\nu^3}{c^2} B_{ul} \\ B_{lu} &= \frac{g_u}{g_l} B_{ul}, \end{aligned} \tag{1.16}$$

where g_l and g_u are the statistical weights of the respective levels. Investigating the formation of spectral lines, source functions of bound-bound transitions are decisive in the radiative transfer equation. From the emission and absorption coefficient equations (1.14) & (1.15), and using the Einstein relations (1.16), the source function (1.9) simplifies to

$$S_\nu^{\text{line}} = \frac{\eta_{\nu,bb}}{\kappa_{\nu,bb}} = \frac{2h\nu^3}{c^2}\left(\frac{n_l g_u}{n_u g_l} - 1\right)^{-1} \tag{1.17}$$

in the case of bound-bound transitions. Within (1.17), the population number densities require further assumptions of LTE or NLTE, which are explained below.

Bound-free and free-free transitions also cause absorption or emission of photons, but they affect the shape of the spectral continuum. Bound-free transitions describe transitions either of bound electrons that are ionized (photoionization) or processes where free electrons are captured (recombination). For instance, a photon with a sufficient amount of energy ionizes a bound electron and, additionally, transfers kinetic energy to it. The absorption coefficient of a bound-free transition[6] is defined as

$$\kappa_{\nu,bf} = n_l\, \sigma_{bf}(\nu)\, (1 - \exp(-h\nu/kT))\,, \tag{1.18}$$

where n_l is the population density of level l, and σ_{bf} represents the photoionization cross section. The emission coefficient for a radiative recombination[6] is given by

$$\eta_{\nu,fb} = n_l\, \sigma_{bf}(\nu)\, (1 - \exp(-h\nu/kT))\, B_\nu(T), \tag{1.19}$$

where $B_\nu(T)$ denotes the Planck function (1.1) and k designates the Boltzmann constant. Free-free transitions are caused by collisional interactions of free charged particles, that is, the interaction between free electrons and ions. When free electrons lose kinetic energy in such a process, they emit photons. This type of radiation is called Bremsstrahlung. The corresponding emission coefficient is defined by

$$\eta_{\nu,ff} = n_{\text{ion}}\, n_e\, \sigma_{ff}(\nu, T)\, (1 - \exp(-h\nu/kT))\, B_\nu(T), \tag{1.20}$$

where n_{ion} is the ion density, n_e denotes the electron density, and σ_{ff} is the free-free transition cross section. On the other hand, the equation

$$\kappa_{\nu,ff} = n_{\text{ion}}\, n_e\, \sigma_{ff}(\nu, T)\, (1 - \exp(-h\nu/kT))\,, \tag{1.21}$$

describes the absorption coefficient of a free-free transition.

Another source of perturbation that concerns propagating radiation is photon scattering. In such scattering events, photons are redirected and possibly change their wavelength. Scattering also contributes to the formation of the spectral continuum. The elastic scattering of photons with free electrons is called Thomson scattering, and its absorption coefficient is defined by

$$\kappa_T = \sigma_T n_e, \tag{1.22}$$

where σ_T denotes the Thomson cross section. The Thomson emission coefficient is given by

$$\eta_T = \sigma_T n_e J_\nu. \tag{1.23}$$

Rayleigh scattering happens when photons are elastically scattered with electrons bound within atoms and molecules, whose diameter is small compared to the wavelength of the scattered

[6] Here, I show the approximation for the case of LTE.

photon. This sort of scattering depends on the occurring species. Therefore, the absorption coefficient follows the equation

$$\kappa_R = \sum_i n_i \sigma_{R,i}, \tag{1.24}$$

where $\sigma_{R,i}$ designates the Rayleigh scattering cross section, and n_i is the number density of species i. The emission coefficient corresponds to

$$\eta_R = \kappa_R J_\nu. \tag{1.25}$$

Taking the transition and scattering processes into account, one obtains the total absorption coefficient as

$$\kappa_\nu^{\text{tot}} = \kappa_{\nu,bb} + \kappa_{\nu,bf} + \kappa_{\nu,ff} + \kappa_T + \kappa_R, \tag{1.26}$$

and total emission coefficient as

$$\eta_\nu^{\text{tot}} = \eta_{\nu,bb} + \eta_{\nu,fb} + \eta_{\nu,ff} + \eta_T + \eta_R. \tag{1.27}$$

Local thermodynamic equilibrium

As mentioned above, a stellar atmosphere is not a closed system in thermodynamic equilibrium with a constant temperature. On the contrary, radiation escapes into open space and the atmosphere itself exhibits large temperature gradients. However, at least the lower atmosphere, that is, the photosphere, can be assumed to be in LTE, which means that collisions dominate locally. Therefore, temperatures and densities are determined by LTE within the photospheric layers. This approximation is justified for the photosphere due to its dense, opaque gas and comparatively small gradients in density and temperature. Generally, the Boltzmann excitation equation and the Saha ionization equation yield the level occupation densities, while the Maxwell velocity distribution describes the motion of the particles in LTE.

From the Boltzmann excitation equation the population density n for level l to level u at a given ionization stage s in LTE can be computed by

$$\frac{n_{s,l}}{n_{s,u}} = \frac{g_{s,l}}{g_{s,u}} \exp\left(-\frac{E_{s,l} - E_{s,u}}{kT}\right), \tag{1.28}$$

where the energy difference $E_{s,u} - E_{s,l}$ corresponds to the excitation energy necessary for raising an electron from level l to level u, and $g_{s,l}/g_{s,u}$ denotes the ratio of the respective statistical weights. Considering the radiation, the application of the Boltzmann equation to the line source function (1.17) yields

$$S_\nu^{\text{line}} = \frac{2h\nu^3}{c^2} \frac{1}{\exp\left(\frac{h\nu_{lu}}{kT}\right) - 1} = B_\nu, \tag{1.29}$$

simplifying to the Planck function in the LTE approximation. With introducing the partition function

$$U_s(T) = \sum_i g_{s,i} \exp\left(-\frac{E_{s,i}}{kT}\right), \tag{1.30}$$

summing up all bound levels i of a particle, one obtains the relation of the number density $n_{s,l}$ to the total number density n_s:

$$\frac{n_{s,l}}{n_s} = \frac{g_{s,l}}{U_s(T)} \exp\left(-\frac{E_{s,l}}{kT}\right). \tag{1.31}$$

The Saha equation gives the population density of a particle of ionization stage $s+1$ to s:

$$\frac{n_{s+1}}{n_s} = \frac{1}{n_e}\frac{2U_{s+1}}{U_s}\left(\frac{2\pi m_e kT}{h^2}\right)^{3/2} \exp\left(-\frac{\chi_s}{kT}\right), \tag{1.32}$$

where m_e denotes the electron mass, and χ_s is the energy necessary to ionize the particle of stage s.

Non-local thermodynamic equilibrium

The chromosphere contributes to a stellar spectrum in a way that deviates from LTE in the photosphere. Since it is hotter, less dense and optically thinner than the photosphere, photons cannot thermalize any more and the LTE assumption cannot be sustained above the photosphere. Therefore, the assumption of the NLTE has to be introduced. The notion NLTE comprises of all sorts of departures from LTE. While the assumption of the Maxwell velocity distribution still holds in NLTE, the occupation numbers of the energy levels of particles differ from the LTE assumption as given by the Saha and Boltzmann equations. Transitions between different excitation levels are caused by collisions or radiation. Due to the validity of the Maxwell velocity distribution of the particles, the collisions tend to approach the LTE state, yet the radiation induces the departure from LTE occupation numbers. Particularly with decreasing optical depth, the radiative processes prevail over collisions increasing the deviation from LTE.

Approaching the NLTE case in the calculation of level populations, the complexity of the radiative transfer increases. The population densities are allowed to depart from the LTE as described by the departure coefficients b_i:

$$b_i = \frac{n_i}{n_i^*}, \tag{1.33}$$

where n_i^* denotes the LTE population density of level i and n_i is the actual NLTE number density. This relation states the extent of departure from LTE densities. Applying NLTE population densities and departure coefficients to the line source function in (1.17) yields

$$S_\nu^{\text{line}} = \frac{2h\nu^3}{c^2}\frac{1}{\frac{b_l}{b_u}\exp\left(\frac{h\nu_{lu}}{kT}\right) - 1} \approx \frac{b_u}{b_l}B_\nu \tag{1.34}$$

in the Wien approximation for small wavelengths $\left(\exp\left(\frac{h\nu_{lu}}{kT}\right) \gg 1\right)$.

To calculate the NLTE level populations, which are taken into account in the determination of the absorption and emission coefficients, and thus in the source function, the collisional and radiative Einstein coefficients have to be considered. The total transition rate (P_{lu}) of levels l and u ($l < u$) has to be split into collisional (C_{lu}) and radiative rates (R_{lu}) by

$$P_{lu} = C_{lu} + R_{lu}. \tag{1.35}$$

There are five different sorts of collisional and radiative, excitation and de-excitation mechanisms to consider: collisionally, there are electron-induced excitation and de-excitation, while the radiative transitions separate into radiative excitation, and spontaneous, as well as induced radiative de-excitation. The excitation rate of collisions is

$$C_{lu} = n_e q_{lu} = n_e \int_{v_0}^{\infty} \sigma_{lu}(v)\, v\, f(v)\, \mathrm{d}v, \tag{1.36}$$

where q_{lu} denotes the excitation rate coefficient as a function of collisional electron cross section σ_{lu}, velocity v and velocity distribution $f(v)$ of the particles, while v_0 corresponds to the threshold velocity of the collisional excitation ($E_{lu} = \frac{1}{2}mv_0^2$). Here, the electron density is taken into account, since the majority of collisions are due to free electrons. On the basis of the Maxwell velocity distribution,

$$C_{ul} = \frac{n_l^*}{n_u^*} C_{lu} \tag{1.37}$$

gives the rate of collisional de-excitation. The equation

$$R_{lu} = B_{lu} \int_0^\infty \phi_{lu}(\nu)\, J_\nu \,\mathrm{d}\nu, \tag{1.38}$$

where B_{lu} is the Einstein coefficient of radiative excitation, and ϕ_{lu} is the absorption profile, yields the radiative excitation rate. Furthermore, the radiative de-excitation is defined by

$$R_{ul} = A_{ul} + B_{ul} \int_0^\infty \psi_{ul}(\nu)\, J_\nu \,\mathrm{d}\nu, \tag{1.39}$$

where A_{ul} is the Einstein coefficient of spontaneous de-excitation, B_{ul} the Einstein coefficient of induced de-excitation, and ψ_{ul} denotes the emission line profile. With the assumption of CRD, the emission and absorption profiles ψ_{ul} and ϕ_{lu} are equal. The population densities are time-independent and the excitation and de-excitation rates are assumed to be in balance. Therefore, the population densities are determined by the statistical equilibrium as given by the rate equations

$$\frac{\mathrm{d}n_l}{\mathrm{d}t} = \sum_{u \neq l} n_u P_{ul} - n_l \sum_{u \neq l} P_{lu} = 0. \tag{1.40}$$

1.3.4 The atmosphere code PHOENIX

The atmosphere code PHOENIX[7] (Hauschildt 1992, 1993; Hauschildt & Baron 1999) was developed to compute model atmospheres of objects such as stars, planets, and novae. In a model computation, PHOENIX computes the model atmosphere as well as the corresponding model spectrum. It calculates the atmospheric line blanketing for all these kinds of objects incorporating millions of atomic and molecular lines. The one-dimensional PHOENIX mode is able to solve the radiative transfer for lines of miscellaneous atomic species in the LTE and NLTE approximation for the geometry of spherical symmetry or plane-parallel atmospheres. A model atmosphere is characterized by a parameterization of physical properties such as stellar mass and effective temperature. A self-consistent radiation field is calculated for a set of fundamental physical variables (temperatures, gas pressures, and population densities) at each wavelength and within every atmospheric layer.

Computational process of a PHOENIX model

PHOENIX calculates model atmospheres and corresponding spectra of stars on the basis of a given temperature stratification. Within the work of this thesis, I use a one-dimensional temperature stratification in spherical symmetry. In the first step of a model calculation, the hydrostatic equations are solved in order to obtain the physical state variables like density and pressure for the whole model atmosphere. The intensity of radiation within different layers is calculated from the radiative transfer equations, and solving the rate equations yields the

[7] `https://www.physik.uni-hamburg.de/en/hs/group-hauschildt/research/phoenix.html`

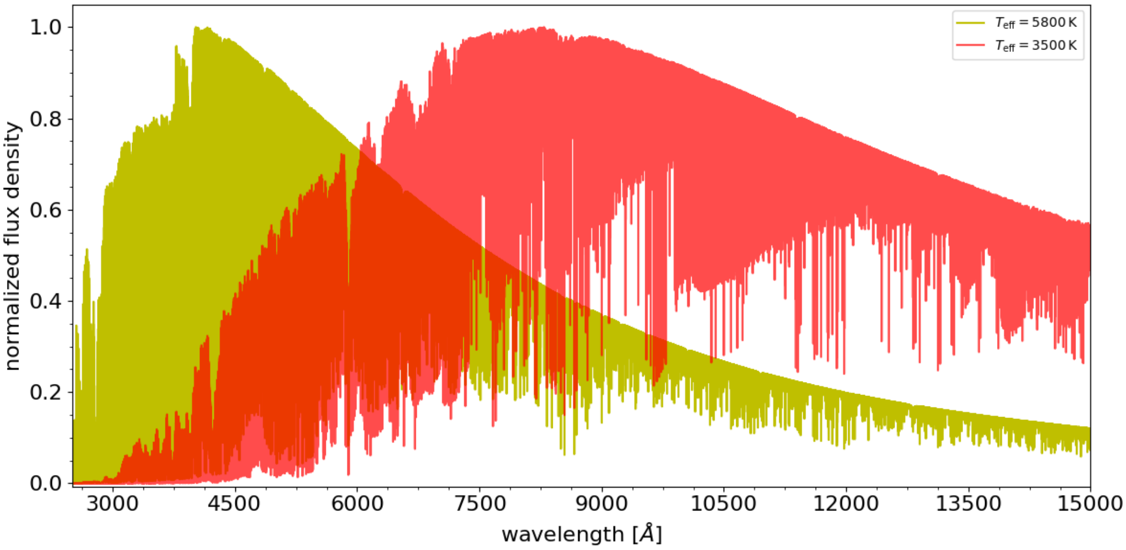

Figure 1.7: PHOENIX model spectra of the photospheres of an M dwarf with an effective temperature $T_{\mathrm{eff}} = 3500\,\mathrm{K}$, surface gravity $\log g = 5.0\,\mathrm{dex}$, and solar metallicity [Fe/H] = 0.0 (red), and the Sun ($T_{\mathrm{eff}} = 5800\,\mathrm{K}$, $\log g = 4.5\,\mathrm{dex}$, and [Fe/H] = 0.0, yellow) taken from (Husser et al. 2013). The fluxes of the spectra are normalized to their respective flux maxima.

occupation numbers of the energy levels of incorporated atoms, ions, and molecules. Thereupon, the complete model atmosphere of one iteration is determined. The code then iteratively solves hydrostatic equations as well as radiative transfer and rate equations for every wavelength taken into account (Fuhrmeister 2005). All models computed in the course of this work are based on CRD. In order to approximate realistic stellar observations in the spectral range of the chromospheric lines investigated in this thesis, I continuously use several atomic species in NLTE. For further details regarding this aspect and other hidden parameters, I refer to Chapter 2.

Applications of PHOENIX to models of stars

PHOENIX has been used to compute whole grids of stellar atmospheres: for instance, the first extensive grid of models using PHOENIX (in the one-dimensional plane parallel mode and with the assumption of LTE) was computed by Allard & Hauschildt (1995) comprising of more than 700 models in the effective temperature range $1500\,\mathrm{K} \leq T_{\mathrm{eff}} \leq 4000\,\mathrm{K}$, which are in good agreement with blue and near-infrared observations of M dwarfs. Another extensive library of model atmospheres was constructed by Hauschildt et al. (1999). The models, again computed in LTE for one-dimensional plane parallel atmospheres, range from 3000 K to 10 000 K in effective temperature. Husser et al. (2013) created the most recent library of PHOENIX LTE photospheres in spherical symmetry for a temperature grid between 2300 K and 12 000 K, various surface gravities, and metallicities. In Fig. 1.7, two PHOENIX photosphere spectra from Husser et al. (2013) are shown. The model photosphere of an early M dwarf with an effective temperature of $T_{\mathrm{eff}} = 3500\,\mathrm{K}$ is compared to that of the Sun ($T_{\mathrm{eff}} \approx 5800\,\mathrm{K}$). This library was used, for instance by Passegger et al. (2018), to derive stellar parameters in the parameter space of effective temperatures, surface gravities, and metallicities for a sample of around 300 M dwarfs observed by CARMENES.

Chromospheres with PHOENIX

The PHOENIX code has also been utilized to compute chromospheric models. For example, Short & Doyle (1997) and Fuhrmeister et al. (2005) extended PHOENIX model photospheres by attaching arbitrarily linear temperature rises representing chromosphere and transition region to simulate spectral lines arising in the chromosphere. Recently, a similar approach by Peacock et al. (2019a,b) was used to calculate the EUV radiation of low-mass stars in order to draw conclusions on the habitability of exoplanets orbiting them. From their model set, they suggested that the temperature structures of the upper atmospheres of early M dwarfs may be similar.

As mentioned above, there are generally two ways of simulating chromosphere models of M dwarfs: it is possible to (i) scale down solar-type VAL C models (e. g., Mauas & Falchi 1994; Fontenla et al. 2016) or (ii) attach linear temperature rises on top of a given photospheric model (e. g., Short & Doyle 1997; Fuhrmeister et al. 2005), that is, a parameterization of the chromosphere. I follow the latter ansatz during the course of this work. A parameterization of an atmospheric structure is an effective tool in one-dimensional atmosphere models to reproduce observed spectra. Although it simplifies the unknown heating mechanism in the upper atmosphere with arbitrarily chosen temperature rises, this method is capable of approximating spectral lines arising in the chromosphere. By solely using the atmosphere code PHOENIX, Fuhrmeister et al. (2005) applied this approach to model spectra of five observed mid- to late-type M dwarfs. The starting point of the model construction is an underlying photosphere model in radiative equilibrium such as the one depicted in Fig. 1.7 (red model spectrum). Next, the chosen ansatz specifies how the temperatures within chromosphere and transition region increase as linear functions of the logarithm of column mass density. In principle, the created models exhibit a moderately increasing temperature gradient in the chromosphere, followed by a very steep one in the transition region. For some models the lower chromospheric temperature rise was slightly adjusted to improve the fit within the Na I D lines. Fuhrmeister et al. (2005) also tried to vary the upper chromosphere by adding a second linear section in the chromosphere with a plateau-like shape. This attempt led to an overpredicted flux in the Balmer lines and thus failed in improving the overall fit.

I here follow this approach with one modification: instead of a single linear temperature rise in the chromosphere, it is distinguished into linear temperature rises of the logarithm of column mass density in the lower and upper chromosphere for all models. Using a newer version of PHOENIX (version 17), this approach leads to better overall fits than taking into account only one linear temperature rise in the chromosphere. Therefore, the upper atmosphere is divided into three sections with different temperature gradients: lower chromosphere, upper chromosphere, and lower transition region. The aim is to refine the structure to simultaneously fit observed chromospheric lines of different species forming in separate parts of the chromosphere. More details on the construction of the chromospheric models and the free parameters are given in Chapter 2. An example of a chromospheric model for an M-type star with an effective temperature of 3500 K is depicted in Fig. 1.8.

1.4 Further structure of the thesis

Modeling stellar chromospheres is an important tool for improving our understanding of the physical processes taking place in the upper atmosphere. In Chapter 2, I present a set of chromosphere models created with the PHOENIX code to simultaneously fit the chromospheric lines of Na I D_2, Hα, and the bluest Ca II IRT line in a sample of 50 M2 – M3 V stars observed by the CARMENES spectrograph covering the wavelength ranges of these chromospheric lines.

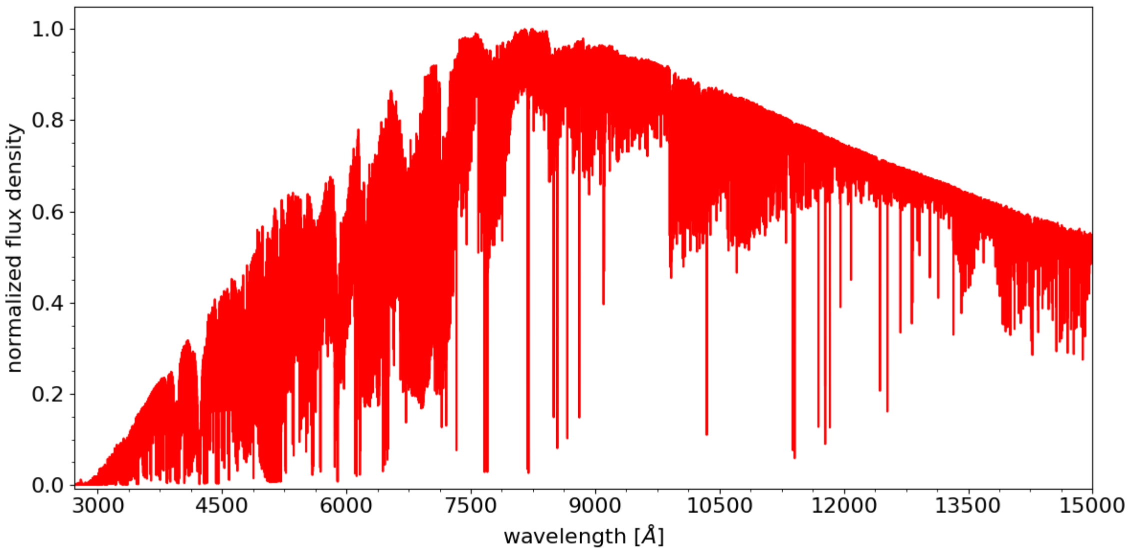

Figure 1.8: Examplary PHOENIX spectrum of an M-dwarf chromosphere model with an effective temperature of 3500 K. This model was calculated for the publication Hintz et al. (2019, model #042 therein), which is a part of this thesis. The fluxes of the spectrum are normalized to the maximum flux.

Prescribed, parameterized temperature structures are used to calculate self-consistent model atmospheres and synthetic spectra. The free parameters are adjusted to approach the shape and strength of the absorption and emission lines. A statistical analysis is performed to identify the best-fit models. The active stars of the sample reveal more difficulties to find appropriate model fits since the respective lines tend to go into emission. Therefore, linear combinations of one inactive and one active component are applied to fit the lines of this type of stars. From the application of linear combinations, we also obtain surface filling factors of inactive and active components. Thus, it allows the possibility to investigate variations of the filling factors with respect to the current activity state of the variable stars in the sample.

Chapter 3 is devoted to the investigation of the He I IR line at 10 833 Å. Recently, this line has received more attention in the research of transmission spectroscopy of exoplanets transiting M dwarfs. A crucial analysis of the stellar He I IR line is substantial to solely extract the planetary contribution to the line. The behavior of the He I IR line is analyzed in the same sample of stars discussed in Chapter 2. Covering different states of activity in the sample enables the analysis of activity-depending behavior of the line. Specifically, the He I IR line strength is investigated as a function of the irradiated EUV radiation from the transition region, which is self-consistently computed in the model chromospheres. This investigation also allows conclusions on the formation mechanisms of the He I IR line, namely the PR and collisional excitation mechanisms. Furthermore, since the model set was optimized for chromospheric lines in the visible range, the prediction of the He I IR line is statistically analyzed.

Chapter 4 summarizes the results of the investigations of the chromospheric modeling of M-dwarf stars. Finally, I give an outlook on further possible investigations with respect to chromospheres of M dwarfs in the light of modeling and observations.

Chapter 2

Chromospheric modeling of M 2–3 V stars with PHOENIX

In this chapter, I present a method of fitting chromospheric lines using parameterized chromosphere models with the reproduced publication "*Chromospheric modeling of M 2–3 V stars with PHOENIX*" (Hintz et al. 2019). The PHOENIX model calculations within were performed by myself as the main author with the help and advice by Birgit Fuhrmeister. The data analysis and writing were done by myself, however, important ideas and advice were provided by Birgit Fuhrmeister, Stefan Czesla, and my supervisor Jürgen H. M. M. Schmitt. The other co-authors contributed by data acquisition and proofreading. The paper Hintz et al. (2019) has been published in Astronomy & Astrophysics.

A&A 623, A136 (2019)
https://doi.org/10.1051/0004-6361/201834788

Astronomy & Astrophysics

The CARMENES search for exoplanets around M dwarfs

Chromospheric modeling of M 2–3 V stars with PHOENIX

D. Hintz[1], B. Fuhrmeister[1], S. Czesla[1], J. H. M. M. Schmitt[1], E. N. Johnson[2], A. Schweitzer[1], J. A. Caballero[3], M. Zechmeister[2], S. V. Jeffers[2], A. Reiners[2], I. Ribas[4,5], P. J. Amado[6], A. Quirrenbach[7], G. Anglada-Escudé[6,8], F. F. Bauer[2], V. J. S. Béjar[9,10], M. Cortés-Contreras[3], S. Dreizler[2], D. Galadí-Enríquez[11], E. W. Guenther[12,9], P. H. Hauschildt[1], A. Kaminski[7], M. Kürster[13], M. Lafarga[4,5], M. López del Fresno[3], D. Montes[14], J. C. Morales[4,5], V. M. Passegger[1], and W. Seifert[7]

1 Hamburger Sternwarte, University of Hamburg, Gojenbergsweg 112, 21029 Hamburg, Germany
e-mail: dominik.hintz@hs.uni-hamburg.de
2 Institut für Astrophysik, Friedrich-Hund-Platz 1, 37077 Göttingen, Germany
3 Centro de Astrobiología (CSIC-INTA), ESAC, Camino Bajo del Castillo s/n, 28692 Villanueva de la Cañada, Madrid, Spain
4 Institut de Ciències de l'Espai (ICE, CSIC), Campus UAB, c/ de Can Magrans s/n, 08193 Bellaterra, Barcelona, Spain
5 Institut d'Estudis Espacials de Catalunya (IEEC), 08034 Barcelona, Spain
6 Instituto de Astrofísica de Andalucía (CSIC), Glorieta de la Astronomía s/n, 18008 Granada, Spain
7 Landessternwarte, Zentrum für Astronomie der Universität Heidelberg, Königstuhl 12, 69117 Heidelberg, Germany
8 School of Physics and Astronomy, Queen Mary, University of London, 327 Mile End Road, London, E1 4NS, UK
9 Instituto de Astrofísica de Canarias, c/ Vía Láctea s/n, 38205 La Laguna, Tenerife, Spain
10 Departamento de Astrofísica, Universidad de La Laguna, 38206 Tenerife, Spain
11 Centro Astronómico Hispano-Alemán (MPG-CSIC), Observatorio Astronómico de Calar Alto, Sierra de los Filabres, 04550 Gérgal, Almería, Spain
12 Thüringer Landessternwarte Tautenburg, Sternwarte 5, 07778 Tautenburg, Germany
13 Max-Planck-Institut für Astronomie, Königstuhl 17, 69117 Heidelberg, Germany
14 Departamento de Física de la Tierra y Astrofísica and UPARCOS-UCM (Unidad de Física de Partículas y del Cosmos de la UCM), Facultad de Ciencias Físicas, Universidad Complutense de Madrid, 28040 Madrid, Spain

Received 6 December 2018 / Accepted 31 January 2019

ABSTRACT

Chromospheric modeling of observed differences in stellar activity lines is imperative to fully understand the upper atmospheres of late-type stars. We present one-dimensional parametrized chromosphere models computed with the atmosphere code PHOENIX using an underlying photosphere of 3500 K. The aim of this work is to model chromospheric lines of a sample of 50 M2–3 dwarfs observed in the framework of the CARMENES, the Calar Alto high-Resolution search for M dwarfs with Exo-earths with Near-infrared and optical Echelle Spectrographs, exoplanet survey. The spectral comparison between observed data and models is performed in the chromospheric lines of Na I D_2, Hα, and the bluest Ca II infrared triplet line to obtain best-fit models for each star in the sample. We find that for inactive stars a single model with a VAL C-like temperature structure is sufficient to describe simultaneously all three lines adequately. Active stars are rather modeled by a combination of an inactive and an active model, also giving the filling factors of inactive and active regions. Moreover, the fitting of linear combinations on variable stars yields relationships between filling factors and activity states, indicating that more active phases are coupled to a larger portion of active regions on the surface of the star.

Key words. stars: activity – stars: chromospheres – stars: late-type

1. Introduction

Magnetic stellar activity comprises a zoo of phenomena affecting different layers of stellar atmospheres. Magnetic activity is thought to be fundamental for the heating of the hot chromospheres and even hotter coronae of late-type stars, which produce all of their high-energy ultraviolet and X-ray fluxes observed from these stars. In addition, late-type stars are frequently planet hosts, and hence their activity is also recognized to have a crucial influence on the evolution of their planets, their atmospheric structure, and also possible life on their surfaces (e.g. Segura et al. 2010; France et al. 2016; O'Malley-James & Kaltenegger 2017).

In late-type stars, the chromosphere is the atmospheric layer between the photosphere and transition region. In the classical, one-dimensional picture, the atmospheric temperature reaches a minimum at the base of the chromosphere and then starts increasing outward. Several heating processes, such as acoustic heating (Wedemeyer et al. 2004), back warming from the corona lying above the chromosphere and the transition region, and magnetic heating, are likely operating in the chromosphere. The importance and magnitude of the individual proposed heating processes still remains unsettled even in the case of the Sun.

The chromosphere is the origin of a plethora of emission lines used to study its structure and physical conditions. Solar images show the chromosphere to be highly inhomogeneous and constantly evolving (e.g. Kuridze et al. 2015). In the stellar context, there is the concept of the so-called basal chromospheric emission, since all stars show some small extent of chromospheric activity which is referred to as basal chromospheric activity (Schrijver 1987; Schrijver et al. 1989; Mittag et al. 2013).

It is clear that a proper representation of such a chromosphere requires a dynamical three-dimensional approach. For example, Uitenbroek & Criscuoli (2011) give a thorough discussion about the limitations of one-dimensional modeling even of stellar photospheres. These authors concluded that the neglect of convective motions, nonlinearities of temperatures, and densities in computing the molecular equilibrium and level populations as well as the nonlinearities of the Planck function depending on the temperature may cause inaccurate interpretations of the calculated spectra. On the other hand, currently existing computer codes combining magnetohydrodynamic models with realistic radiative transfer for the chromosphere (and also for the photosphere) still remain computationally too costly to handle larger grids and cannot sensibly be juxtaposed to observations (De Gennaro Aquino 2016). Therefore, irrespective of its shortcomings, we consider the inferred chromospheric parameters from one-dimensional modeling useful, in particular, in a comparison among a sample of stars.

Fundamental insights into the chromospheric structure can, however, already be obtained based on static one-dimensional models with a parametrized temperature stratification. In the case of stars we are presumably looking simultaneously at the integrated emission of many, spatially unresolved "mini-chromospheres", which may be described by a mean one-dimensional model; at least, such models can reproduce observed stellar spectra well for M dwarfs (Fuhrmeister et al. 2005). On the other hand, the VAL C model by Vernazza et al. (1981) is often considered the classical model for the temperature structure in the photosphere, the chromosphere, and the transition region of the average quiet Sun. Up to now there are two approaches to model the chromospheres in late-type stars, viz., scaling the VAL C model (Mauas & Falchi 1994; Fontenla et al. 2016) or parameterizing the chromosphere (Short & Doyle 1997). Analyzing chromosphere models for a large stellar sample of homogeneous effective temperatures gives the opportunity to detect whether and how the chromospheres are distinguished.

In this study we use the state-of-the-art atmosphere code PHOENIX[1] (Hauschildt 1992, 1993; Hauschildt & Baron 1999) to compute chromospheric model atmospheres based on a parametrized temperature stratification and obtain the resulting spectra. These spectra are then compared to observed high-resolution spectra obtained with the CARMENES (Calar Alto high-Resolution search for M dwarfs with Exo-earths with Near-infrared and optical Echelle Spectrographs) spectrograph. Section 2 describes these observations and Sect. 3 highlights the model construction. We compare the computed model spectra to a stellar sample of M2.0, M2.5, and M3.0 dwarfs observed by CARMENES and search for the best-fit models to each star of the stellar sample in Sect. 4. Moreover, we also fit linear model combinations to the spectra to improve the modeling of the active stars where single models do not yield adequate fits. By calculating model combinations we obtain filling factors illustrating the coverage of inactive and active regions on the surfaces of the stars. In Sect. 5 we present our results and conclusions.

[1] https://www.hs.uni-hamburg.de/index.php?option=com_content&view=article&id=14&Itemid=294&lang=de

2. Observations

2.1. CARMENES

The CARMENES spectrograph (Calar Alto high-Resolution search for M dwarfs with Exo-earths with Near-infrared and optical Echelle Spectrographs; Quirrenbach et al. 2018) is a highly stabilized spectrograph attached to the 3.5 m telescope at the Calar Alto Observatory. The visual channel (VIS) operates in the wavelength range from 5200 to 9600 Å, and the infrared channel (NIR) covers the range between 9600 and 17 100 Å. The spectral resolution of the VIS channel is about $R = 94\,600$ and that of the NIR channel is $R = 80\,400$.

Since the start of the observations at the beginning of 2016, CARMENES regularly observes a sample of ~300 dM0 to dM9 stars in the context of its CARMENES survey (Alonso-Floriano et al. 2015; Reiners et al. 2018). The main goal of the survey is to find Earth-like planets in the habitable zone of M dwarfs by measuring periodic signals in the radial velocities of the stars with a precision on the order of 1 m s^{-1} and long-term stability (Reiners et al. 2018; Ribas et al. 2018). The CARMENES survey sample is only magnitude limited in each spectral type. Notably, no activity selection was applied.

The CARMENES spectra cover a wide range of chromospheric activity indicators except for the classical Ca II H and K lines. However, the Ca II infrared triplet (IRT) lines can be observed, which were recently shown to be a good substitute of the blue Ca II H and K lines (Martínez-Arnáiz et al. 2011; Martin et al. 2017). Additional chromospherically active lines covered by the CARMENES spectrograph are Hα, the Na I D lines, and the He I D_3 line. The shape of the different lines is well resolved, including possible self-reversal in Hα (in case of emission lines) or the emission cores of Na I D. Traditionally, M dwarfs have been designated with spectral class identifiers dM, dM(e), and dMe depending on whether Hα is in absorption, not detectable, or in emission in low-resolution spectra. We mainly use the indices of the Ca II IRT lines as activity indicators, since they simply fill in and go into emission without showing a complicated line profile like Hα. Nevertheless, we refer to the traditional designations in Table 1 and examples of each class can be found in Fig. 4.

2.2. Stellar sample

This study focuses on simulations and observations of the chromospheric properties of dM-type stars with an effective temperature of about 3500 K, a surface gravity of $\log g = 5.0$, and solar metallicity [Fe/H] = 0.0 dex. These stars lie between the earliest M and the mid-M dwarfs. While the stellar parameters can be fixed in the modeling, we have to allow some margin in the selection of targets from the CARMENES sample. For this study, we selected all targets with stellar parameters fulfilling $T_{\rm eff} = 3500 \pm 50$ K, $\log g = 5.0 \pm 0.2$ dex, and [Fe/H] $= 0.0 \pm 0.3$ dex as measured by Passegger et al. (2018) using PHOENIX photospheric models and also given in the CARMENES input catalog Carmencita (Caballero et al. 2016a). Carmencita gathers information about the stars observed by CARMENES from different sources, including the effective temperature, gravity, and metallicity. We choose this range of effective temperature because it comprises a large number of M dwarfs, some of which show Hα in emission. Below this effective temperature range the number of observed dM-type stars quickly decreases. The stellar sample investigated in this work comprises 50 M dwarfs with spectral types between dM1.5 and dM3.5. According to

Table 1. Basic information about the considered stars.

Karmn	Name	Sp. type	Ref. (SpT)	T_{eff} (K)	$\log g$ (dex)	[Fe/H] (dex)	$I_{\mathrm{H}\alpha}$ (Å)	$I_{\mathrm{Ca\,IRT}}$ (Å)	Available spectra	Used spectra
J00389+306	Wolf 1056	dM2.5	AF15	3537	4.89	–0.04	1.74	0.63	12	7
J01013+613	GJ 47	dM2.0	PMSU	3537	4.92	–0.13	1.75	0.63	8	1
J01025+716	BD+70 68	dM3.0	PMSU	3478	4.92	0.00	1.73	0.62	107	35
J01433+043	GJ 70	dM2.0	PMSU	3534	4.91	–0.08	1.71	0.63	5	4
J02015+637	G 244-047	dM3.0	PMSU	3495	4.93	–0.05	1.73	0.62	17	11
J02442+255	VX Ari	dM3.0	PMSU	3459	4.96	–0.07	1.72	0.62	34	19
J03531+625	Ross 567	dM3.0	Lep13	3484	4.94	–0.04	1.73	0.63	28	28
J06103+821	GJ 226	dM2.0	PMSU	3543	4.89	–0.05	1.76	0.63	19	5
J07044+682	GJ 258	dM3.0	PMSU	3469	4.94	–0.01	1.74	0.62	7	7
J07287-032	GJ 1097	dM3.0	PMSU	3458	4.95	–0.02	1.72	0.62	8	8
J07353+548	GJ 3452	dM2.0	PMSU	3526	4.93	–0.14	1.74	0.63	5	2
J09133+688	G 234-057	dM2.5(e)	Lep13	3545	4.93	–0.16	1.52	0.57	6	2
J09360-216	GJ 357	dM2.5	PMSU	3488	4.96	–0.14	1.73	0.63	2	1
J09425+700	GJ 360	dM2.0(e)	PMSU	3511	4.91	–0.03	1.47	0.58	16	12
J10167-119	GJ 386	dM3.0	PMSU	3511	4.89	0.01	1.75	0.63	6	3
J10350-094	LP 670-017	dM3.0	Sch05	3457	4.95	–0.03	1.74	0.62	5	1
J10396-069	GJ 399	dM2.5	PMSU	3524	4.91	–0.06	1.75	0.62	2	2
J11000+228	Ross 104	dM2.5	PMSU	3500	4.94	–0.10	1.74	0.63	47	39
J11201-104	LP 733-099	dM2.0e	Ria06	3540	4.97	–0.27	0.88	0.46	3	3
J11421+267	Ross 905	dM2.5	AF15	3512	4.90	–0.02	1.75	0.63	113	69
J11467-140	GJ 443	dM3.0	PMSU	3523	4.87	0.06	1.76	0.62	5	2
J12230+640	Ross 690	dM3.0	PMSU	3528	4.87	0.03	1.77	0.63	80	34
J12248-182	Ross 695	dM2.0	PMSU	3476	4.98	–0.18	1.73	0.63	2	2
J14152+450	Ross 992	dM3.0	PMSU	3456	4.94	0.00	1.74	0.62	8	6
J14251+518	θ Boo B	dM2.5	AF15	3512	4.92	–0.08	1.75	0.63	8	5
J15095+031	Ross 1047	dM3.0	PMSU	3480	4.93	–0.01	1.72	0.62	7	7
J15474-108	LP 743-031	dM2.0	PMSU	3515	4.96	–0.21	1.75	0.61	8	6
J16092+093	G 137-084	dM3.0	Lep13	3455	4.98	–0.09	1.67	0.62	5	5
J16167+672N	EW Dra	dM3.0	PMSU	3504	4.91	0.00	1.75	0.62	35	23
J16254+543	GJ 625	dM1.5	AF15	3516	4.98	–0.27	1.75	0.63	32	28
J16327+126	GJ 1203	dM3.0	PMSU	3486	4.92	0.00	1.74	0.63	7	5
J16462+164	LP 446-006	dM2.5	PMSU	3505	4.92	–0.05	1.76	0.63	7	6
J17071+215	Ross 863	dM3.0	PMSU	3482	4.94	–0.05	1.73	0.62	7	7
J17166+080	GJ 2128	dM2.0	PMSU	3544	4.91	–0.10	1.75	0.63	8	6
J17198+417	GJ 671	dM2.5	PMSU	3499	4.93	–0.08	1.73	0.63	8	8
J17578+465	G 204-039	dM2.5	AF15	3459	4.94	0.00	1.67	0.61	9	8
J18174+483	TYC 3529-1437-1	dM2.0e	Ria06	3515	4.96	–0.18	0.99	0.51	32	32
J18419+318	Ross 145	dM3.0	PMSU	3473	4.95	–0.06	1.71	0.62	7	7
J18480-145	G 155-042	dM2.5	PMSU	3500	4.94	–0.09	1.75	0.63	13	5
J19070+208	Ross 730	dM2.0	AF15	3532	4.95	–0.21	1.69	0.63	10	8
J19072+208	HD 349726	dM2.0	PMSU	3535	4.94	–0.20	1.69	0.63	12	9
J20305+654	GJ 793	dM2.5	PMSU	3475	4.96	–0.08	1.64	0.62	25	11
J20567-104	Wolf 896	dM2.5	PMSU	3523	4.89	0.00	1.76	0.62	6	6
J21019-063	Wolf 906	dM2.5	AF15	3521	4.90	–0.05	1.76	0.62	9	5
J21164+025	LSPM J2116+0234	dM3.0	Lep13	3475	4.95	–0.05	1.75	0.62	21	9
J21348+515	Wolf 926	dM3.0	PMSU	3484	4.92	0.00	1.73	0.63	27	20
J22096-046	BD-05 5715	dM3.5	PMSU	3492	4.96	–0.01	1.76	0.62	41	26
J22125+085	Wolf 1014	dM3.0	PMSU	3500	4.92	–0.04	1.72	0.62	32	29
J23381-162	G 273-093	dM2.0	PMSU	3545	4.92	–0.13	1.78	0.63	8	5
J23585+076	Wolf 1051	dM3.0	PMSU	3470	4.94	0.00	1.73	0.62	16	10

Notes. Karmn is the Carmencita identifier. All effective temperatures (±51 K), gravities (±0.07 dex), and metallicities (±0.16 dex) are measured by Passegger et al. (2018). The indices $I_{\mathrm{H}\alpha}$ and $I_{\mathrm{Ca\,IRT}}$ are measured in this work.

References. AF15: Alonso-Floriano et al. (2015); Lep13: Lépine et al. (2013); PMSU: Reid et al. (1995); Ria06: Riaz et al. (2006); Sch05: Scholz et al. (2005).

Pecaut & Mamajek (2013)[2], dM2 and dM3 stars typically have effective temperatures at 3550 and 3400 K. Table 1 gathers basic data about our stellar sample including Carmencita identifiers, names, spectral types, effective temperatures, surface gravities, and metallicities.

[2] The effective temperatures for the spectral subtypes are given in http://www.pas.rochester.edu/~emamajek/EEM_dwarf_UBVIJHK_colors_Teff.txt

2.3. Data reduction

The spectra for our sample stars provided in the CARMENES archive are reduced by the CARMENES data reduction pipeline (Caballero et al. 2016b; Zechmeister et al. 2018); note that all wavelengths refer to vacuum. Typical exposure times of the spectra were 800, 900, 1200, and 1800 s, but there are also several spectra with integration times lower than 500 s. Since we want to compare line shapes to the model predictions we require a minimum of 300 s of integration time in order to exclude very noisy spectra.

To investigate the spectra, we corrected them for the barycentric velocity shift and also systematic radial velocity shifts of the individual stars. We did not apply a telluric correction since the chromospheric lines used in our study are usually only weakly affected (Hα and He I D$_3$). However, spectra containing airglow signals in the cores of the Na I D lines are neglected in the modeling. Therefore, we inspected by eye the spectra exhibiting possible airglow contamination in the Na I D line cores (in the wavelength range of $\lambda_{\rm NaD} \pm 0.4$ Å) and excluded those affected; we only used spectra observed up until 21 December 2017. The number of available and used spectra of our sample stars are listed in Table 1; most of the excluded spectra contain airglow signals.

2.4. Activity characterization of the sample stars

The stars in the sample feature very different levels of stellar activity as can be easily seen qualitatively in the Hα line, which is an absorption line for most of our sample stars, but goes into emission for four stars. The state of activity can be characterized quantitatively by the line index of chromospheric emission lines. Following the method of Fuhrmeister et al. (2018) and Robertson et al. (2016), the line index $I_{\rm line}$ is defined by

$$I_{\rm line} = w\left(1 - \frac{\overline{F_{\rm line}}}{\overline{F_{\rm ref1}} + \overline{F_{\rm ref2}}}\right), \quad (1)$$

where w is the bandwidth of the spectral line, and $\overline{F_{\rm line}}$, $\overline{F_{\rm ref1}}$, and $\overline{F_{\rm ref2}}$ indicate the mean flux densities of the spectral line and reference bands. The line index corresponds to the pseudo-equivalent width.

In this paper, we investigated the Na I D, Hα, and Ca II IRT lines. These lines represent the most widely used chromospheric indicators in our wavelength range. Another known chromospheric line covered by our wavelength range is the He I D$_3$ line, which is seen in none of the spectra of our more inactive stars. Of the Na I D doublet and the Ca II IRT triplet lines, we only considered the bluest components because the remaining lines are influenced in the same manner by the chromospheric structure. For the Ca II IRT line we chose $w = 0.5$ Å to be the width of the line band centered at the (vacuum) wavelength of the line at 8500.35 Å. The reference band located at the blue side of the Ca line is centered at 8481.33 Å with a half-width of 5 Å, and the central wavelength of the red band is 8553.35 Å with a half-width of 1 Å to avoid telluric contamination for most radial and barycentric velocities. The center of the Hα line band is located at a wavelength of 6564.62 Å and we chose the width of the line band to be 1.6 Å. The reference bands are located at 6552.68 ± 5.25 and 6582.13 ± 4.25 Å. For the Na I D$_2$ line at 5891.58 ± 0.2 Å the reference bands are 5872.3 ± 2.3 and 5912.0 ± 2.0 Å.

Figure 1 shows an overview of the activity levels and the spread in effective temperature of the stellar sample. Most of the stars are considered inactive indicated by the high Ca II IRT index above 0.6 Å, which should represent the average activity level of the star. The more active stars in our sample are GJ 360 and G 234-057 exhibiting line indices between 0.6 and 0.55 Å (further on also called semi-active), and even more active are LP 733-099 and TYC 3529-1437-1 with indices below 0.55 Å. There is a photospheric trend to higher indices for higher effective temperatures marked as the linear fit in Fig. 1. This trend can also be found for the photospheric models by Husser et al. (2013) varying the effective temperatures between 3400 and 3600 K ($\log g$ = 5.0 dex, [Fe/H] = 0.0 dex and [α/Fe] = 0.0 dex). We used the index of the Ca II IRT line to specify the different activity levels of the investigated stars, although in many studies, such as in Fuhrmeister et al. (2018), the line index of Hα is used to determine the activity state. While the Hα line is a strong line very sensitive to activity changes, the drawback in using the Hα line is its evolution with increasing stellar activity: this line first goes into absorption, then fills up the line core and eventually goes into emission (see, e. g. Cram & Mullan 1979). Thus more active stars can exhibit the same Hα line index as less active stars. The Ca II IRT line only fills in and goes into emission while the activity level increases, making its index easier to interpret in terms of the activity state.

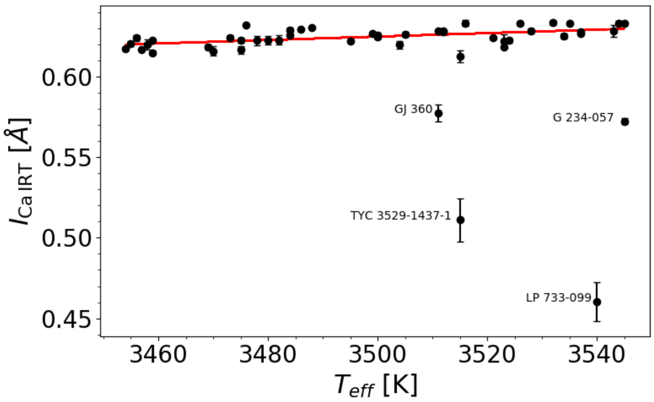

Fig. 1. Average $I_{\rm line}$ in the Ca II IRT line at 8500.35 Å against the $T_{\rm eff}$ of the investigated stars. The error bars correspond to the standard deviations of the line indices of individual spectra of the respective stars. The red line is a linear fit for the inactive stars exceeding $I_{\rm Ca\,IRT}$ = 0.6 Å. The four active stars are highlighted by their names.

In Fig. 2 we compare the average line indices of the Ca II IRT line and the Hα line that are given in Table 1. The plot exhibits a good correlation between the two indices with a Pearson correlation coefficient of 0.97, while the indices of the more inactive stars form an uncorrelated cloud. At the highest Ca II IRT line indices there are two stars, Ross 730 and HD 349726, exhibiting lower Hα indices; we interpret these to be the most inactive stars of the sample being located in the branch where increasing activity means increasing Hα line depth. As error bars we plot the standard deviation of the line indices derived from individual spectra of the respective stars. The scatter in the Hα line index is obviously larger than that in the Ca II IRT line. So the Hα line appears to be more sensitive for activity variations in the whole observation period. This supports the choice for the Ca II IRT line index as a robust estimate of the mean activity level of a given star. For further insight into the variability of individual stars we show the time series of the three considered lines for TYC 3529-1437-1 in Fig. 3 as one of the stars with the largest amount of variations. Figure 3 demonstrates the typical temporal sampling of the spectral time series, which has been optimized for planet searches. The average sampling cadence is around 14 days. Also times of different levels of activity can be

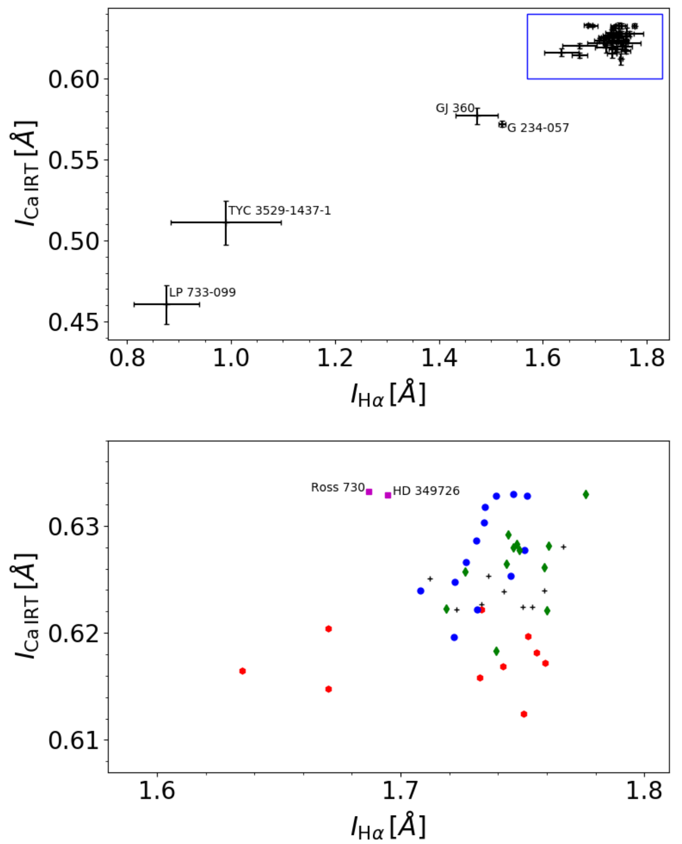

Fig. 2. *Upper panel*: average I_{line} in the Ca II IRT line at 8500.35 Å against the average I_{line} in the Hα line of the investigated stars. The error bars correspond to the standard deviations of the line indices of individual spectra of the respective stars. *Lower panel*: zoom of the range of the inactive stars without error bars (blue box in the upper panel). The black pluses indicate the stars best fit by model #079, red hexagons indicate best fit by model #080, blue circles by #042, green diamonds by #047, and magenta squares by #029 (see Sect. 4.2). The model numbers and properties are given in Table C.1. To improve clarity, the errors are faded out in the lower panel.

identified: the star was more active at the end of the time series. Since we do not want to average the variations of the lines or whole periods of enhanced activity, we do not co-add the observations. Co-adding would certainly boost the signal-to-noise ratio (S/N), but most stars also have S/Ns above 50 in single spectra, which is sufficient for our analysis. Therefore, we examine the spectrum with the median line index $I_{\mathrm{Ca\,IRT}}$ as a representation of the median activity level of the star. For the inactive stars the level of variation is much lower and an averaging would be possible in the sense of not mixing different activity states, but for consistency we treat these like the four active stars.

In Fig. 4 we show individual example spectra of one inactive (GJ 671) and two active stars (GJ 360, TYC 3529-1437-1). The inactive star exhibits absorption lines in Na I D$_2$, Hα, and the bluest Ca II IRT line. For GJ 360 the spectral lines are in the transition from absorption to emission, while the lines in the spectrum of TYC 3529-1437-1 are clearly in emission. Thus we cover the bandwidth of rather inactive, semi-active, and very active M dwarfs in our sample.

3. Model construction

The state-of-the-art PHOENIX code models atmospheres and spectra of a wide variety of objects such as novae, supernovae,

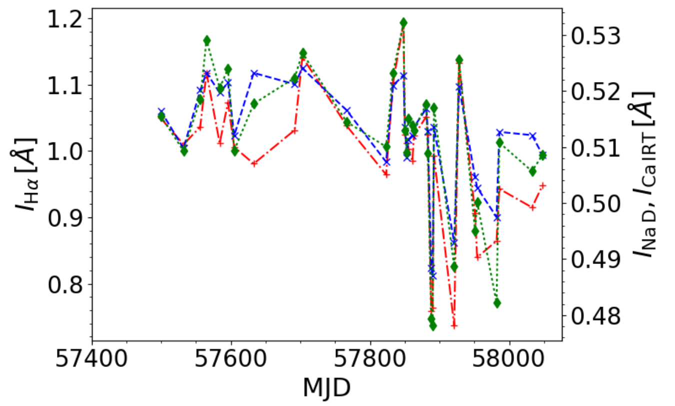

Fig. 3. Time series of the indices I_{line} of the Na I D$_2$ (blue crosses), Hα (red pluses), and Ca II IRT line (green diamonds) of TYC 3529-1437-1.

planets, and stars (Hauschildt 1992, 1993; Hauschildt & Baron 1999). A number of PHOENIX model libraries covering M dwarfs have been published. For instance, Allard & Hauschildt (1995) used local thermodynamic equilibrium (LTE) calculations for dwarfs with effective temperatures of 1500 K ≤ T_{eff} ≤ 4000 K and Hauschildt et al. (1999) computed an even wider model grid in the temperature range between 3000 and 10 000 K. A recent library of PHOENIX model atmospheres was presented by Husser et al. (2013).

3.1. Selection of a photospheric model

All of the above-mentioned libraries are exclusively concerned with the photospheres. The first model calculations that investigated the chromospheres using PHOENIX were carried out by Short & Doyle (1997) and Fuhrmeister et al. (2005). These models extend the atmospheric range up to the transition region, but are still rooted in the atmospheric structure of the photosphere, which therefore, provides the basis for our calculations.

In this paper, we adopt a photospheric model from the Husser et al. (2013) library as the underlying photosphere. This model was calculated under the assumptions of spherical symmetry and LTE using 64 atmospheric layers. The particular model atmosphere we adopted was computed for the parameters T_{eff} = 3500 K, log g = 5.0 dex, [Fe/H] = 0.0 dex, and [α/Fe] = 0.0 dex; in Fig. 5 (blue line) we show the temperature as a function of column mass for this model photosphere. Obviously, the temperature decreases continuously outward.

3.2. Chromospheric models

We now extend the photospheric model following the approach of Short & Doyle (1997) and Fuhrmeister et al. (2005). In particular, we add three sections of rising temperature to the model photosphere, which represent the lower and upper chromosphere and the transition region. To technically facilitate the extension, we increase the number of atmospheric layers in the model from originally 64 to 100 layers.

Our model chromosphere is described by a total of six free parameters. The column mass density at the onset of the lower chromosphere, m_{min}, defines the location of the temperature minimum. The column mass densities and temperatures of the end points of the lower (log m_{mid}, T_{mid}) and the upper chromosphere (log m_{max}, T_{max}), and the temperature gradient in the transition region, grad$_{\mathrm{TR}}$, given by

$$\mathrm{grad}_{\mathrm{TR}} = \frac{\mathrm{d}\,T}{\mathrm{d}\,\log\,m} = \mathrm{const.} \quad (2)$$

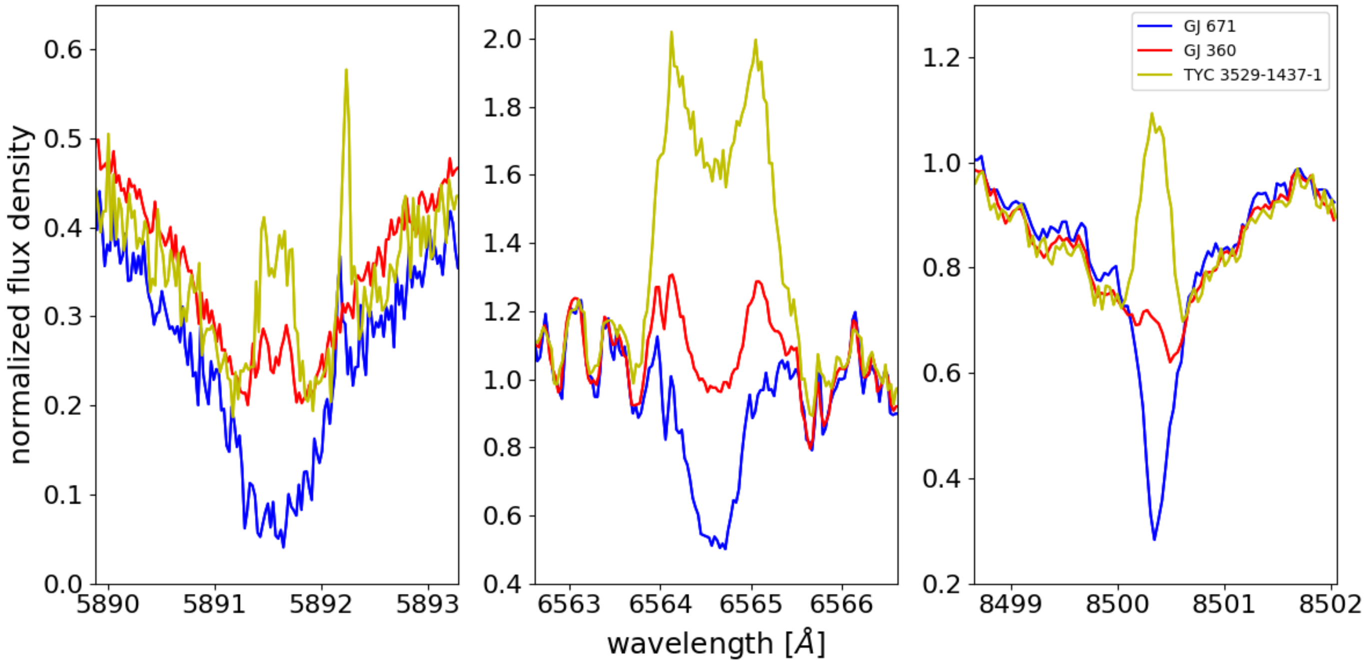

Fig. 4. Example spectra of one inactive (GJ 671, blue line), one semi-active (GJ 360, red line), and one very active star (TYC 3529-1437-1, yellow line) in the stellar sample in the range between Na I D_2, Hα, and the bluest Ca II IRT line. The peak right to the sodium line of TYC 3529-1437-1 is an airglow line.

as introduced by Fuhrmeister et al. (2005). The maximum temperature of the transition region is fixed at T_{TR} = 98 000 K. The temperature rise segments in the lower, upper chromosphere, and transition region are taken to be linear in the logarithm of the column mass density in our model. This is a rough approximation to the structure of the VAL C model. The meaning of the individual parameters is also illustrated in Fig. 5, where we show the temperature structure of the original photospheric model along with a modified structure including the photosphere, chromosphere, and transition region.

We used this modified temperature structure as a new starting point for the PHOENIX calculations. To account for the conditions in the chromosphere, the atomic species of H I, He I–II, C I–II, N I–V, O I–V, Na I–II, Mg I–II, K I–II, and Ca I–III are computed in non-LTE (NLTE) for all available levels taken from the database of Kurucz & Bell (1995)[3]. This applies to all species but He, for which we consulted CHIANTI v4 (Landi et al. 2006). The PHOENIX code iteratively adapts the electron pressure and mean molecular weight to reconcile these with the NLTE H I/H II ionization equilibrium. To that end, it is necessary that the population of all the states of the NLTE species are reiterated with the photoexciting and photoionizing radiation field, which is particularly important in the thin chromospheric and transition region layers. Moreover, the electron collisions have to be taken into account. A detailed comparison between LTE and NLTE atmospheric models is described by, for example, Short & Hauschildt (2003). Our calculations rely on the assumption of complete redistribution, as PHOENIX does not yet support partial redistribution, which would provide a more appropriate treatment in large parts of the chromosphere. However, its expected impact is largest for the Lyα line and resonance lines such as the Ca II H and K lines, which we also do not use in our study; the Na I D lines are much less affected (Mauas 2000).

[3] http://kurucz.harvard.edu/

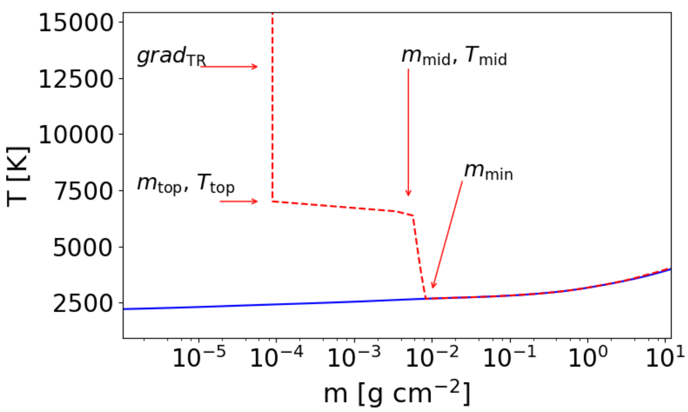

Fig. 5. Photosphere model (blue solid line) at $T_{\rm eff}$ = 3500 K, log g = 5.0 dex, [Fe/H] = 0 dex, and [α/Fe] = 0 dex taken from the Husser et al. (2013) library and an attached chromosphere model consisting of linear sections (red dashed line). The arrows indicate the variable parameters of the chromosphere model.

3.3. Hidden parameters

Besides the six parameters describing the temperature structure introduced in Sect. 3.2, there are further aspects of the model that can be modified and influence the solution, most importantly, the microturbulence and the chosen set of NLTE lines.

While in our models the photospheric microturbulent velocity is set to 2 km s^{-1}, in the chromosphere and the transition region the velocity is set to half the speed of sound in each layer, but is not allowed to exceed 20 km s^{-1} which may otherwise happen in the transition region. This follows the ansatz by Fuhrmeister et al. (2005). We do not smooth the microturbulent velocity transition between photosphere and chromosphere but the conditions in the model lead to quasi-smooth transitions with increases between two layers not exceeding 3 km s^{-1}. Varying the microturbulent velocity leads to changes in the intensity

Table 2. Parameter ranges for the chromosphere models.

Parameter	Minimum value	Maximum value
$m_{\rm min}$ (dex)	−4.0	−0.3
$m_{\rm mid}$ (dex)	−4.3	−1.5
$T_{\rm mid}$ (K)	3500	8000
$m_{\rm top}$ (dex)	−6.0	−3.5
$T_{\rm top}$ (K)	4500	8500
grad$_{\rm TR}$ (dex)	7.5	10.0

as well as in the shape of the spectral lines (Jevremović et al. 2000). The considered NLTE set is practically restricted by the computational effort. While a more comprehensive NLTE set including, for example, higher O and Fe species would certainly be desirable to improve the synthetic spectra, we consider the here-adopted NLTE set sufficient to model the chromosphere in the context of the investigated lines.

3.4. The model set

Our chromospheric model is described by six free parameters, and as a result of the rather large NLTE sets, each model calculation requires several dozens of CPU hours. While it may seem most straightforward to obtain a model grid homogeneously covering typical ranges for all free parameters, already a very moderate sampling of ten grid points per free parameter results in a grid with 10^6 elements, which results in too high a computational demand. It is also clear that the large majority of the grid points are expected to result in spectra nowhere near the observations, which would be of little use in the subsequent analysis.

The challenge was therefore to identify reasonable parameter ranges and to explore these with a number of models. To that end, we first calculated limiting cases, such as models simultaneously showing all spectral lines in absorption or emission, in other words inactive or active chromosphere models. By visual comparison with the observed spectra, we subsequently identified the most promising parameter ranges to be explored further.

A particularly interesting comparison is between models with a steep temperature rise in the lower chromosphere and a plateau in the upper chromosphere, and models with a shallow temperature increase in the lower chromosphere and a steeper increase in the upper chromosphere. The first type of model is similar in structure to the VAL models used for the Sun.

The final set of models used in this study comprises 166 models with different model parameter configurations. The parameters are varied in the ranges listed in Table 2, and the properties of the individual models are given in Table C.1. The activity levels of the models are given by the line index $I_{\rm Ca\,IRT}$ but, as shown in Sects. 3.6 and 3.7, Hα can behave differently compared to the Ca II IRT. Figure 6 shows an excerpt of the model set. The models in the upper panel have steep gradients in the lower chromosphere and shallow gradients in the upper chromosphere, and it turns out these models represent more inactive states. The models in the lower panel have the shallow gradients in the lower and the steep gradients in the upper chromosphere and are rather characteristic of active chromospheres.

3.5. Synthetic high-resolution spectra

To compare our models to stellar spectra, we need densely sampled synthetic spectra. We calculated the synthetic spectra in the spectral ranges of 3900–4000, 4830–4890, 5700–7000, and 8000–8800 Å with a sampling of $\Delta\lambda$ = 0.005 Å per spectral bin. These ranges comprise the chromospheric lines covered by CARMENES as discussed in Sect. 2.4 and additionally the Ca II H and K, Hϵ, and Hβ lines to enable a comparison to spectra obtained by other instruments such as the High Accuracy Radial velocity Planet Searcher (HARPS; Mayor et al. 2003) in the context of further investigations. For the comparison to the CARMENES spectra, we lowered the model spectral resolution to that of CARMENES by folding with a Gaussian kernel of the approximated width. The stellar rotational velocities are neglected because none of the sample stars is a fast rotator with $v \sin i$ never exceeding 4 km s^{-1} (Reiners et al. 2017; Jeffers et al. 2018). Even for the most active stars in our sample, relatively long rotation periods are not in contradiction with their activity. Newton et al. (2017) found the threshold between active and inactive stars (Hα in emission or absorption) for early M dwarfs to be at a rotation period of about 30 days. For two of our active dwarfs we have rotation period measurements by Díez Alonso et al. (2019): GJ 360 has a period of 21 days and TYC 3529-1437-1 has a period of 15.8 days. These periods are consistent with the corresponding $v \sin i$ values and there is no need to assume that they are seen pole-on.

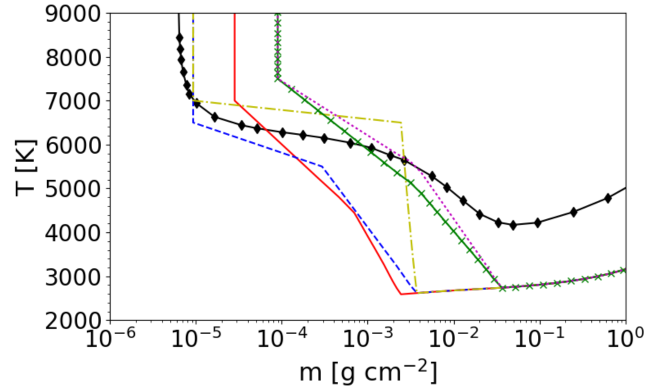

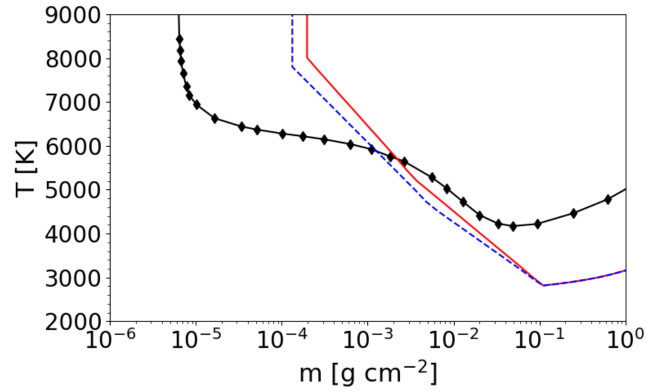

Fig. 6. *Upper panel*: temperature structure of the best single-component fits for the inactive stars as listed in Table A.1. Model #029 is shown by the red solid line, #042 by the blue dashed line, #047 by the yellow dash-dotted line, #079 by the green crossed line, and #080 by the magenta dotted line. *Lower panel*: same as in the upper panel for the active stars. Model #131 is plotted by the red solid line and #136 by the blue dashed line. The black solid diamond line shows the VAL C model for the Sun (Vernazza et al. 1981).

3.6. Sequences modeling the evolution of the chromospheric lines

The interaction of the parameters determines whether the chromospheric lines are in absorption or emission and determines the strengths and shapes of the lines. In order to obtain an impression

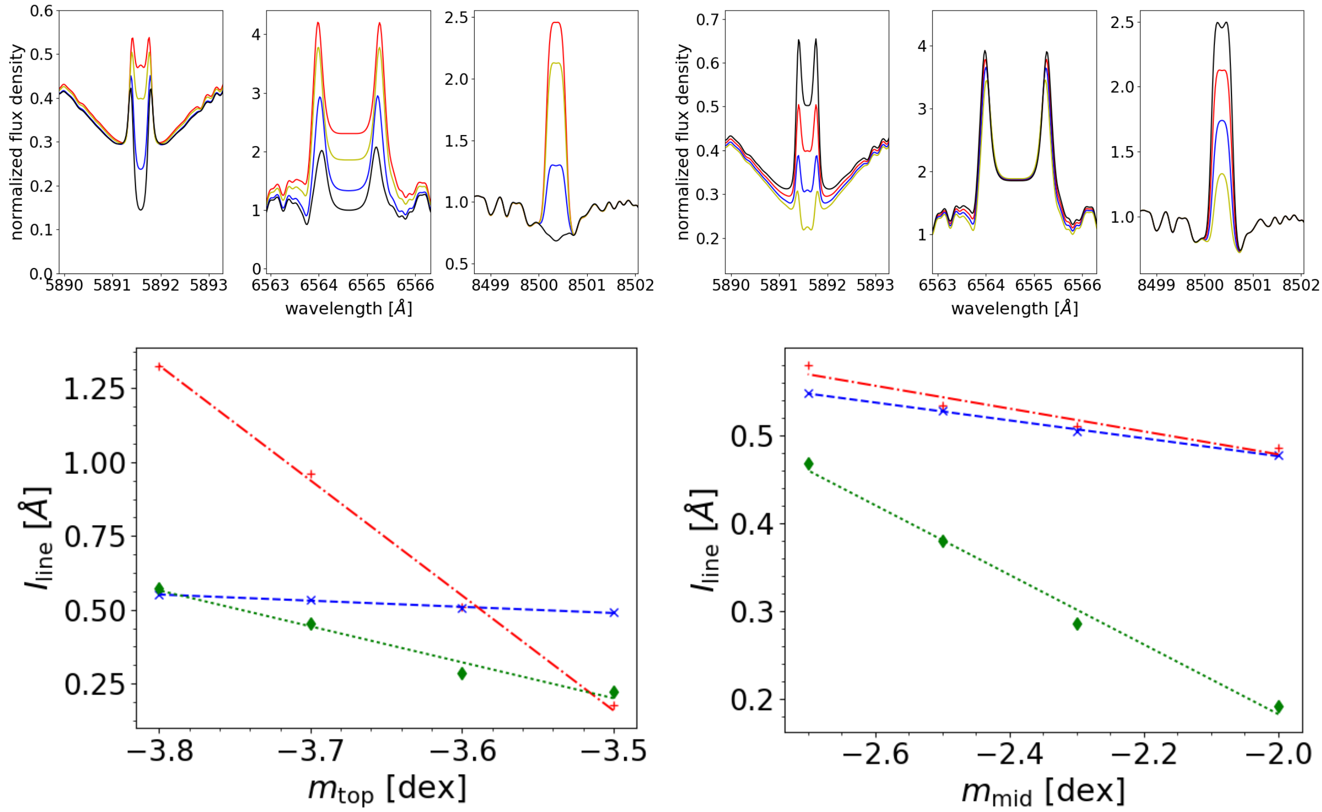

Fig. 7. *Top panels, left-hand side*: sequence of model spectra varying only the parameter $m_{\rm top}$ from −4.0 to −3.5 dex, the models are: #136 (black), #137 (blue), #138 (yellow), and #139 (red). *Top panels, right-hand side*: sequence for the parameter $m_{\rm mid}$ varying from −2.7 to −2.0 dex, models: #121 (yellow), #126 (blue), #138 (red), and #153 (black). *Bottom panels*: corresponding values of $I_{\rm line}$ against $m_{\rm top}$ for Na I D (blue crosses), Hα (red pluses), and Ca II IRT (green diamonds) for the top panels. Additionally the linear fits are plotted: the Na I D fit is plotted by the blue dashed line, the Hα fit by the red dash-dotted line, and the Ca II IRT fit by the green dotted line.

of how variations of a single parameter affect the line properties, we show in Fig. 7 the lines of Na I D_2, Hα, and the blue Ca II IRT line of different models only varying in the parameter $m_{\rm top}$ from −4.0 to −3.5 dex (left-hand side) and in $m_{\rm mid}$ from −2.7 to −2.0 dex (right-hand side). Changing a parameter of the upper chromosphere leads to stronger effects for Hα compared to Na I D and Ca II IRT, although the Ca II IRT is clearly more influenced than Na I D. The line indices illustrated in the lower panel confirm this impression with the gradients of the linear fits. However, the line core of Na I D_2 is filled up while the peaks are increasing less. The Hα and Ca II IRT lines completely go from absorption to emission, and simultaneously the Hα self-absorption becomes even stronger.

While Hα is almost not influenced by the variation of $m_{\rm mid}$, the Ca II IRT emission peak is approximately four times higher above the continuum for $m_{\rm mid} = -2.0$ dex than for $m_{\rm mid} = -2.7$ dex. The variation of Na I D is also visible in the spectra, but not as strong as for the Ca II IRT line. The strong self-absorption of Na I D leads to a smaller variation of the line index than for the Ca II IRT. This sequence suggests a weak relationship of the Hα formation to the mid-chromosphere, while the other two lines clearly depend on the structure of the transition between lower and upper chromosphere.

Furthermore, we also found the location $m_{\rm min}$ of the temperature minimum of the chromosphere to be a decisive factor to determine whether lines appear in absorption or emission. More active lines are generated with a temperature minimum at higher density as found by Short & Doyle (1998) who calculated a model grid for the chromospheric lines of Hα and Na I D in five M dwarfs.

3.7. Flux contribution functions

Performing sequences indicates that modeling the chromospheric lines of Na I D_2, Hα, and the bluest Ca II IRT line turns out to be a challenge mainly due to different formation heights of the line wings and cores in the chromosphere. Therefore, we investigated where the lines form in order to improve the understanding of the chromospheric structure and to make restrictions for the calculations of the chromospheres. The PHOENIX code is capable of computing flux contribution functions following the concept of Magain (1986) and Fuhrmeister et al. (2006). The intensity contribution function $\mathscr{C}_I$ is defined by

$$\mathscr{C}_I(\log m) = \mu^{-1} \ \ln 10 \, m \, \kappa \, S \, e^{-\tau/\mu}, \tag{3}$$

where m is the column mass density, κ the absorption coefficient, S the source function, τ the optical depth, and $\mu = \cos\theta$, with θ as the angle between the considered direction and surface normal. The flux contribution function C is the intensity contribution function integrated over all μ and it gives information on where the flux density of every computed wavelength in the stellar atmosphere arises from. Figure 8 illustrates the flux contribution function of the line core (upper panel) and wing (mid-panel) of the bluest Ca II IRT line for model #080 (see Table C.1). Additionally, the source function S_ν, Planck function B_ν, and intensity J_ν are given in the plots. The core is formed nearly at the center of the upper chromosphere at $T = 6200$ K. In the lower panel the temperature structure of the model is shown to visualize at which temperatures the lines are formed and the formation regions of Na I D_2, Hα and the Ca II IRT line are given. The formation region is defined as the full width at

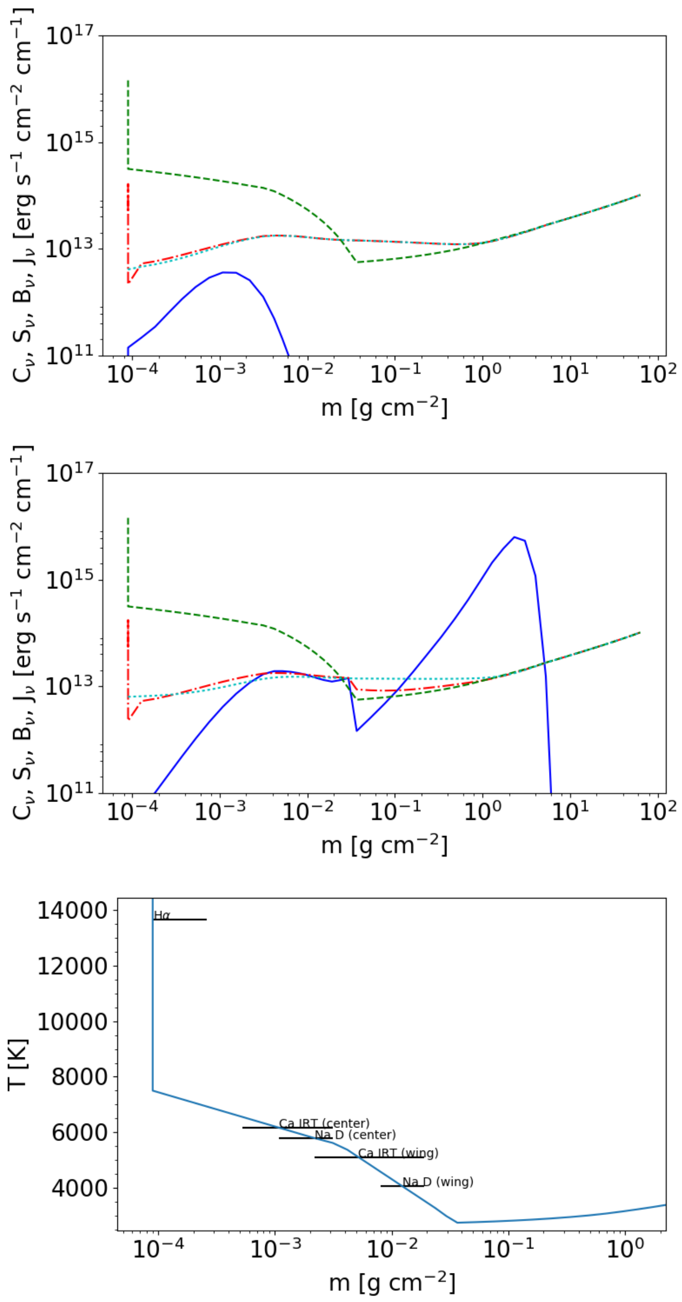

Fig. 8. *Upper and middle panels*: scaled flux contribution function C_ν (solid blue), source function S_ν (dash-dotted red), Planck function B_ν (dashed green), and intensity J_ν (dotted cyan) for $\lambda = 8500.36$ Å representing the line core (upper panel) and $\lambda = 8500.54$ Å in the line wing (mid-panel) of the Ca II IRT line in model #080. The peak at high column mass in the contribution function of the line wing shows that the photospheric flux already dominates at this wavelength but there is still some chromospheric contribution. *Lower panel*: temperature structure of model #080 and the formation regions of Na I D_2, Hα, and the bluest Ca II IRT line.

half maximum around the maximum of the contribution function above the photosphere. The Na I D_2 core is formed in the transition between the lower and upper chromosphere at $T = 5800$ K, while the Hα core is formed at the top of the chromosphere at $T = 13700$ K. This is in agreement with the results from the best-fit model by Fuhrmeister et al. (2005) for AD Leo in Na I D and Hα.

4. Results and discussion

4.1. Comparing synthetic and observed spectra

To compare our synthetic spectra to observations we focus on the Na I D_2, Hα, and the bluest Ca II IRT lines. Before carrying out the comparison, the flux densities of the observed and synthetic spectra were normalized to the mean value in the blue reference bands of the respective chromospheric line (see Sect. 2.4). For stars with several available spectra, we used the spectrum with the median value of the $I_{\mathrm{Ca\,IRT}}$ line index for comparison.

Our comparison is based on a least-squares-like minimization. In particular, we consider the difference between the observed and synthetic spectra simultaneously in the wavelength ranges $\lambda_{\mathrm{NaD}} \pm 0.2$, $\lambda_{\mathrm{H}\alpha} \pm 0.8$ and $\lambda_{\mathrm{CaIRT}} \pm 0.25$. These line bands cover the chromospheric cores of the respective spectral lines. In Fig. 9 we show the best-fit models to the individual lines of TYC 3529-1437-1 irrespective of the other two lines. In the case of the Ca II IRT line, the best-fit model (yellow line) produces an almost perfect match to the observed line core, however, a comparison of this model to the shape of Na I D and Hα shows clear mismatches with regard to the data. While the predicted Hα line shows too strong an emission, the core of the associated Na I D line profile is strongly absorbed, which is clearly at odds with the observation. However, it is possible to obtain good fits for each of the three lines individually using appropriate models.

For physical reasons, the line band used for the Hα line is nearly three times as wide as that of the Ca II IRT line and four times wider than that of the Na I D_2 line. Moreover, the observed (and modeled) amplitude of variation in these line profiles is by far largest for the Hα line. Both factors boost the weight of the Hα line profile in the minimization based on the summed χ^2 values obtained in the three line bands as the objective. This reflects a relative overabundance of data in the Hα line and makes it the dominant component in such a fit. However, we intend to find the model that provides the most appropriate representation of all three considered chromospheric lines simultaneously.

Therefore, we constructed a dedicated statistic, χ_m^2, which we use as the objective function in our minimization. Specifically, we define

$$\chi_m^2 = \chi_{\mathrm{H}\alpha}^2 + w_{\mathrm{Na}}\chi_{\mathrm{Na}}^2 + w_{\mathrm{Ca}}\chi_{\mathrm{Ca}}^2, \tag{4}$$

where $\chi_{\mathrm{H}\alpha}^2$, χ_{Na}^2, and χ_{Ca}^2 denote the sum of squared differences between model and observation obtained in the individual line bands. The weighting factors w_{Na} and w_{Ca} were adapted to give approximately the same weight to all three lines in the minimization. To counterbalance the different widths of the line bands we increase the weighting of the Na I D_2 and Ca II IRT line bands by a factor of 3. To account for the different flux density scales of variation in the Na I D_2 and Ca II IRT lines, an additional factor of 4 is added to further increase their weight. The factor of 4 was estimated based on the observed amplitude of variation of the Hα line compared to the variation of the Na I D_2 and Ca II IRT lines. We therefore end up with weighting factors of $w_{\mathrm{Na}} = w_{\mathrm{Ca}} = 12$. The resulting χ_m^2 statistic establishes a relative order among the model fits, but cannot be used as a goodness-of-fit criterion.

4.2. Single-component fits

In a first attempt, we directly compare our set of synthetic spectra with the observations using the modified χ_m^2 criterion defined above. Since we normalize both the model and observation using the same reference band, no free parameters in this comparison remain; however, we compare every observed spectrum to

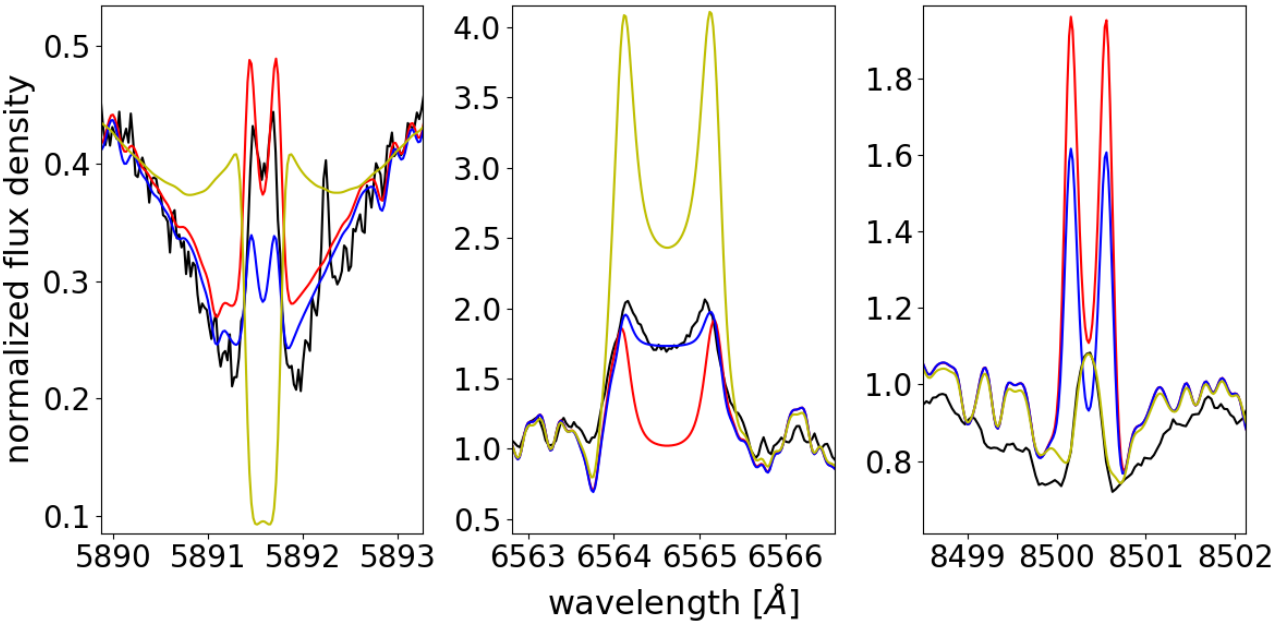

Fig. 9. Comparison of the observed median activity spectrum of TYC 3529-1437-1 (black) as given by $I_{\mathrm{Ca\,IRT}}$ to the model spectrum fitting best in a single line. Best-fit models using only Na I D_2 are denoted in red (model #078), using only Hα in blue (model #073), and Ca II IRT in yellow (model #157).

all spectra from our set of models. Table A.1 lists the results of the single model fits for the whole stellar sample, i. e., the models with the lowest modified χ_m^2 value. An inspection of Table A.1 shows that this approach yields reasonable fits with χ_m^2 values between 1.8 and 4.04 for most stars, while four stars, the outliers in Fig. 1, show only poor fits with χ_m^2 values in excess of 10.

4.2.1. Inactive stars

For the inactive stars in our sample interestingly a small subset of five models provides the best fits, viz., the models #029 (2 cases), #042 (13 cases), #047 (12 cases), #079 (9 cases), and #080 (10 cases). In the lower panel of Fig. 2, the distribution of inactive stars is shown in the plane spanned by the Hα and Ca IRT activity indices. The color coding identifies the best-fitting models from Table A.1. While for most of the stars with $I_{\mathrm{Ca\,IRT}} < 0.625$ model #080 is the best from our set, the spectra of the majority of stars exceeding this value are best represented by model #042. The two stars Ross 730 and HD 349726, which we consider the most inactive in our sample (see Sect. 2.4), are best represented by model #029. The modified χ_m^2 values range between 1.8 and 4.5 for the inactive stars.

As an example, we juxtapose the best-fitting models and observed spectra of the two inactive stars GJ 671 and EW Dra in Fig. 10. In these models as well as in the observations all the considered lines appear in absorption. We note that the observation of the sodium line of GJ 671 shows some telluric emission, however, sufficiently offset from the line core. From our point of view, the #042 provides a reasonable fit to all considered lines in the case of GJ 671. Despite some shortcomings, such as a too deep Ca IRT line in the model and a somewhat too narrow sodium trough, all aspects of the data are appropriately reproduced by the model spectrum.

For the case of EW Dra, the overall situation is less comfortable. The strongest deviation of model #080 from the observed spectrum of EW Dra is the width of the central part of the Na I D_2 line. The model clearly produces a too wide line with a signature of a central fill-in and self-absorption clearly more pronounced than in the observation. We emphasize, however, that despite these differences, the observation shows a similar structure in the line core, yet of course less pronounced. The line shapes of the Hα and the Ca II IRT line are well represented by this model although in particular the observed Hα line is deeper than that predicted by the model.

Although there are shortcomings, we conclude that the spectra of inactive stars can be appropriately represented by our models. Notably, all best-fit models for inactive stars are characterized by a temperature structure with a steeper temperature rise in the lower chromosphere and a more shallow rise in the upper chromosphere. This is in fact not very different from the VAL C model (Vernazza et al. 1981) for the Sun, which also shows a steeper temperature rise in the lower chromosphere and a plateau in the upper chromosphere.

4.2.2. Active stars

For the active stars in our sample we only need two models that provide the best fits, viz., the models #131 (2 cases) and #136 (2 cases). In Fig. 11 we show the observed spectra and best-fit models for the more active stars GJ 360 and TYC 3529-1437-1, and clearly, in both cases the modified χ_m^2 values are more than twice as high as for any inactive star in the sample. The observed Na I D line profiles show self-absorption in both stars, which is also predicted by the model, but the width of the emission core is too broad for the models and the self-absorption is too strong. The observed Hα lines of both stars show clear self-absorption. This aspect is reproduced by the models, although for GJ 360 the model strongly overpredicts the self-absorption. The overall Hα line profile seems more appropriate for TYC 3529-1437-1, although the model yields a line that is too strong. The shape of the Ca II IRT line in the model is roughly reproduced in GJ 360; the model for TYC 3529-1437-1 shows considerable self-absorption, which is not observed. In particular for the more active stars, it is hard to fit all three lines simultaneously by one model.

The column mass densities of the temperature minima m_{min} of the best-fit models of the active stars are obviously higher

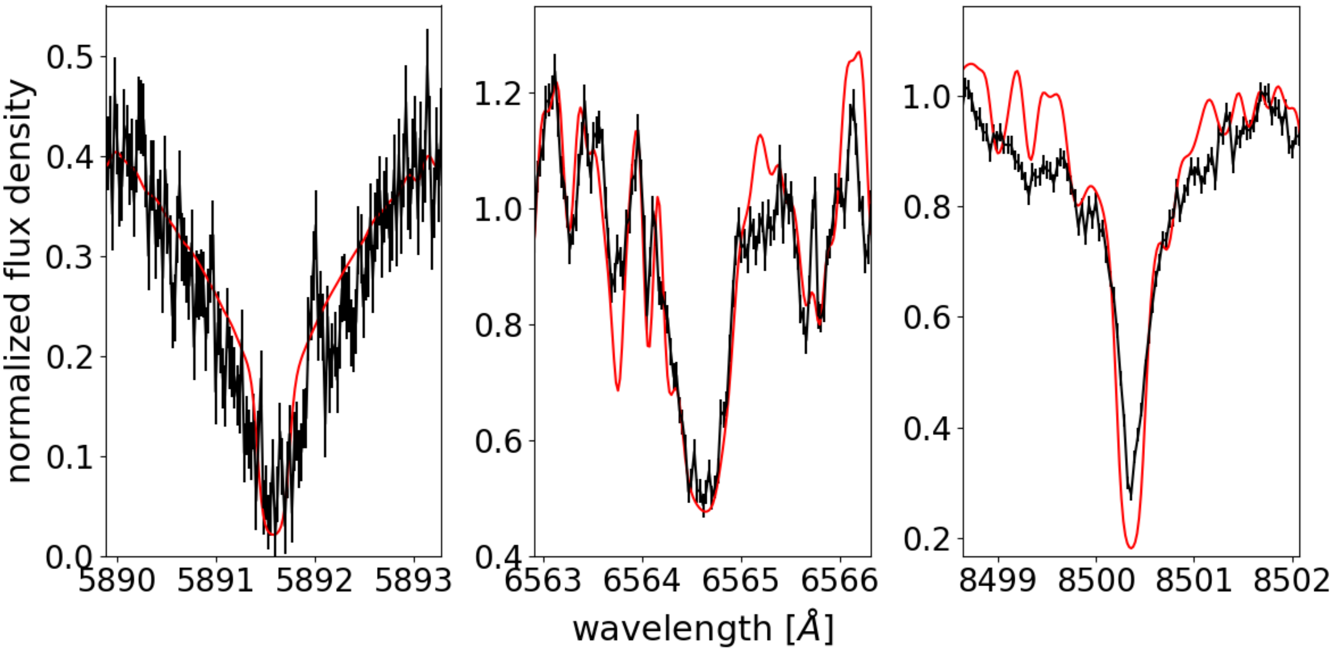

Fig. 10. Comparison of the best-fit model spectrum (red) to the observed spectrum (black) with median activity as defined by $I_{\mathrm{Ca\,IRT}}$. *Upper panels*: GJ 671 and model #042. *Lower panels*: EW Dra and model #080.

compared to the models of the inactive stars. Both models have a density of at least $\Delta m_{\mathrm{min}} = 0.5$ dex higher than the found inactive models. In notable contrast to our results for the inactive stars, the best-fit models for the spectra of the more active stars tend to show a more shallow rise in the lower chromosphere and a steeper rise in the upper chromosphere. It is possible to increase the flux of the Hα and Na I D_2 lines by only moving the chromosphere to increasing densities, but the shape of the chromosphere needs to be changed to reconcile a more active chromosphere with the Ca II IRT line. Although this result has to be viewed against the background of the shortcomings of the fit, we tentatively identify this reversal of gradients as a characteristic change in the chromospheric temperature structure associated with a change from an inactive to an active chromosphere.

4.3. Linear-combination fits

The solar chromospheric spectrum is well known for varying across the solar disk, in particular, when active regions and quiet regions are compared. To account for this fact, some studies using one-dimensional static models have combined models applying a filling factor. This method was first applied using models with a thermal bifurcation by Ayres (1981) to account for observations of molecular CO in the solar spectrum. However, it cannot be explained by chromospheric models alone, which have a temperature minimum well above a temperature allowing for CO. Such studies normally use linear combinations of a photospheric (or inactive chromospheric) and an active chromospheric model and have also been used for flare

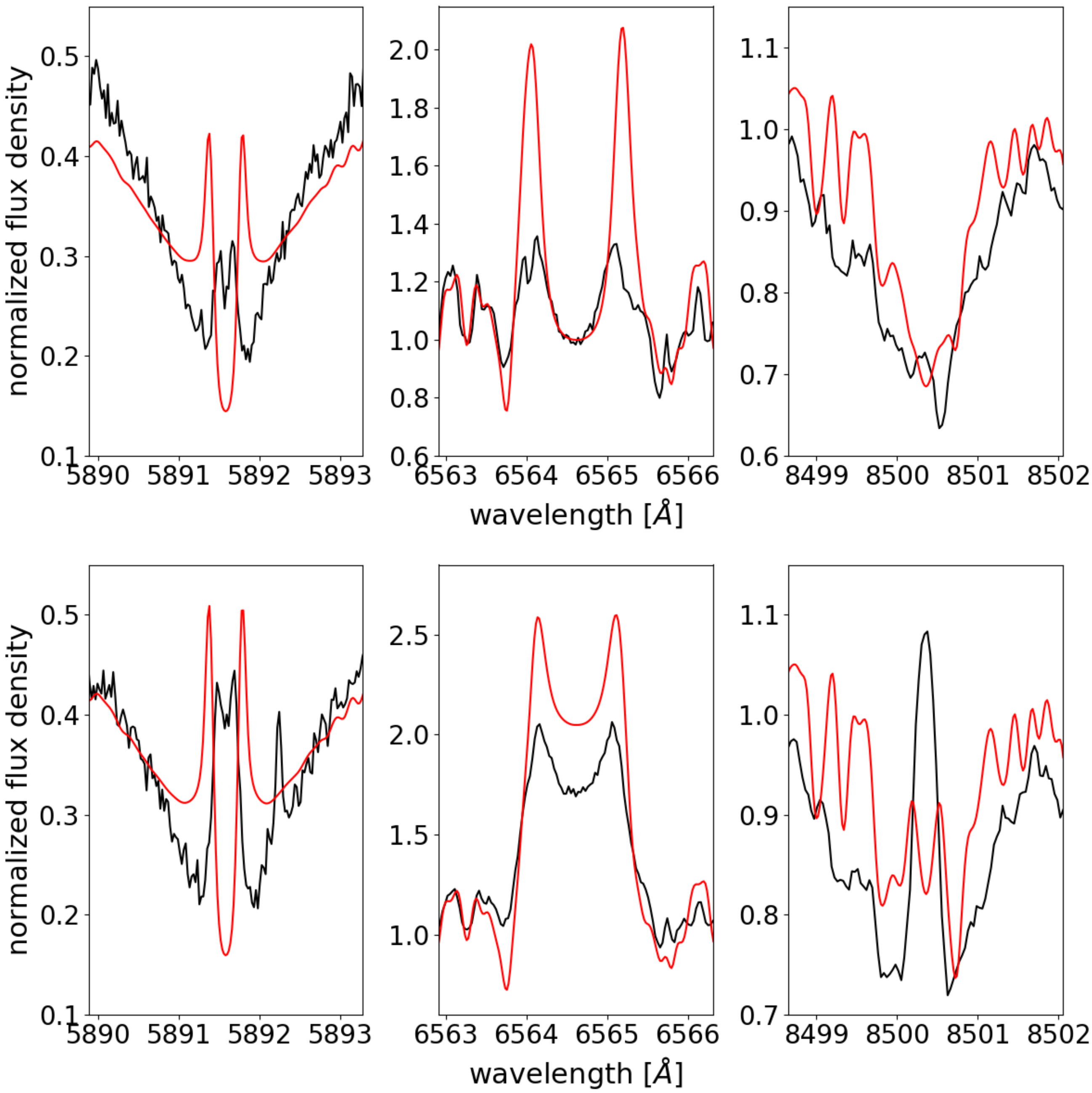

Fig. 11. Same as Fig. 10. *Upper panels*: GJ 360 and model #136. *Lower panels*: TYC 3529-1437-1 and model #131.

modeling (Fuhrmeister et al. 2010). Classically this treatment is also known as 1.5D modeling, since it tries to account for the inhomogeneity of the stellar atmospheres (Ayres et al. 2006). It relies on the assumption that the individual components are independent and influence each other neither radiatively nor collisionally via NLTE. This assumption would be satisfied if these regions were optically thick, which they are most probably not, but neither are they too optically thin. Therefore, we consider the assumption to be approximately satisfied.

We also adopt this approach in an attempt to improve especially the spectral fits of the more active dwarfs in our sample. In particular, we consider a linear combination of an inactive and an active spectral model, and determine a best-fit filling factor by again minimizing the modified χ_m^2 value. This analysis is done for the whole stellar sample from Table 1, and Table A.2 summarizes the results. The latter table contains the filling factors of the inactive and active component and the associated modified χ_m^2 values. Although these values do not represent classical χ^2 values, they can be compared with those of the single model fits (see Table A.1). As expected, the modified χ_m^2 values improve for every star when a second component is added to the model. Table A.2 also lists the differences of the Ca II IRT line indices ($\Delta I_{\mathrm{Ca\,IRT}}$) between the inactive and active model in the best combination fits giving an impression of the contrast in the respective combinations.

4.3.1. Inactive stars

In the spectral fits of the inactive sample stars, we start with the best-fit single-component model as the first component. We then add every model of our model set, determine a best-fit filling factor, and finally, choose the model combination providing the minimum modified χ_m^2. The thus determined second model component mostly also exhibits the Na I D$_2$, Hα and the Ca II IRT

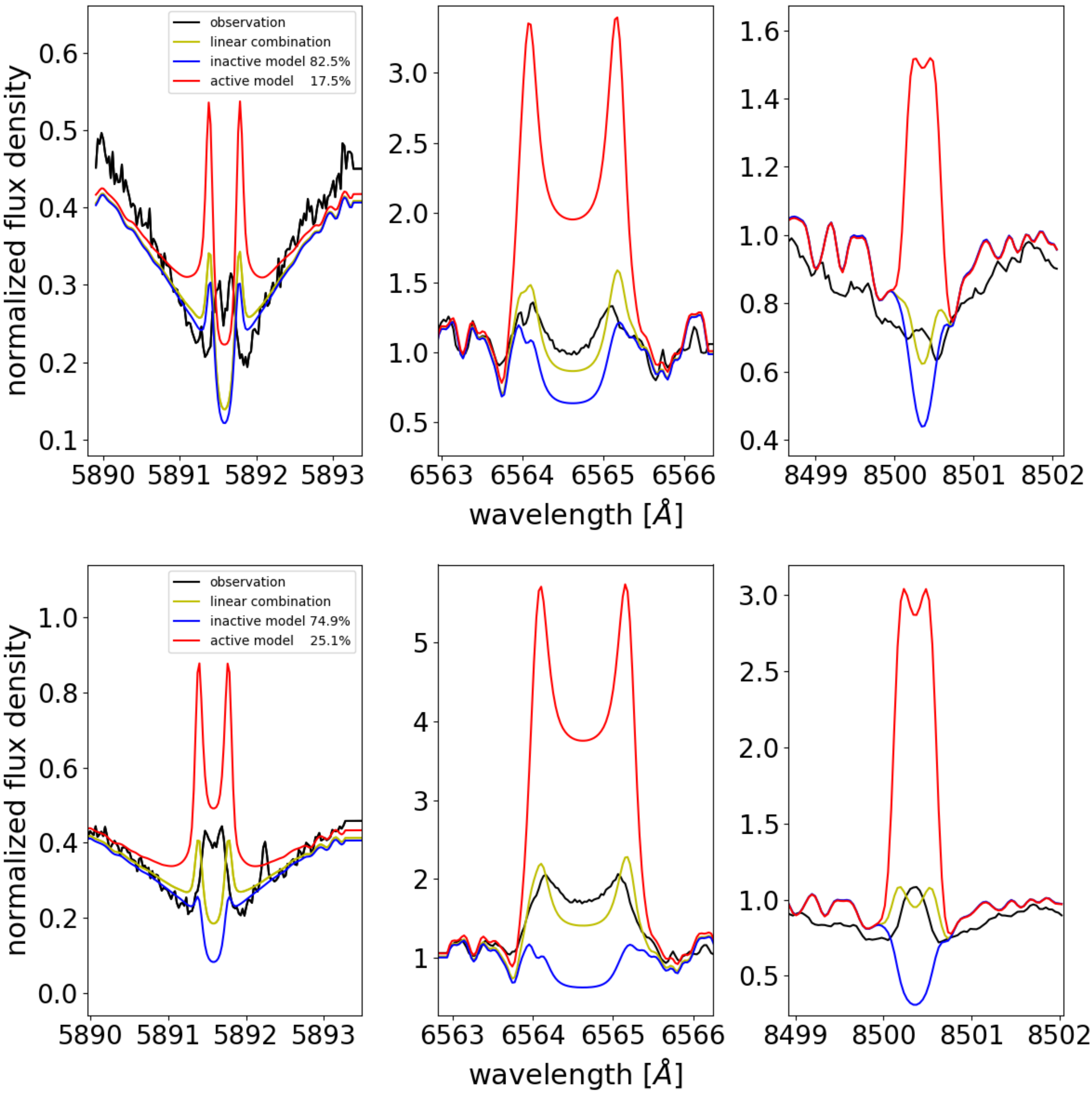

Fig. 12. Comparison of the observed median activity spectrum to the best linear-combination fits for GJ 360 (*upper panels*, inactive model #080 and active model #132) and TYC 3529-1437-1 (*lower panels*, inactive model #079 and active model #149). The line of Na I D_2 and the bluest Ca II IRT line are weighted by a factor of 12, respectively, compared to Hα as described in Sect. 4.1.

lines in absorption. Although the combination leads to better matching of the line shapes, the overall improvement obtained for the inactive stars remains moderate.

4.3.2. Active stars

The spectra of the active stars could not be reproduced well with our single-component fits. Therefore, we do not consider the best-fit single model component as a good starting point for the fit as for the inactive stars and, instead, apply the following procedure. As the inactive spectral model component, we subsequently tested the five models, which produced the best fits for the inactive stars in the single-component approach (see Sect. 4.2). These were then tentatively combined with all other models from our set and the filling factor determined. Again, we finally opted for that combination providing the minimum modified χ^2_m value.

The best χ^2_m value is obtained by the combination with models with differences regarding the temperature structure in comparison to the found inactive models. The temperature gradient of the lower chromosphere is shallower and that of the upper chromosphere is steeper, which is the reverse case for the five best models of the inactive stars. While the active models of G 234-057 and GJ 360 have higher gradients in the upper than in the lower chromosphere, in the active model of LP 733-099 and TYC 3529-1437-1 the gradients of the lower and upper chromosphere are equal, meaning the chromosphere consists of only one linear section. Furthermore, in each of these active models the whole chromosphere is shifted inward about $\Delta m = 0.5$ dex compared to the inactive models. The width of the chromosphere nearly remains the same in every case, but the temperature at the top of the chromosphere increases at least by about 300 K. The interaction of the free parameters yields chromospheric emission lines in the corresponding synthetic spectra, i. e. varying only one parameter does not necessarily yield all the chromospheric lines in emission. In particular, the contribution function of PHOENIX can provide information about where the lines are formed, as discussed in Sect. 3.7.

In these three active models all three investigated lines clearly appear in emission. In Fig. 12, we show the observed spectrum of TYC 3529-1437-1 with median activity as given by $I_{\rm Ca\,IRT}$, the spectra of the inactive and active model, and the best linear-combination spectral fit of the two models to the observed spectrum. From the modified χ^2_m and in comparison to Fig. 11 it becomes obvious that the combination provides a better representation of the observation than the best-fit single model. In Fig. 12 we also show the linear-combination fit for the spectrum of GJ 360. Again the linear combination gives a better fit to the shape of the Na I D_2 and Hα lines. However, reproducing the transition from absorption to emission in the Ca II IRT line also turns out to be hard with this method. While in the fit for TYC 3529-1437-1 the inactive model spectrum contributes 75%, the filling factors for the moderately more active LP 733-099 yields 68% for the inactive and 32% for the active component. The semi-active stars G 234-057 and GJ 360 exhibit filling factors of 90 and 82% for the inactive chromospheric model. We therefore conclude that the resulting filling factors of the active model component match the activity levels of the stars as determined from spectral indices.

4.4. Filling factor as a function of activity level

To study the relationship between the activity state and the filling factors in individual stars, we perform an analysis of a set of available CARMENES spectra, considering the restrictions described in Sect. 2.3, of a subsample of stars. This subsample consists of all active stars and those inactive stars from which we have used more than five spectra and that show variability in the flux density of the considered chromospheric lines. We determine filling factors based on fits to all used CARMENES spectra, following the same method as in Sect. 4.3, but fix the combination of models to the pair previously determined.

In Fig. 13 we show the filling factor of the inactive model component as listed in Table A.2 as a function of the $I_{\rm Ca\,IRT}$. Our modeling yields a decrease in the filling factor of the inactive chromospheric component as the level of activity rises (i.e. $I_{\rm Ca\,IRT}$ decreases), but even for LP 733-099, the most active star in our sample, the filling factor of the inactive model component remains as high as ~65%. While this indicates that the major fraction of its surface is not covered with active chromosphere, we caution that our two-component approach remains a highly simplified description of the chromosphere. In the case of the inactive stars, the interpretation of the filling factor in Table A.2 is more complicated. In particular, combinations of two inactive chromospheric components possibly yield formally large filling factors for either component.

In the upper panel of Fig. 13 we show the relation between the Ca IRT index, $I_{\rm Ca\,IRT}$, and the filling factor for the active stars LP 733-099, TYC 3529-1437-1, GJ 360, G 234-057. There is a clear relation between $I_{\rm Ca\,IRT}$ and the filling factor in all these stars, which can well be approximated by a linear trend (see Fig. 13). This trend can also be seen for most of the inactive stars considered in this study, some of these are plotted in the lower panel of Fig. 13. The filling factor of the inactive model decreases with increasing activity level.

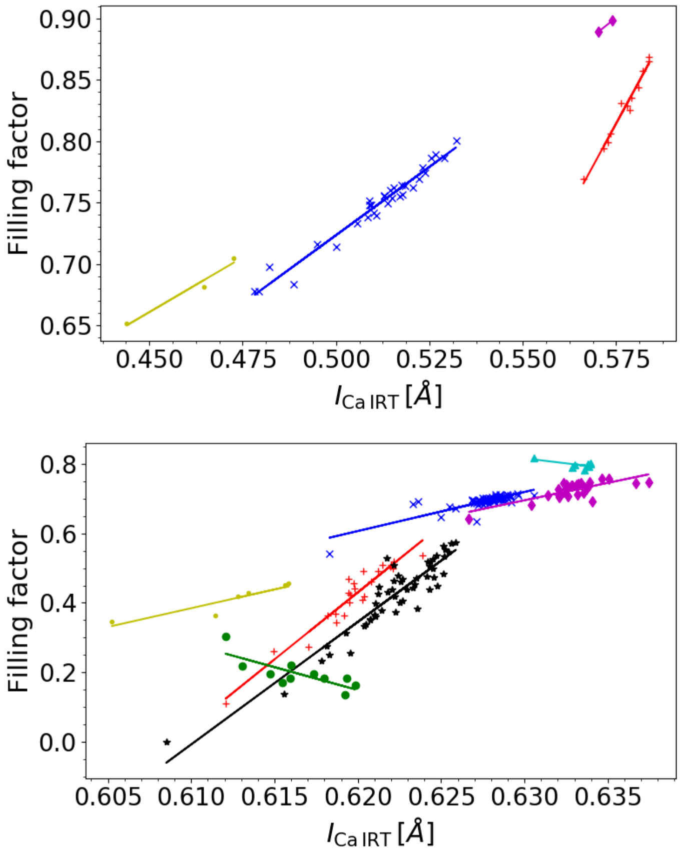

Fig. 13. *Upper panel*: filling factors of the inactive models in the combination fits as a function of $I_{\rm Ca\,IRT}$ of the four active stars LP 733-099 (yellow dots), TYC 3529-1437-1 (blue crosses), GJ 360 (red pluses), and G 234-057 (magenta diamonds) are shown. *Lower panel*: same as in the upper panel for Ross 905 (blue crosses), EW Dra (red pluses), LP 743-031 (yellow dots), GJ 625 (magenta diamonds), BD+70 68 (black asterisks), Ross 730 (cyan triangles), and GJ 793 (green circles). The solid lines show the linear fits of the stars. To improve clarity, the errors of $I_{\rm Ca\,IRT}$ are not shown.

Therefore linear regressions are performed to reveal the following linear trends:

$$\mathrm{FF}_{\rm star} = a + b\left(I_{\rm Ca\,IRT} - \overline{I_{\rm Ca\,IRT}}\right) \tag{5}$$

for the filling factor ($\mathrm{FF}_{\rm star}$) as a function of $I_{\rm Ca\,IRT}$, where $\overline{I_{\rm Ca\,IRT}}$ is the mean $I_{\rm Ca\,IRT}$ of the respective star. The gradients are denoted by b and the intercepts by a, and the uncertainties on the coefficients (σ_b and σ_a) were estimated using the Jackknife method (Efron & Stein 1981). For example, the application of a linear regression for GJ 360 yields $a = 0.83 \pm 0.0015$ and $b = 5.59 \pm 0.28$ Å^{-1}. Table B.1 lists the results of the linear regressions of our study. For nearly all of the subsample stars we obtain clear positive gradients. Ross 730 and Wolf 1014 show a slight negative trend that cannot be distinguished from noise as visible in the comparably high relative errors. The negative slope of Ross 730 is dominated by a single outlier data point. Therefore, GJ 793 is the only star for which we find a significant negative gradient. In this case model #080 is more active than model #112 according to $I_{\rm Ca\,IRT}$, although it is the opposite for Hα. The variation of Hα in GJ 793 leads the linear-combination method to give model #112 a higher weight with increasing activity state of GJ 793. The particular model combination is the reason for the negative slope of GJ 793.

Interestingly, the range of filling factors of the inactive part for the active stars shown in Fig. 13 is comparable irrespective of their activity level. However, with increasing $I_{\mathrm{Ca\,IRT}}$ the gradient of the relationship appears to increase except for G 234-057 from which we only used two spectra. Therefore, compared to an active star, the same change in filling factor in an inactive star produces only a comparably weak response in the Ca IRT line index, $I_{\mathrm{Ca\,IRT}}$. In our modeling, this results from a stronger contrast between inactive and active chromospheric components in active stars, which is also indicated by the differences of the Ca II IRT line indices as given in Table A.2.

5. Conclusions

We have calculated a set of one-dimensional parametrized chromosphere models for a stellar sample of M-type stars in the effective temperature range 3500 ± 50 K. The synthetic spectra of single models have turned out to be able to represent inactive stars in the lines of Na I D_2, Hα, and a Ca II IRT line simultaneously, while a linear combination of at least two models is needed to simultaneously approach the chromospheric lines of active stars, suggesting that the enhanced activity originates only in parts of the stellar surface – as though the Sun is covered partially in active regions. The shape of the temperature structure of the models representing the inactive stars is comparable to the VAL C model for the Sun. A steep temperature gradient in the lower chromosphere is followed by a plateau-like structure in the upper chromosphere. Our best-fit inactive models resemble this general structure of the VAL C model, but the temperatures and column mass densities differ, of course.

Concerning the models representing the active regions of the four active stars in our sample, the temperature structure rather indicates a steeper temperature gradient in the upper chromosphere than a plateau-like structure. The deduced filling factors of inactive and active models correspond to the activity levels of the active stars under the constraint of the model combination. Furthermore, the variable stars revealed a linear relationship between the filling factors and the line index in the Ca II IRT line, i. e. the higher the activity state, the less the coverage of the inactive chromosphere. The gradients of the filling factors of the variable stars depend on the model combinations, hence the gradients are not evenly distributed, but they only vary in their absolute value. Moreover, the model combination analysis also indicates an increasing contrast between the inactive and active regions with increasing level of activity.

Acknowledgements. D.H. acknowledges funding by the DLR under DLR 50 OR1701. B.F. acknowledges funding by the DFG under Cz 222/1-1 and Schm 1032/69-1. S.C. acknowledges support through DFG projects SCH 1382/2-1 and SCHM 1032/66-1. CARMENES is an instrument for the Centro Astronómico Hispano-Alemán de Calar Alto (CAHA, Almería, Spain). CARMENES is funded by the German Max-Planck-Gesellschaft (MPG), the Spanish Consejo Superior de Investigaciones Científicas (CSIC), the European Union through FEDER/ERF FICTS-2011-02 funds, and the members of the CARMENES Consortium (Max-Planck-Institut für Astronomie, Instituto de Astrofísica de Andalucía, Landessternwarte Königstuhl, Institut de Ciències de l'Espai, Institut für Astrophysik Göttingen, Universidad Complutense de Madrid, Thüringer Landessternwarte Tautenburg, Instituto de Astrofísica de Canarias, Hamburger Sternwarte, Centro de Astrobiología and Centro Astronómico Hispano-Alemán), with additional contributions by the Spanish Ministry of Science [through projects AYA2016-79425-C3-1/2/3-P, ESP2016-80435-C2-1-R, AYA2015-69350-C3-2-P, and AYA2018-84089], the German Science Foundation through the Major Research Instrumentation Programme and DFG Research Unit FOR2544 "Blue Planets around Red Stars", the Klaus Tschira Stiftung, the states of Baden-Württemberg and Niedersachsen, and by the Junta de Andalucía. We thank J. M. Fontenla for providing us with the atmospheric structure of his chromospheric model for GJ 832 (Fontenla et al. 2016) for comparison purposes. CHIANTI is a collaborative project involving George Mason University, the University of Michigan (USA) and the University of Cambridge (UK).

References

Allard, F., & Hauschildt, P. H. 1995, ApJ, 445, 433
Alonso-Floriano, F. J., Morales, J. C., Caballero, J. A., et al. 2015, A&A, 577, A128
Ayres, T. R. 1981, ApJ, 244, 1064
Ayres, T. R., Plymate, C., & Keller, C. U. 2006, ApJS, 165, 618
Caballero, J. A., Cortés-Contreras, M., Alonso-Floriano, F. J., et al. 2016a, in 19th Cambridge Workshop on Cool Stars, Stellar Systems, and the Sun (CS19), 148
Caballero, J. A., Guàrdia, J., López del Fresno, M., et al. 2016b, in Observatory Operations: Strategies, Processes, and Systems VI, Proc. SPIE, 9910, 99100E
Cram, L. E., & Mullan, D. J. 1979, ApJ, 234, 579
De Gennaro Aquino, I. 2016, Ph.D. Thesis, University of Hamburg, Hamburg, Germany
Díez Alonso, E., Caballero, J. A., Montes, D., et al. 2019, A&A, 621, A126
Efron, B., & Stein, C. 1981, Ann. Stat., 9, 586
Fontenla, J. M., Linsky, J. L., Witbrod, J., et al. 2016, ApJ, 830, 154
France, K., Loyd, R. O. P., Youngblood, A., et al. 2016, ApJ, 820, 89
Fuhrmeister, B., Schmitt, J. H. M. M., & Hauschildt, P. H. 2005, A&A, 439, 1137
Fuhrmeister, B., Short, C. I., & Hauschildt, P. H. 2006, A&A, 452, 1083
Fuhrmeister, B., Schmitt, J. H. M. M., & Hauschildt, P. H. 2010, A&A, 511, A83
Fuhrmeister, B., Czesla, S., Schmitt, J. H. M. M., et al. 2018, A&A, 615, A14
Hauschildt, P. H. 1992, J. Quant. Spectr. Rad. Transf., 47, 433
Hauschildt, P. H. 1993, J. Quant. Spectr. Rad. Transf., 50, 301
Hauschildt, P. H., & Baron, E. 1999, J. Comput. Methods Appl. Math., 109, 41
Hauschildt, P. H., Allard, F., & Baron, E. 1999, ApJ, 512, 377
Husser, T.-O., Wende-von Berg, S., Dreizler, S., et al. 2013, A&A, 553, A6
Jeffers, S. V., Schöfer, P., Lamert, A., et al. 2018, A&A, 614, A76
Jevremović, D., Doyle, J. G., & Short, C. I. 2000, A&A, 358, 575
Kuridze, D., Henriques, V., Mathioudakis, M., et al. 2015, ApJ, 802, 26
Kurucz, R. L., & Bell, B. 1995, Atomic Line List (Cambridge, MA: Smithsonian Astrophysical Observatory)
Landi, E., Del Zanna, G., Young, P. R., et al. 2006, ApJS, 162, 261
Lépine, S., Hilton, E. J., Mann, A. W., et al. 2013, AJ, 145, 102
Magain, P. 1986, A&A, 163, 135
Martin, J., Fuhrmeister, B., Mittag, M., et al. 2017, A&A, 605, A113
Martínez-Arnáiz, R., López-Santiago, J., Crespo-Chacón, I., & Montes, D. 2011, MNRAS, 414, 2629
Mauas, P. J. D. 2000, ApJ, 539, 858
Mauas, P. J. D., & Falchi, A. 1994, A&A, 281, 129
Mayor, M., Pepe, F., Queloz, D., et al. 2003, The Messenger, 114, 20
Mittag, M., Schmitt, J. H. M. M., & Schröder, K.-P. 2013, A&A, 549, A117
Newton, E. R., Irwin, J., Charbonneau, D., et al. 2017, ApJ, 834, 85
O'Malley-James, J. T., & Kaltenegger, L. 2017, MNRAS, 469, L26
Passegger, V. M., Reiners, A., Jeffers, S. V., et al. 2018, A&A, 615, A6
Pecaut, M. J., & Mamajek, E. E. 2013, ApJS, 208, 9
Quirrenbach, A., Amado, P. J., Ribas, I., et al. 2018, SPIE Conf. Ser., 10702, 107020W
Reid, I. N., Hawley, S. L., & Gizis, J. E. 1995, AJ, 110, 1838
Reiners, A., Ribas, I., Zechmeister, M., et al. 2017, VizieR Online Data Catalog: 360
Reiners, A., Zechmeister, M., Caballero, J. A., et al. 2018, A&A, 612, A49
Riaz, B., Gizis, J. E., & Harvin, J. 2006, AJ, 132, 866
Ribas, I., Tuomi, M., Reiners, A., et al. 2018, Nature, 563, 365
Robertson, P., Bender, C., Mahadevan, S., Roy, A., & Ramsey, L. W. 2016, ApJ, 832, 112
Scholz, R.-D., Meusinger, H., & Jahreiß, H. 2005, A&A, 442, 211
Schrijver, C. J. 1987, A&A, 172, 111
Schrijver, C. J., Dobson, A. K., & Radick, R. R. 1989, ApJ, 341, 1035
Segura, A., Walkowicz, L. M., Meadows, V., Kasting, J., & Hawley, S. 2010, Astrobiology, 10, 751
Short, C. I., & Doyle, J. G. 1997, A&A, 326, 287
Short, C. I., & Doyle, J. G. 1998, A&A, 336, 613
Short, C. I., & Hauschildt, P. H. 2003, ApJ, 596, 501
Uitenbroek, H., & Criscuoli, S. 2011, ApJ, 736, 69
Vernazza, J. E., Avrett, E. H., & Loeser, R. 1981, ApJS, 45, 635
Wedemeyer, S., Freytag, B., Steffen, M., Ludwig, H.-G., & Holweger, H. 2004, A&A, 414, 1121
Zechmeister, M., Reiners, A., Amado, P. J., et al. 2018, A&A, 609, A12

Appendix A: Best single-component fits and best linear-combination fits

Table A.1. Best single-component fits for the considered stars.

Stars	Model	χ^2_m
Wolf 1056	#047	2.75
GJ 47	#047	2.53
BD+70 68	#080	2.26
GJ 70	#079	2.29
G 244-047	#042	3.45
VX Ari	#079	3.61
Ross 567	#042	2.75
GJ 226	#047	1.8
GJ 258	#047	3.83
GJ 1097	#042	4.04
GJ 3452	#042	2.37
G 234-057*	#136	10.17
GJ 357	#042	2.63
GJ 360*	#136	10.12
GJ 386	#047	2.78
LP 670-017	#080	4.51
GJ 399	#079	2.54
Ross 104	#079	2.59
LP 733-099*	#131	28.11
Ross 905	#042	2.84
GJ 443	#080	2.04
Ross 690	#079	2.41
Ross 695	#042	2.91
Ross 992	#079	2.85
θ Boo B	#047	2.55
Ross 1047	#047	3.16
LP 743-031	#080	3.38
G 137-084	#080	2.66
EW Dra	#080	2.31
GJ 625	#042	2.41
GJ 1203	#047	2.5
LP 446-006	#047	2.82
Ross 863	#079	3.11
GJ 2128	#042	2.45
GJ 671	#042	3.3
G 204-039	#080	2.79
TYC 3529-1437-1*	#131	18.2
Ross 145	#042	3.28
G 155-042	#042	3.54
Ross 730	#029	2.82
HD 349726	#029	2.83
GJ 793	#080	3.01
Wolf 896	#047	2.59
Wolf 906	#079	2.43
LSPM J2116+0234	#079	3.08
Wolf 926	#047	2.99
BD-05 5715	#080	2.9
Wolf 1014	#042	3.32
G 273-093	#047	1.97
Wolf 1051	#080	2.31

Notes. Asterisks identify active stars in the stellar sample. Figure 6 illustrates the temperature structure of all the best single-component fits. The spectra of the best-fit models for GJ 671 and EW Dra are shown in Fig. 10, and those for GJ 360 and TYC 3529-1437-1 are shown in Fig. 11.

Table A.2. Best-fit models in a linear-combination fit with filling factors and the difference $\Delta I_{\mathrm{Ca\,IRT}}$ of the models.

Stars	Inactive model		More active model		χ^2_m	$\Delta I_{\mathrm{Ca\,IRT}}$
	Model	Filling factor	Model	Filling factor		(Å)
Wolf 1056	#047	0.8	#050	0.2	1.02	0.047
GJ 47	#047	0.81	#050	0.19	0.86	0.047
BD+70 68	#047	0.4	#080	0.6	1.18	0.033
GJ 70	#079	0.72	#049	0.28	1.18	0.067
G 244-047	#042	0.66	#049	0.34	1.08	0.071
VX Ari	#079	0.66	#049	0.34	2.04	0.067
Ross 567	#042	0.73	#049	0.27	1.25	0.071
GJ 226	#047	0.92	#064	0.08	0.66	0.189
GJ 258	#047	0.87	#064	0.13	1.08	0.189
GJ 1097	#042	0.63	#049	0.37	1.29	0.071
GJ 3452	#042	0.76	#049	0.24	1.22	0.071
G 234-057★	#080	0.9	#139	0.1	3.58	0.389
GJ 357	#042	0.74	#049	0.26	1.24	0.071
GJ 360★	#080	0.82	#132	0.17	5.13	0.215
GJ 386	#047	0.81	#050	0.19	1.21	0.047
LP 670-017	#042	0.49	#080	0.51	2.23	0.039
GJ 399	#079	0.8	#065	0.2	1.31	0.093
Ross 104	#079	0.71	#049	0.29	1.46	0.067
LP 733-099★	#079	0.68	#149	0.32	16.13	0.598
Ross 905	#042	0.7	#049	0.3	1.05	0.071
GJ 443	#047	0.37	#080	0.63	1.09	0.033
Ross 690	#079	0.82	#065	0.18	1.39	0.093
Ross 695	#042	0.73	#049	0.27	1.41	0.071
Ross 992	#079	0.68	#049	0.32	1.43	0.067
θ Boo B	#047	0.8	#050	0.2	0.83	0.047
Ross 1047	#047	0.88	#064	0.12	1.01	0.189
LP 743-031	#047	0.43	#080	0.57	2.12	0.033
G 137-084	#029	0.39	#080	0.61	1.39	0.038
EW Dra	#047	0.44	#080	0.56	0.96	0.033
GJ 625	#042	0.74	#049	0.26	1.02	0.071
GJ 1203	#047	0.81	#050	0.19	0.98	0.047
LP 446-006	#047	0.8	#050	0.2	1.08	0.047
Ross 863	#079	0.8	#060	0.2	1.87	0.102
GJ 2128	#042	0.75	#049	0.25	1.13	0.071
GJ 671	#042	0.7	#049	0.3	1.44	0.071
G 204-039	#029	0.36	#080	0.64	1.73	0.038
TYC 3529-1437-1★	#079	0.75	#149	0.25	14.25	0.598
Ross 145	#042	0.69	#049	0.31	1.27	0.071
G 155-042	#042	0.68	#049	0.32	1.44	0.071
Ross 730	#029	0.8	#049	0.2	1.89	0.070
HD 349726	#029	0.8	#049	0.2	1.91	0.070
GJ 793	#112	0.22	#080	0.78	1.93	0.050
Wolf 896	#047	0.89	#064	0.11	0.67	0.189
Wolf 906	#079	0.79	#065	0.21	1.09	0.093
LSPM J2116+0234	#079	0.78	#060	0.22	1.54	0.102
Wolf 926	#047	0.79	#050	0.21	1.05	0.047
BD-05 5715	#047	0.43	#080	0.57	1.66	0.033
Wolf 1014	#042	0.7	#049	0.3	1.43	0.071
G 273-093	#047	0.85	#050	0.15	0.92	0.047
Wolf 1051	#042	0.32	#080	0.68	1.44	0.039

Notes. The line of Na I D_2 and the bluest Ca II IRT line are weighted by a factor of 12 compared to Hα as described in Sect. 4.1. Asterisks identify active stars in the stellar sample. The combinations for GJ 360 and TYC 3529-1437-1 are illustrated in Fig. 12.

Appendix B: Linear regressions of the filling factors as a function of activity state

Table B.1. Gradients $b \pm \sigma_b$ and intercepts $a \pm \sigma_a$ of the linear regressions of the filling factors of the inactive region as a function of $I_{\mathrm{Ca\,IRT}}$ (Eq. (5)).

Stars	$b\,(\mathrm{Å}^{-1})$	a
Wolf 1056	1.33 ± 19.94	0.79 ± 0.0128
BD+70 68	35.28 ± 3.60	0.42 ± 0.0060
G 244-047	9.66 ± 6.31	0.63 ± 0.0056
Ross 567	5.01 ± 2.13	0.71 ± 0.0033
GJ 258	2.27 ± 2.60	0.87 ± 0.0034
GJ 1097	10.96 ± 11.49	0.61 ± 0.0169
G 234-057★	2.44 ± 239.72	0.89 ± 0.4470
GJ 360★	5.59 ± 0.28	0.83 ± 0.0015
Ross 104	5.86 ± 2.31	0.72 ± 0.0017
LP 733-099★	1.78 ± 0.98	0.68 ± 0.0092
Ross 905	11.25 ± 4.82	0.69 ± 0.0019
Ross 690	4.13 ± 0.96	0.81 ± 0.0012
Ross 992	4.77 ± 3.19	0.69 ± 0.0056
Ross 1047	7.95 ± 1.35	0.87 ± 0.0036
LP 743-031	10.80 ± 7.01	0.41 ± 0.0143
G 137-084	31.95 ± 4.38	0.39 ± 0.0053
EW Dra	38.59 ± 2.54	0.42 ± 0.0060
GJ 625	10.03 ± 2.93	0.73 ± 0.0034
LP 446-006	2.67 ± 7.99	0.81 ± 0.0107
Ross 863	5.51 ± 4.24	0.80 ± 0.0063
GJ 2128	17.22 ± 4.75	0.73 ± 0.0052
GJ 671	14.65 ± 3.31	0.68 ± 0.0028
G 204-039	29.84 ± 6.28	0.29 ± 0.0097
TYC 3529-1437-1★	2.23 ± 0.11	0.75 ± 0.0011
Ross 145	12.94 ± 2.05	0.67 ± 0.0052
Ross 730	−5.76 ± 10.77	0.80 ± 0.0055
HD 349726	0.31 ± 7.66	0.78 ± 0.0048
GJ 793	−13.19 ± 5.83	0.20 ± 0.0100
Wolf 896	6.37 ± 0.69	0.88 ± 0.0024
LSPM J2116+0234	7.07 ± 1.06	0.78 ± 0.0011
Wolf 926	13.78 ± 2.52	0.77 ± 0.0042
BD-05 5715	19.60 ± 6.67	0.44 ± 0.0080
Wolf 1014	−1.07 ± 2.63	0.69 ± 0.0030

Notes. Asterisks identify active stars in the stellar sample.

Appendix C: Calculated model set

Table C.1. Calculated model set and parameters.

Model	$m_{\rm min}$ (dex)	$m_{\rm mid}$ (dex)	$T_{\rm mid}$ (K)	$m_{\rm top}$ (dex)	$T_{\rm top}$ (K)	grad$_{\rm TR}$ (dex)	$I_{\rm Ca\,IRT}$ (Å)
#001	−4.0	−4.3	5500	−6.0	6000	7.5	0.653
#002	−3.5	−3.6	4500	−5.2	5000	7.5	0.655
#003	−3.5	−3.6	4500	−5.2	5000	8.0	0.654
#004	−3.5	−3.6	4500	−5.1	5000	7.5	0.655
#005	−3.5	−3.8	5500	−5.5	6000	7.5	0.655
#006	−3.4	−3.6	4500	−5.1	5000	7.5	0.654
#007	−3.2	−3.6	4500	−5.1	5000	7.5	0.653
#008	−3.2	−3.6	4500	−5.0	5000	7.5	0.654
#009	−3.2	−3.6	5500	−5.1	6000	7.5	0.655
#010	−3.2	−3.5	4500	−5.0	5000	7.5	0.654
#011	−3.2	−3.5	4700	−5.0	5200	7.5	0.654
#012	−3.1	−3.6	4500	−5.0	5000	8.5	0.652
#013	−3.1	−3.3	4500	−5.0	5000	8.5	0.653
#014	−3.1	−3.3	5500	−5.0	6000	8.5	0.654
#015	−3.0	−3.6	4500	−5.0	5000	7.5	0.653
#016	−3.0	−3.6	5500	−5.0	6000	7.5	0.652
#017	−3.0	−3.4	4500	−4.9	5000	7.5	0.653
#018	−3.0	−3.3	4500	−5.0	5000	7.5	0.653
#019	−3.0	−3.3	4500	−5.0	5000	7.5	0.653
#020	−3.0	−3.3	5500	−5.0	6000	7.5	0.653
#021	−3.0	−3.3	5500	−5.0	6000	7.5	0.653
#022	−2.8	−3.6	4500	−5.0	5000	7.5	0.576
#023	−2.8	−3.6	5500	−5.0	6000	7.5	0.651
#024	−2.8	−3.3	4500	−5.0	5000	7.5	0.653
#025	−2.8	−3.3	5500	−5.0	6000	7.5	0.651
#026	−2.6	−3.6	4500	−5.0	5000	8.5	0.650
#027	−2.6	−3.2	4500	−4.5	5000	8.5	0.652
#028	−2.6	−3.2	4500	−4.5	6000	8.5	0.650
#029	−2.6	−3.2	4500	−4.5	7000	8.5	0.649
#030	−2.6	−3.0	4500	−4.5	5000	8.5	0.652
#031	−2.6	−3.0	4500	−4.5	6000	8.5	0.651
#032	−2.6	−3.0	4500	−4.5	7000	8.5	0.651
#033	−2.6	−2.8	3500	−4.5	5000	8.5	0.653
#034	−2.6	−2.8	4000	−4.5	4500	8.5	0.652
#035	−2.6	−2.8	4500	−4.5	5000	8.0	0.653
#036	−2.6	−2.8	4500	−4.5	5000	8.5	0.653
#037	−2.6	−2.8	4500	−4.5	6000	8.5	0.652
#038	−2.6	−2.8	4500	−4.5	7000	8.5	0.652
#039	−2.5	−3.6	4500	−5.0	5000	7.5	0.652
#040	−2.5	−3.6	5500	−5.0	6000	7.5	0.650
#041	−2.5	−3.6	5500	−5.0	6200	7.5	0.650
#042	−2.5	−3.6	5500	−5.0	6500	7.5	0.650
#043	−2.5	−3.3	4500	−5.0	5000	7.5	0.652
#044	−2.5	−3.3	5500	−5.0	6000	7.5	0.651
#045	−2.5	−2.8	4500	−4.5	5000	7.5	0.654
#046	−2.5	−2.8	5500	−4.5	6000	7.5	0.649
#047	−2.5	−2.7	6500	−5.0	7000	9.2	0.644
#048	−2.1	−2.6	4500	−4.0	5000	8.5	0.658
#049	−2.1	−2.6	6500	−4.5	7000	7.5	0.579
#050	−2.1	−2.6	6500	−4.0	7000	9.2	0.597
#051	−2.1	−2.3	4500	−4.0	5000	8.5	0.664
#052	−2.1	−2.3	5000	−5.0	5500	7.5	0.667
#053	−2.1	−2.3	5000	−4.0	6000	8.5	0.648
#054	−2.1	−2.3	5000	−4.0	6000	9.0	0.660
#055	−2.1	−2.3	5000	−4.0	6000	9.5	0.665
#056	−2.1	−2.3	5500	−5.0	6000	7.5	0.660
#057	−2.1	−2.3	5500	−4.5	6000	7.5	0.632

Table C.1. continued.

Model	$m_{\rm min}$ (dex)	$m_{\rm mid}$ (dex)	$T_{\rm mid}$ (K)	$m_{\rm top}$ (dex)	$T_{\rm top}$ (K)	$\mathrm{grad}_{\rm TR}$ (dex)	$I_{\rm Ca\,IRT}$ (Å)
#058	−2.1	−2.3	5500	−4.0	6000	8.5	0.628
#059	−2.1	−2.3	5500	−4.0	6000	9.5	0.649
#060	−2.1	−2.3	6500	−5.0	7000	9.2	0.543
#061	−2.1	−2.3	6500	−4.5	7000	9.2	0.524
#062	−2.1	−2.3	6500	−4.2	7000	8.2	0.427
#063	−2.1	−2.3	6500	−4.0	7000	9.0	0.442
#064	−2.1	−2.3	6500	−4.0	7000	9.2	0.455
#065	−2.0	−2.5	6500	−5.0	8000	9.2	0.552
#066	−2.0	−2.5	6500	−4.5	8000	9.2	0.510
#067	−2.0	−2.3	5000	−4.0	7000	8.2	0.605
#068	−2.0	−2.3	6500	−5.0	7000	9.2	0.539
#069	−2.0	−2.3	6500	−4.5	7000	9.2	0.521
#070	−2.0	−2.3	6500	−4.0	7000	9.2	0.455
#071	−2.0	−2.2	6500	−5.0	7000	9.2	0.539
#072	−2.0	−2.2	6500	−4.5	7000	9.2	0.521
#073	−1.9	−2.3	6500	−4.0	7000	9.2	0.428
#074	−1.8	−2.6	3000	−4.0	7000	9.0	0.653
#075	−1.8	−2.6	3500	−4.0	7000	9.0	0.656
#076	−1.8	−2.3	3000	−4.0	7000	9.0	0.656
#077	−1.8	−2.3	3500	−4.0	7000	9.0	0.658
#078	−1.8	−2.3	6500	−4.0	7000	9.0	0.363
#079	−1.5	−2.5	5000	−4.0	7500	8.5	0.645
#080	−1.5	−2.5	5500	−4.0	7500	8.5	0.611
#081	−1.5	−2.5	6000	−4.1	7500	8.5	0.538
#082	−1.5	−2.5	6000	−4.0	7500	8.0	0.439
#083	−1.5	−2.5	6000	−4.0	7500	8.5	0.527
#084	−1.5	−2.5	6000	−4.0	8000	8.0	0.312
#085	−1.5	−2.5	6000	−3.9	7500	8.5	0.455
#086	−1.5	−2.5	6000	−3.8	7500	8.5	0.424
#087	−1.5	−2.5	6000	−3.7	6500	8.5	0.416
#088	−1.5	−2.5	6000	−3.7	7000	8.5	0.391
#089	−1.5	−2.5	6000	−3.7	7500	8.5	0.270
#090	−1.5	−2.5	6500	−4.0	7500	8.0	0.111
#091	−1.5	−2.5	6500	−3.5	7500	8.5	−0.326
#092	−1.5	−2.3	4000	−4.0	7000	9.0	0.665
#093	−1.5	−2.3	5000	−4.0	7000	8.2	0.604
#094	−1.5	−2.3	5000	−4.0	7000	9.0	0.650
#095	−1.5	−2.3	6500	−4.5	7000	9.0	0.408
#096	−1.5	−2.3	6500	−4.5	8000	9.2	0.089
#097	−1.5	−2.3	6500	−4.0	7000	9.0	0.302
#098	−1.5	−2.0	4500	−3.5	5000	8.5	0.668
#099	−1.5	−2.0	5000	−3.5	5500	8.0	0.584
#100	−1.5	−2.0	5000	−3.5	5500	8.5	0.599
#101	−1.5	−2.0	5000	−3.5	5700	8.5	0.562
#102	−1.5	−2.0	5000	−3.5	5900	8.5	0.510
#103	−1.5	−2.0	5000	−3.5	6000	8.5	0.487
#104	−1.5	−1.7	5500	−4.0	6000	8.0	0.444
#105	−1.5	−1.7	5500	−4.0	6000	8.5	0.537
#106	−1.5	−1.7	6000	−4.0	6500	8.5	0.366
#107	−1.0	−3.5	4000	−5.0	8000	9.5	0.663
#108	−1.0	−3.5	4000	−4.5	8000	9.5	0.666
#109	−1.0	−3.0	4000	−5.0	8000	9.5	0.659
#110	−1.0	−3.0	4000	−4.5	8000	9.5	0.662
#111	−1.0	−3.0	4000	−4.0	8000	9.5	0.672
#112	−1.0	−2.7	4000	−3.5	7000	9.5	0.661
#113	−1.0	−2.7	4000	−3.5	7500	9.5	0.650
#114	−1.0	−2.7	4000	−3.5	8000	9.5	0.607
#115	−1.0	−2.7	4000	−3.5	8100	9.5	0.580
#116	−1.0	−2.7	4000	−3.5	8200	9.5	0.539

Table C.1. continued.

Model	$m_{\rm min}$ (dex)	$m_{\rm mid}$ (dex)	$T_{\rm mid}$ (K)	$m_{\rm top}$ (dex)	$T_{\rm top}$ (K)	grad$_{\rm TR}$ (dex)	$I_{\rm Ca\,IRT}$ (Å)
#117	−1.0	−2.7	4000	−3.5	8250	9.5	0.514
#118	−1.0	−2.7	4200	−3.5	8200	9.5	0.516
#119	−1.0	−2.7	4200	−3.5	8250	9.5	0.484
#120	−1.0	−2.7	4500	−3.5	8300	8.5	0.256
#121	−1.0	−2.7	4600	−3.6	7800	8.5	0.468
#122	−1.0	−2.6	5000	−3.6	7800	8.5	0.411
#123	−1.0	−2.6	5000	−3.6	7800	9.5	0.599
#124	−1.0	−2.5	4000	−4.0	8000	9.5	0.671
#125	−1.0	−2.5	4300	−3.5	8250	8.5	0.190
#126	−1.0	−2.5	4600	−3.6	7800	8.5	0.380
#127	−1.0	−2.5	5200	−3.8	8000	8.5	0.503
#128	−1.0	−2.5	5200	−3.8	8200	8.5	0.425
#129	−1.0	−2.5	5200	−3.7	8000	8.5	0.345
#130	−1.0	−2.5	5200	−3.7	8000	8.8	0.424
#131	−1.0	−2.5	5200	−3.7	8000	9.5	0.534
#132	−1.0	−2.5	5200	−3.6	8000	9.6	0.396
#133	−1.0	−2.5	5200	−3.5	8000	9.5	0.324
#134	−1.0	−2.5	5500	−3.5	8000	9.5	0.194
#135	−1.0	−2.3	4550	−3.5	8000	8.5	0.155
#136	−1.0	−2.3	4600	−3.8	7800	8.5	0.572
#137	−1.0	−2.3	4600	−3.7	7800	8.5	0.452
#138	−1.0	−2.3	4600	−3.6	7800	8.5	0.286
#139	−1.0	−2.3	4600	−3.5	7800	8.5	0.222
#140	−1.0	−2.3	4600	−3.5	7800	10.0	0.529
#141	−1.0	−2.3	4800	−3.6	7800	8.5	0.240
#142	−1.0	−2.3	5000	−3.7	7800	8.5	0.372
#143	−1.0	−2.3	5000	−3.7	8000	8.5	0.285
#144	−1.0	−2.3	5000	−3.6	7800	8.5	0.184
#145	−1.0	−2.3	5000	−3.6	8000	8.5	0.073
#146	−1.0	−2.3	5000	−3.5	7800	8.5	0.115
#147	−1.0	−2.3	5000	−3.5	7900	8.5	0.060
#148	−1.0	−2.3	5500	−3.5	8000	9.8	0.030
#149	−1.0	−2.3	5500	−3.5	8000	10.0	0.047
#150	−1.0	−2.3	6000	−3.5	8000	10.0	−0.381
#151	−1.0	−2.2	5500	−3.6	8000	9.5	0.063
#152	−1.0	−2.0	4000	−4.0	8000	9.5	0.661
#153	−1.0	−2.0	4600	−3.6	7800	8.5	0.193
#154	−1.0	−2.0	5200	−3.5	8000	9.5	−0.021
#155	−1.0	−1.5	4000	−4.0	8000	9.5	0.576
#156	−1.0	−1.5	5000	−3.5	6000	8.5	0.332
#157	−0.5	−2.7	4200	−3.5	8200	9.5	0.515
#158	−0.5	−2.7	4200	−3.5	8250	9.5	0.483
#159	−0.3	−3.0	4000	−4.5	8000	9.5	0.675
#160	−0.3	−2.8	4000	−3.5	7000	9.5	0.674
#161	−0.3	−2.8	4000	−3.5	8000	9.5	0.640
#162	−0.3	−2.7	4000	−3.5	8000	9.5	0.606
#163	−0.3	−1.5	7000	−3.5	7800	8.5	−0.758
#164	−0.3	−1.5	7000	−3.5	8000	8.5	−0.816
#165	−0.3	−1.5	8000	−3.5	8500	9.5	0.234
#166	−0.3	−1.5	8000	−4.0	8500	9.5	0.227

Chapter 3

The He I infrared triplet lines in PHOENIX models of M2–3 V stars

In the following, this chapter reproduces the publication "*The* He I *infrared triplet lines in PHOENIX models of M2–3 V stars*" (Hintz et al. 2020). It describes the behavior of the He I IR line in PHOENIX chromosphere models of M2–3 V stars for different states of activity. The line behavior is studied with respect to the EUV radiation. The connection of the line strengths to the EUV radiation gives an indicator for the contributions of the responsible line formation mechanisms. The PHOENIX model calculations for this publication were conducted by myself as the main author with the help and advice by Birgit Fuhrmeister and Andreas Schweitzer. Analyzing the data and writing the paper were done by myself. However, Sect. 3.2 in the paper, that is, the comparison of results from CARMENES observations covering the whole M-dwarf range performed by Fuhrmeister et al. (2019) to the model results, was mainly written by Birgit Fuhrmeister. Furthermore, important ideas for the paper were given by Birgit Fuhrmeister, Stefan Czesla, Jürgen H. M. M. Schmitt, and Andreas Schweitzer. The other co-authors helped with data acquisition and proofreading. The paper Hintz et al. (2020) has been accepted for publication in Astronomy & Astrophysics on April 28th, 2020.

Astronomy & Astrophysics manuscript no. 37596_corr
May 12, 2020

The CARMENES search for exoplanets around M dwarfs

The He I infrared triplet lines in PHOENIX models of M2–3 V stars

D. Hintz[1], B. Fuhrmeister[1], S. Czesla[1], J. H. M. M. Schmitt[1], A. Schweitzer[1], E. Nagel[2], E. N. Johnson[3], J. A. Caballero[4], M. Zechmeister[3], S. V. Jeffers[3], A. Reiners[3], I. Ribas[5,6], P. J. Amado[7], A. Quirrenbach[8], G. Anglada-Escudé[7,9], F. F. Bauer[7], V. J. S. Béjar[10,11], M. Cortés-Contreras[4], S. Dreizler[3], D. Galadí-Enríquez[12], E. W. Guenther[2,10], P. H. Hauschildt[1], A. Kaminski[8], M. Kürster[13], M. Lafarga[5,6], M. López del Fresno[4], D. Montes[14], and J. C. Morales[5,6]

[1] Hamburger Sternwarte, University of Hamburg, Gojenbergsweg 112, D-21029 Hamburg, Germany
e-mail: dominik.hintz@hs.uni-hamburg.de
[2] Thüringer Landessternwarte Tautenburg, Sternwarte 5, D-07778 Tautenburg, Germany
[3] Institut für Astrophysik, Friedrich-Hund-Platz 1, D-37077 Göttingen, Germany
[4] Centro de Astrobiología (CSIC-INTA), ESAC, Camino Bajo del Castillo s/n, E-28692 Villanueva de la Cañada, Madrid, Spain
[5] Institut de Ciències de l'Espai (ICE, CSIC), Campus UAB, c/ de Can Magrans s/n, E-08193 Bellaterra, Barcelona, Spain
[6] Institut d'Estudis Espacials de Catalunya (IEEC), E-08034 Barcelona, Spain
[7] Instituto de Astrofísica de Andalucía (CSIC), Glorieta de la Astronomía s/n, E-18008 Granada, Spain
[8] Landessternwarte, Zentrum für Astronomie der Universität Heidelberg, Königstuhl 12, D-69117 Heidelberg, Germany
[9] School of Physics and Astronomy, Queen Mary, University of London, 327 Mile End Road, London, E1 4NS, UK
[10] Instituto de Astrofísica de Canarias, c/ Vía Láctea s/n, E-38205 La Laguna, Tenerife, Spain
[11] Departamento de Astrofísica, Universidad de La Laguna, E-38206 Tenerife, Spain
[12] Centro Astronómico Hispano-Alemán (MPG-CSIC), Observatorio Astronómico de Calar Alto, Sierra de los Filabres, E-04550 Gérgal, Almería, Spain
[13] Max-Planck-Institut für Astronomie, Königstuhl 17, D-69117 Heidelberg, Germany
[14] Departamento de Física de la Tierra y Astrofísica and UPARCOS-UCM (Unidad de Física de Partículas y del Cosmos de la UCM), Facultad de Ciencias Físicas, Universidad Complutense de Madrid, E-28040, Madrid, Spain

Received 28 January 2020 / accepted dd mm 2020

ABSTRACT

The He I infrared (IR) line at a vacuum wavelength of 10 833 Å is a diagnostic for the investigation of atmospheres of stars and planets orbiting them. For the first time, we study the behavior of the He I IR line in a set of chromospheric models for M-dwarf stars, whose much denser chromospheres may favor collisions for the level population over photoionization and recombination, which are believed to be dominant in solar-type stars. For this purpose, we use published PHOENIX models for stars of spectral types M2 V and M3 V and also compute new series of models with different levels of activity following an ansatz developed for the case of the Sun. We perform a detailed analysis of the behavior of the He I IR line within these models. We evaluate the line in relation to other chromospheric lines and also the influence of the extreme ultraviolet (EUV) radiation field. The analysis of the He I IR line strengths as a function of the respective EUV radiation field strengths suggests that the mechanism of photoionization and recombination is necessary to form the line for inactive models, while collisions start to play a role in our most active models. Moreover, the published model set, which is optimized in the ranges of the Na I D_2, Hα, and the bluest Ca II IR triplet line, gives an adequate prediction of the He I IR line for most stars of the stellar sample. Because especially the most inactive stars with weak He I IR lines are fit worst by our models, it seems that our assumption of a 100% filling factor of a single inactive component no longer holds for these stars.

Key words. stars: activity – stars: chromospheres – stars: late-type

1. Introduction

Spectral lines arising in a stellar chromosphere provide essential information on stellar activity. In the optical wavelength range, widely used chromospheric indicator lines include the Ca II H and K lines (3934.77 Å, 3969.59 Å), the He I D_3 line (5877.25 Å), the Na I D doublet (5897.56 Å, 5891.58 Å), and the Hα (6564.62 Å) line. In the infrared, the Ca II infrared triplet (IRT) lines (8500.35 Å, 8544.44 Å, 8664.52 Å) and the He I IRT lines (hereafter He I IR line for short) at 10 833 Å are widely used chromospheric diagnostics.[1] Specifically, the He I IR line has recently become even more important in the light of investigations of exoplanet atmospheres around late-type stars (e.g., Spake et al. 2018; Nortmann et al. 2018; Salz et al. 2018). For this reason, it is imperative to improve our understanding of the He I IR line behavior of stars, especially for the very late-type stars. In this paper, we investigate the behavior of the He I IR line in early M-dwarf stars.

[1] We use vacuum wavelengths throughout the paper. However, the He I IR line is well known for its air wavelength at 10 830 Å.

The He I IR line is a triplet line of orthohelium, whose three components are centered at 10 832.057, 10 833.217, and 10 833.306 Å. The term scheme of the neutral helium atom splits into the ortho- and parahelium branch, depending on whether the electrons have aligned or opposite spins. Singlet lines only occur in parahelium, while orthohelium is characterized by triplet lines.

The lower level of the He I IR line is the metastable $2\,^3S$ level of orthohelium, which is located about 20 eV above the ground state of (para-)helium. The He I IR line appears in absorption when the occupation number of the metastable level is higher than that of the overlying $2\,^3P$ triplet levels, and vice versa for an emission line. A decisive question is which process is responsible for populating the metastable ground state. Previous studies modeling the He I IR line (e.g., Andretta & Giampapa 1995; Andretta & Jones 1997) investigated two possible line formation mechanisms in detail: (i) the photoionization and recombination (PR) mechanism, and (ii) collisional excitation.

In the PR formation scenario, the continuum shortward of 504 Å is important for photoionization of He I in the ground state. The photons from this continuum, produced in the transition region and corona, photoionize the He I atoms and produce free electrons. These can be captured by the helium ion into a highly excited energy level, from which they finally cascade down to the metastable $2\,^3S$ level. The excited He I atom then interacts with photospheric photons. The PR mechanism is thought to dominate the population of the metastable level at temperatures below 10 000 K in the upper chromosphere. In the collisional line formation scenario, a helium atom in the ground state is excited by an electron collision to the $2\,^3S$ level. This process requires a sufficiently dense high-energy electron population, which is typically only encountered in the hot upper chromosphere and lower transition region at temperatures above 20 000 K.

Vaughan & Zirin (1968) were the first to study the He I IR line in stars of spectral type between F and M. In their study, He I IR absorption was detected for most of the G and early K-type stars in their sample. Further observations by Zirin (1975a) revealed He I IR emission lines for some late M-type stars. Zirin (1975b) constructed a solar model incorporating the PR mechanism and concluded that this mechanism is decisive for the formation of the He I D_3 and He I IR lines. Furthermore, they postulated a correlation between the He I IR line equivalent widths and the soft X-ray flux for stars that show the line in absorption. This was later observed by Zarro & Zirin (1986) for stars in the spectral range between F7 and K3.

In a study of the formation of the He I IR line in the Sun, Avrett et al. (1994) generated different solar models based on the VAL C model by Vernazza et al. (1981) for the average quiet Sun. In varying the atmospheric height of the transition region onset as well as changing the incident radiation from the transition region, Avrett et al. (1994) found that enhancing the radiation leads to an increase in absorption of the solar He I IR line. In contrast, a solar plage model, characterized by a radiation level thrice that of the quiet Sun and a transition region moved inward, showed a slightly weaker He I IR line than the average quiet model. The authors attributed the weakening of the line strength in the plage model to its high density and to the relatively lower geometric extension of the chromosphere in this model. Andretta & Giampapa (1995) found a clear correlation between the X-ray emission and the neutral helium lines in chromospheric models of F, G, and early K stars by investigating the behavior of the He I D_3 and He I IR line with the VAL C model shifted in density. Intensifying the ionizing radiation field leads to stronger He I IR line absorption until a limit of ~400 mÅ in the equivalent width is reached. Then the behavior reverses and the line tends to go into emission. Studying the He I IR line of stars of spectral types G, K, and M, Sanz-Forcada & Dupree (2008) concluded that the collisional excitation mechanism may contribute to the line formation for active dwarfs because high densities of neutral helium in the upper chromosphere can be reached. This conclusion agrees with the results of Andretta & Giampapa (1995).

Andretta & Jones (1997) theoretically studied the effects of these two He I IR line formation mechanisms on the solar spectrum. From computing a series of solar models that varied in density and radiation field, they found that the formation mechanisms influence the He I IR line quite differently. While the He I IR line is highly sensitive to irradiation from the transition region and corona in the classical VAL C model for the quiet Sun, collisions become more important when the chromospheric structure is shifted inward toward increasing densities. After an inward shift of ten times the mass load above the quiet-Sun model, the line becomes almost insensitive to the radiation field. Further shifting toward higher densities drives the line into emission. Later, Leenaarts et al. (2016) investigated the spatial structure of the He I IR line using a three-dimensional radiation-magnetohydrodynamic simulation. From their model atmosphere, which included the solar chromosphere and corona, they were able to confirm that the PR mechanism is responsible for populating the $2\,^3S$ level in the case of the Sun. Compared to this, the collisional excitation appeared to be negligible. However, they also found that variations of the chromospheric electron density have a crucial effect on variations of the He I IR line.

The number of He I IR line studies in M dwarfs falls far short of that carried out for solar-type stars. A recent observational study by Fuhrmeister et al. (2019) used high-resolution infrared spectra obtained with the Calar Alto high-Resolution search for M dwarfs with Exo-earths with Near-infrared and optical Echelle Spectrographs (CARMENES; Quirrenbach et al. 2018) to examine the behavior of the He I IR line in M dwarfs. They found the line to be prominent in early M dwarfs with a tendency to decrease in strength toward later spectral types. Moreover, the line was observed transiently in emission during flaring events. Fuhrmeister et al. (2019) was unable to detect a correlation of the line strength measured by its pseudo-equivalent width (pEW) and the fractional X-ray luminosity (L_X/L_{bol}) even for the earliest M dwarfs. It remains unclear whether this noncorrelation is caused by observational deficits (e.g., the lack of simultaneous observations) or a stronger effect of the collisional level population mechanism. Hintz et al. (2019) compared models of optical chromospheric lines with observed spectra of a stellar sample of M2–3 V stars. In the best-fit models, the onset of the transition region can reach column mass densities more than one magnitude higher than the density of the solar VAL C model even in the low-activity regime, implying much higher electron densities than in the Sun. Even in early M dwarfs, collisions may therefore play a larger role in the He I IR line formation. For this reason, chromospheric models dedicated to M dwarfs need to be computed to theoretically explain the observed behavior.

In this study, we investigate the behavior of the He I IR line using a model set of chromospheres based on the model set presented by Hintz et al. (2019). We introduce the model set as well as the comparison observations, and describe the method of measuring the equivalent widths in Sect. 2. In Sect. 3 we show and discuss our results, and we present our conclusions in Sect. 4.

2. Models and observations

2.1. Observations and stellar sample

The observed spectra to which we compared our models were taken with the CARMENES spectrograph (Quirrenbach et al. 2018) and retrieved from the CARMENES archive; the CARMENES spectrograph covers the He I IR line in its near-infrared channel (NIR), which ranges from 9600 to 17 100 Å with a resolution of $R = 80\,400$. All spectra were reduced by the CARMENES data reduction pipeline (Caballero et al. 2016; Zechmeister et al. 2018).

For further correction and averaging of the spectra, we followed the same procedures as Fuhrmeister et al. (2019): The stellar spectra were corrected for telluric contamination using the method of Nagel (2019) and for airglow lines by coadding the spectra using the SpEctrum Radial Velocity AnaLyser (SERVAL, Zechmeister et al. 2018). Furthermore, barycentric and radial velocity shifts were corrected in the spectra.

We compared the model set to 50 M2–3 V stars, which are a subsample of the stars used by Fuhrmeister et al. (2019). Our sample is defined by the effective temperature range $T_{\rm eff} = 3500 \pm 50$ K, and has previously been investigated by Hintz et al. (2019). It comprises four active stars in which the lines of Na I D$_2$, Hα, and the Ca II IRT lines usually appear in emission; for further details about the stellar parameters of the sample, we refer to Table 1 in Hintz et al. (2019).

2.2. Measuring the He I IR line pseudo-equivalent width

To characterize the line strengths in the investigated spectra, we calculated the pEW with the same ansatz as Fuhrmeister et al. (2019), who fit Voigt profiles to the He I IR line profiles. This line profile fitting has a long tradition. It has also been performed, for example, by Takeda & Takada-Hidai (2011) using Gaussian models to estimate the equivalent width of the He I IR line in late-type stars.

In the following, we give a brief overview of the method and refer to Fuhrmeister et al. (2019) for more details. We used an empirical function consisting of four Voigt profiles to approximate the spectrum in the wavelength range of 10 829–10 835 Å. The Voigt components represent the relevant spectral lines, including the He I IR line. The two red components of the He I IR triplet at 10 833.217 and 10 833.306 Å are unresolved, and, therefore, represented by one Voigt profile centered at 10 833.25 Å, which is used to estimate the pEW. The weak blue triplet component is neglected in the calculations of this pEW because it is blended with an unidentified absorption line. Figure 1 shows the Voigt profile fits of the He I IR line for three model spectra of different states of activity. While the fit of the more or less filled-in line (middle panel) hardly reproduces the shape of the line, clear absorption and emission lines (top and bottom panels, respectively) are well fit by the respective Voigt profiles. Therefore, pEW values close to zero may be problematic.

To determine the pEW of the Hα, He I D$_3$, Na I D$_2$, and the bluest Ca II IRT line, we integrated the model spectrum in the respective wavelength ranges following Fuhrmeister et al. (2019) for the stellar sample. The central wavelengths of the lines, the line widths, and the ranges of the reference bands are adopted from Fuhrmeister et al. (2019).

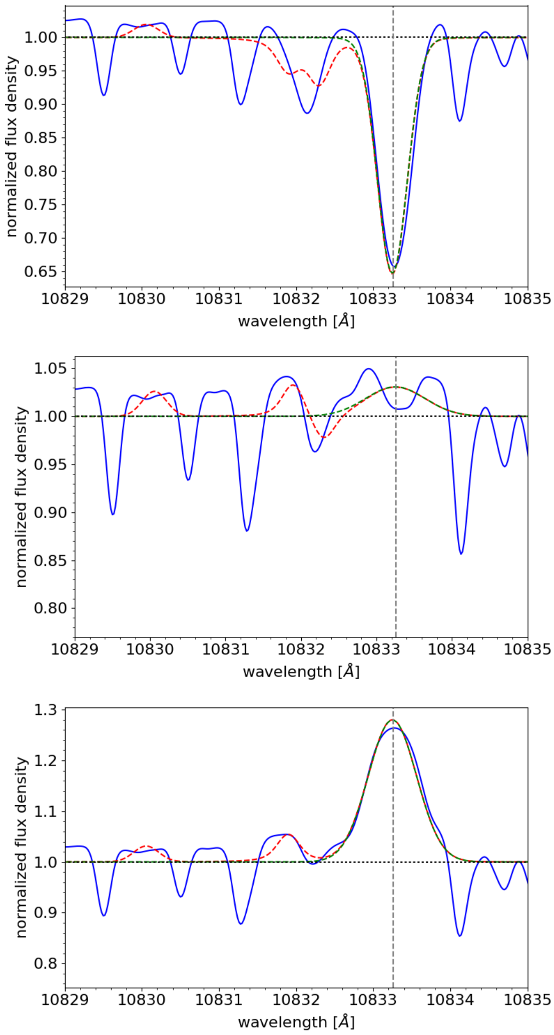

Fig. 1. Fitting Voigt profiles in the wavelength range around the He I IR triplet (10 829–10 835 Å). Three models (solid blue lines) at different states of activity are shown: a model with He I IR in absorption (*top panel*, number 042 from Hintz et al. (2019)) or number A2 from the model series A, details are given in Sect. 2.4), one nearly filled in (*middle panel*, number 149), and one with the line in emission (*bottom panel*, number 121). The red dashed line is the best fit of four Voigt profiles in the wavelength range of 10 829–10 835 Å. The dashed green line represents the single Voigt profile fit to the center of the two indistinguishable red components of the He I IR triplet at 10 833.25 Å (dashed vertical line). The pEW of the He I IR line is calculated from the green Voigt profile.

2.3. Previous chromospheric models

The stellar atmosphere code PHOENIX[2] has been developed for calculations of atmospheres and spectra from various objects such as stars, planets, novae, and supernovae (Hauschildt 1992, 1993; Hauschildt & Baron 1999). A recent library of PHOENIX model photospheres was calculated by Husser et al. (2013) in the effective temperature range of 2 300–12 000 K, covering a wide range of different stellar spectral types. Based on one of these photospheric models, Hintz et al. (2019) computed chromosphere models for M dwarfs using the PHOENIX code, but extending the photospheric PHOENIX model, which was com-

[2] https://www.physik.uni-hamburg.de/en/hs/group-hauschildt/research/phoenix.html

Table 1. Parameters of the extended model series A and B based on models 042 and 080 from Hintz et al. (2019), hereafter A2 and B4 in the new model series, respectively.

Model	$m_{\rm min}^{a}$ [dex]	$m_{\rm mid}^{a}$ [dex]	$T_{\rm mid}^{a}$ [K]	$m_{\rm top}^{a}$ [dex]	$T_{\rm top}^{a}$ [K]	$\nabla_{\rm TR}^{a}$ [dex]	m_i/m_0^{b}
A1	-3.0	-4.1	5500	-5.5	6500	7.5	0.37
A2	-2.5	-3.6	5500	-5.0	6500	7.5	1.0
A3	-2.0	-3.1	5500	-4.5	6500	7.5	3.16
A4	-1.9	-3.0	5500	-4.4	6500	7.5	4.47
B1	-2.5	-3.5	5500	-5.0	7500	8.5	0.1
B2	-2.3	-3.3	5500	-4.8	7500	8.5	0.16
B3	-1.8	-2.8	5500	-4.3	7500	8.5	0.50
B4	-1.5	-2.5	5500	-4.0	7500	8.5	1.0
B5	-1.3	-2.3	5500	-3.8	7500	8.5	1.59
B6	-1.2	-2.2	5500	-3.7	7500	8.5	2.24

[a] The six parameters are consistent with the definitions of Hintz et al. (2019). The column mass density $m_{\rm min}$ represents the onset of the lower chromosphere and also marks the location of the temperature minimum. The end of the lower chromosphere is located at the column mass density $m_{\rm mid}$ and the temperature $T_{\rm mid}$. The end of the upper chromosphere and onset of the transition region is located at ($m_{\rm top}$, $T_{\rm top}$), and $\nabla_{\rm TR}$ gives the temperature gradient of the transition region.
[b] The parameter m_i/m_0 defines the mass load in comparison to the respective basis model.

puted by Husser et al. (2013) with $T_{\rm eff}$ = 3500 K, log g = 5.0 dex, [Fe/H] = 0.0 dex, and [α/Fe] = 0.0 dex, by a chromosphere and transition region, assuming a temperature structure characterized by linear sections in the logarithm of the column mass density for the lower and upper chromosphere as well as for the transition region. In total, we varied six free parameters in the temperature structure of the chromosphere and computed a set of 166 one-dimensional spherically symmetric chromospheric models. In creating the models, the semi-empirical, solar VAL C temperature structure was parameterized and adjusted to the M-dwarf sample. The parameterized ad hoc temperature structure represents the unknown heating mechanisms in the upper atmosphere. In addition, we assumed hydrostatic equilibrium and neglected any acoustic and magnetic waves. Convergence was achieved using nonlocal thermodynamic equilibrium (NLTE) calculations for the chromospheric lines. The grid encompasses models of various levels of activity. The spectra of the inactive models typically show the chromospheric lines in absorption, while with increasing activity, the lines go into emission. Hintz et al. (2019) optimized their models to simultaneously fit the Na I D_2, Hα, and the bluest Ca II IRT line of the stellar sample described above.

2.4. Construction of new chromospheric models

Here we extend our previous study that we performed in Hintz et al. (2019) by constructing two series of models with the specific goal of studying the behavior of the He I IR line in terms of the activity state. We varied the activity level of a given chromospheric temperature structure by shifting the whole density structure. Models shifted farther inward toward higher densities correspond to higher activity states. In particular, we performed systematic density shifts for two inactive best-fit models of Hintz et al. (2019), those designated numbers 042 and 080 therein.

The temperature structure of these two models was shifted toward higher and lower densities following the approach of Andretta & Jones (1997). Table 1 lists the model parameters, and Fig. 2 depicts the temperature structures of these series of models. The change in the column mass density is described by m_i/m_0 relative to the basis model 042, hereafter called model A2 within the new series designated by A, while former model 080 is hereafter called model B4 in series B. Model A1 (blue line in Fig. 2) of the A series represents the least active state with the column mass density of the layers being about ten times lower than that of the original model A2. Model A4 (green line) has the largest inward shift (m_i/m_0 = 4.47), corresponding to the highest activity state of the series.

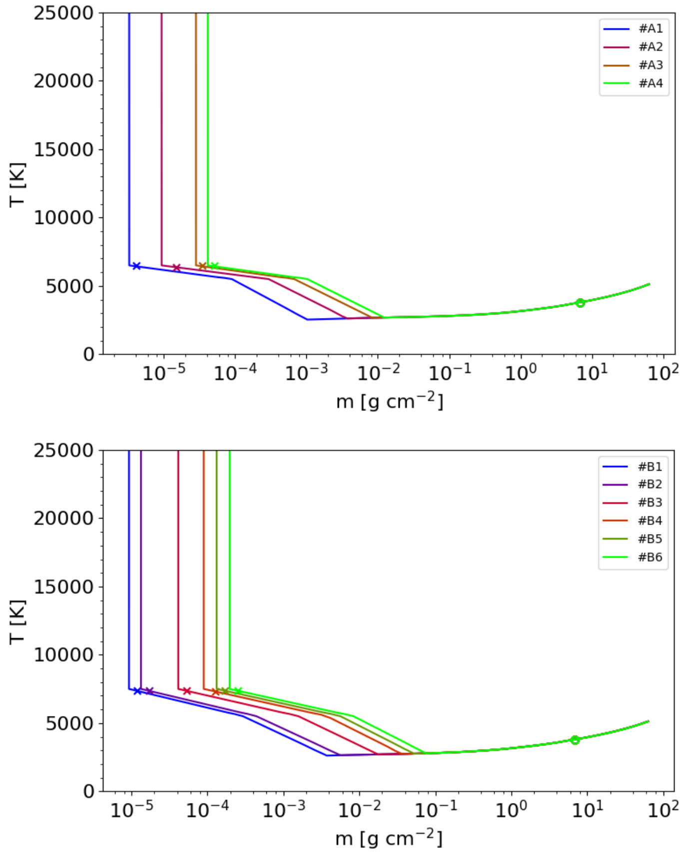

Fig. 2. Model temperature profiles as a function of the column mass densities. The respective model parameters are given in Table 1. The temperature structures of series A are shown in the *top panel*, and those of series B are depicted in the *bottom panel*. Models A2 and B4 in these series correspond to models 042 and 080 from Hintz et al. (2019), respectively. In both series, we also mark the structural positions where the He I IR line core (crosses) and continuum at λ = 10 834.5 Å (open circles) approach an optical depth of τ = 1, i. e., where both become optically thick.

Because we shifted the atmospheric structure on a given discontinuous column mass grid, we obtained deviations in the gradients of the different linear sections. We allowed a tolerance deviation at maximum of 15 % for the gradients compared to the gradients of the respective basis model. Therefore the series are not equidistant on the column mass grid. While the NLTE level occupation numbers of the models in series A and B converge during the iteration process of the model computation as described in Hintz et al. (2019), further inward shifts of the innermost models come along with nonconverged atmospheres. Thus, models A4 and B6 yield the limit of the inward density shift of the respective series.

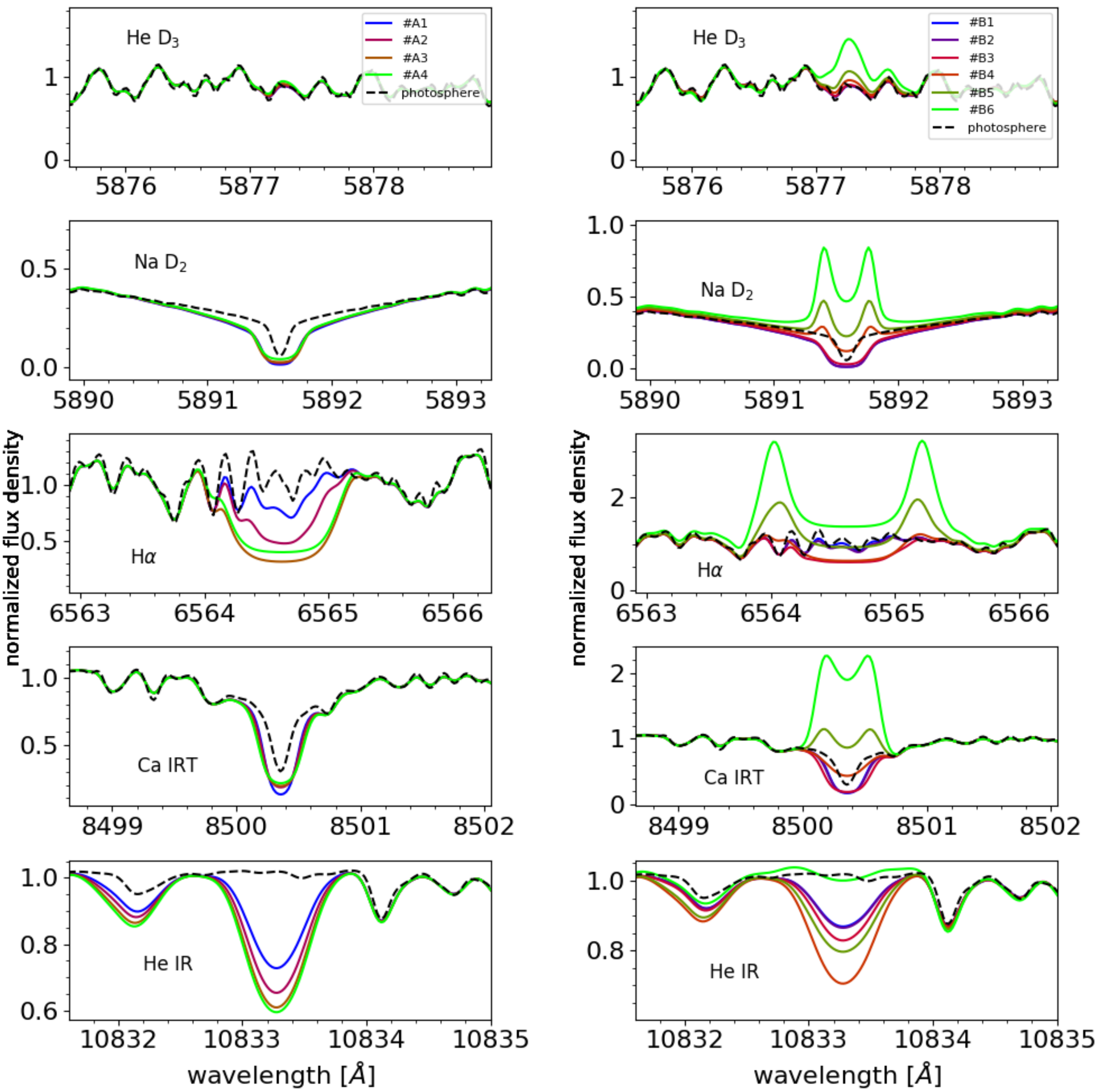

Fig. 3. Spectra according to the temperature structures of the new series A (*left panel*) and B (*right panel*) of models in Fig. 2 (corresponding color-coding) in the spectral ranges of He I D_3, Na I D_2, Hα, the bluest Ca II IRT line, and the He I IR line (from *top* to *bottom*). For comparison, the underlying photosphere model ($T_{\rm eff}$ = 3500 K, $\log g$ = 5.0 dex, [Fe/H] = 0.0 dex, [α/Fe] = 0.0 dex) is plotted as well. The photosphere is taken from Husser et al. (2013).

2.5. New model spectra

From both new series A and B of model atmospheres as given by the chromospheric temperature structures in Fig. 2 we obtained model spectra that are shown in the wavelength ranges of the chromospheric lines of He I D_3, Na I D_2, Hα, the bluest Ca II IRT line, and the He I IR line in Fig. 3. The series show the evolution of these chromospheric lines with increasing activity, that is, the inward shifting of the models. The outermost models with the respective lowest densities, A1 and B1, already show absorption in the He I IR line. Models representing higher activity levels lead to an increase in absorption strength, with model A4 exhibiting the strongest absorption line in series A. In series B, model B4 displays the highest absorption depth, while for models B5 and B6, the He I IR line fills in. In Fig. 2 we also indicate where the He I IR line core and neighboring continuum become optically thick. The corresponding temperatures for the He I IR line core range between 6350 K and 6450 K for series A and between 7300 K and 7400 K for series B. The continuum temperatures are in both cases at ~ 3800 K. The optically thick temperature regions of the line core indicate a He I IR line formation in the upper chromosphere. Furthermore, we determined whether geometric effects caused by the chromospheric extension above the photosphere contribute to the He I IR line formation in our spherically symmetric models. We were unable to find significant geometric effects with respect to the He I IR line formation.

A comparable behavior is observed in the Hα line, where model A4 already shows fill-in. This means that the evolution of Hα seems to be shifted compared to that of the He I IR line in series A. In series B, model B3 displays maximum absorption in Hα and model B4 just starts to fill in, which is slightly more strongly visible in the wings. In models B5 and B6, the Hα line tends to go into emission. However, the Hα lines of models B5 and especially B6 exhibit strong trough-like self-absorption features, suggesting that at least model B6 does not represent a real stellar spectrum because even during flares no such broad self-absorption troughs have been observed. This demonstrates that not every parameterized chromosphere leads to realistic spectra.

The He I D_3 line is not visible at all in series A. Only in series B does the line arise beyond the continuum when the activity levels increase: model B5 shows the line in slight emission, and a clear He I D_3 emission line appears in model B6. In the cases of the Na I D_2 and the bluest Ca II IRT line, the evolution is different than in the other cases: the lines start at a maximum absorption depth and fill in for both series while shifting the whole atmospheric structure farther inward. For series B, the response of the lines is again stronger, and for the two innermost models B5 and B6, these lines go into emission.

2.6. Flare classification and model selection

In our investigation of the formation of He I IR line, we focused on quiet atmospheres. Therefore we identified models representing high-activity states (flaring). To that end, we followed observational findings in the spectra. Because Hα can be observed in emission during the quiescent state, the line is not well suited as a flare criterion; the same applies for most chromospheric lines in the optical. In contrast, we are not aware of Paschen emission line observations outside of flares, while the line was observed in emission during M-dwarf flares (Schmidt et al. 2012; Fuhrmeister et al. 2008; Liebert et al. 1999; Paulson et al. 2006). Therefore we used the Paβ emission as a discriminator for flaring activity. With this criterion, we identified the highest activity states.

In particular, we computed the pEW for Paβ at 12821.57 Å. For the line core, we assumed a width of 0.5 Å, and the reference bands were located at $12\,811.5 \pm 1.0$ Å and $12\,826 \pm 1.0$ Å. Each model yielding a pEW value below −0.02 Å was considered a flare model and was omitted in the detailed analysis of the He I IR line. One model (number 166 from Hintz et al. 2019) passed this criterion, but the Paβ line developed broad emission wings that reached into the reference bands. Including this model, a total of 81 models were flagged as flaring and were excluded from further consideration.

We also neglected models with a transition region onset below 6000 K. It might be argued that the onset of the transition region occurs where hydrogen becomes completely ionized and hence no longer is an efficient cooling agent. While this occurs only at about 8000 K, hydrogen becomes partially ionized above 5000 K so that cooling starts to diminish (Ayres 1979).

In total, we investigated a subsample of 58 models from Hintz et al. (2019) that fulfilled our selection criteria for inactive chromospheres; these models and the parameter configurations are listed in Table A. Because we are interested in investigating nonflaring models and the evolution of the He I IR line as a function of increasing activity, we took two best-fit models of inactive stars from our previous work and varied their activity state. We thus included eight newly calculated models from series A and B in our investigation even though models B5 and B6 did not pass the Paβ criterion.

3. Results and discussion

3.1. Model EUV flux and its effect on the He I IR line

The wavelength range of the EUV is self-consistently calculated within the PHOENIX models according to the prescribed atmospheric structure. The maximum temperature is 98 000 K in all of our models. We did not extend the models to higher temperatures because then conduction plays a major role that is not incorporated in the PHOENIX models. In this regard, the models underpredict the EUV radiation field because the upper part of the transition region and the corona are neglected.

Andretta & Jones (1997) highlighted that it is important that the EUV radiation field is irradiated from the solar transition region and corona in the formation of the He I spectrum of the Sun. Omitting the radiation field in the VAL C model of the quiet Sun, the authors obtained a model spectrum without any visible He I line. We repeated this exercise exemplarily for one of our inactive models A2 and of our most active model B6, and show the resulting He I IR line in Fig. 4. While the original model spectra were calculated down to a wavelength of 10 Å, we cut off the wavelength range $\lambda \leq 504$ Å and left everything else unchanged. In the spectrum of the modified model A2, the He I IR line completely vanishes, while the self absorption of the fill-in seen in model B6 turns into a slight emission line without any sign of self-absorption. This indicates that in the PHOENIX model calculations the PR mechanism is important in populating the metastable $2\,^3S$ level of helium to obtain any absorption feature in the first place. Because the PR mechanism is eliminated in the modified model B6, the emission is caused by collisional excitation alone.

We calculated the emanating EUV radiation of our PHOENIX models by integrating the flux density in the wavelength range of $10\,\text{Å} \leq \lambda \leq 504\,\text{Å}$ ($F_{\rm EUV}$) and related it to the integrated bolometric flux ($F_{\rm bol}$). In Fig. 5 we show the pEW(He I IR) as a function of the EUV radiation field as measured by $F_{\rm EUV}/F_{\rm bol}$. The values of $F_{\rm EUV}/F_{\rm bol}$ from our nonflaring PHOENIX models (all models investigated in this work except for models B5 and B6) as shown in Fig. 5 range from 4.5×10^{-7} for model 047 to 1.48×10^{-4} for model A4. These values are difficult to compare to observations because EUV observations for M dwarfs are especially hard to come by. Nevertheless, we can compare our values to the estimated EUV radiation field of GJ 176 from Loyd et al. (2016), obtained in the context of the Measurements of the Ultraviolet Spectral Characteristics of Low-mass Exoplanetary Systems (MUSCLES) Treasury Survey. The estimated $F_{\rm EUV}/F_{\rm bol}$ value of GJ 176 from Loyd et al. (2016) is in the order of 10^{-5}, which is slightly higher than the typical value that we obtain for our nonflaring PHOENIX models; the median of $F_{\rm EUV}/F_{\rm bol}$ of the nonflaring models is 8.9×10^{-6}. GJ 176 is slightly above our effective temperature range with $T_{\rm eff} = 3689 \pm 54$ K (Passegger et al. 2019). We therefore conclude that the calculated $F_{\rm EUV}/F_{\rm bol}$ values from our nonflaring PHOENIX chromospheres are compatible with observational results of EUV radiation, although our models neglect the temperature region of the upper transition and corona because of the model temperature limit of 98 000 K. However, compared to real stars, our models presumably contain too much material in the lower transition region, and this might therefore compensate

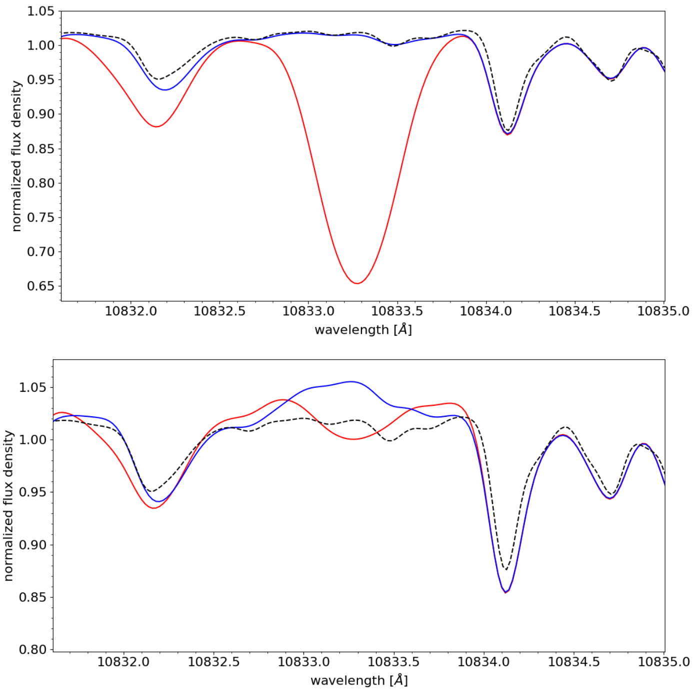

Fig. 4. Spectral ranges of the He I IR line in models A2 (*upper panel*) and B6 (*lower panel*) in the original configuration (red lines) and when the radiation field below 504 Å (blue lines) is omitted. The dashed black line shows the underlying photosphere alone (from Husser et al. (2013) with $T_{\rm eff}$ = 3500 K, $\log g$ = 5.0 dex, [Fe/H] = 0.0 dex, and [α/Fe] = 0.0 dex).

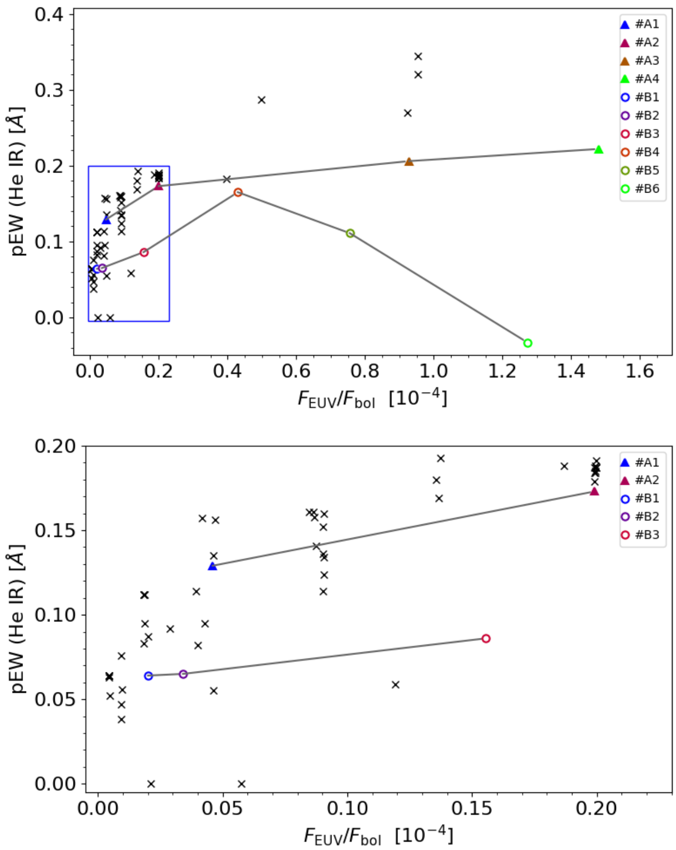

Fig. 5. He I IR pEW as a function of the integrated EUV flux at $\lambda \leq 504$ Å (vacuum). The color-coded models correspond to the new series A and B of models as given in Fig.2. Black crosses represent the previously nonflaring models from Hintz et al. (2019) as given in Table A. The region marked by the blue rectangular in the *upper panel* is enlarged in the *lower panel* and shows our most quiescent models.

for the material that we omitted in the upper transition region and corona. This means that we obtain realistic $F_{\rm EUV}/F_{\rm bol}$ within our models despite this inadequacy. For a recent detailed analysis of a synthetic EUV PHOENIX spectrum computed for the inactive M dwarf Ross 905, we refer to the study by Peacock et al. (2019).

The graph in Fig. 5 shows that an increase in the strength of the radiation field in the transition region tends to deepen the He I IR line. The effect of the radiation field on the line strength decreases at higher irradiation levels. For $F_{\rm EUV}/F_{\rm bol} \lesssim 2.0 \times 10^{-5}$, absorption in the He I IR line strongly increases in response to a comparably weak rise of the integrated EUV flux. When the models are shifted farther inward, the EUV flux increases more strongly, but the He I IR line strength only changes slowly. The pEW(He I IR) seems to saturate or even starts to fill in for higher $F_{\rm EUV}/F_{\rm bol}$ values. Our modeling yields a maximum absorption depth at pEW = 0.35 Å for model 057.

The comparison of the results for series A and B shows that both series yield a qualitatively similar behavior within the low-activity regime of the pEW(He I IR) vs. $F_{\rm EUV}/F_{\rm bol}$ plane, although they differ in their model parameters such as the temperature gradient in the transition region. However, the extent of the response of the radiation field and the line depth on the shift of the models depends on the series. In both cases, the chromospheres are equal in thickness on the column mass density scale, but the gradients of the upper chromospheres and transition regions differ from each other. This difference affects the density at the temperatures where the PR mechanism works in the He I IR line formation. Fig. 5 shows that the effect of shifting the prescribed atmospheric structure in series B is stronger than in A. In model series A, the line absorption monotonically increases with increasing $F_{\rm EUV}/F_{\rm bol}$. In the other model series, model B4 exhibits the highest absorption level (pEW = 0.165 Å) at $F_{\rm EUV}/F_{\rm bol} = 4.3 \times 10^{-5}$. A further inward shift results in filling in the line with a further increase in the radiation field. Because the maximum absorption depth is not reached for series A, the saturation level does not appear to be determined solely by the position of the chromospheric structure in the atmosphere, but also depends on other parameters such as temperature gradients or the temperature at the onset of the transition region.

3.2. Comparison to observations

Fuhrmeister et al. (2019) compared the pEW(He I IR) measurements of their investigated M-dwarf sample to X-ray observations that can serve as a proxy of the EUV radiation field. For their inactive and quiescent stars, they found that for low $\log L_X/L_{\rm bol}$ values the full range of pEW(He I IR) values was observed. For high X-ray luminosities, only high pEW(He I IR) values were seen, that is, there is some sort of lower envelope that is correlated with $\log L_X/L_{\rm bol}$. This lower envelope has the steepest gradient for M0 dwarfs, while later subtypes exhibit lower gradients, with M3–4 dwarfs showing no dependence on $\log L_X/L_{\rm bol}$. For the M2–3 dwarfs considered here, they therefore only found a very weak tendency for high $\log L_X/L_{\rm bol}$ values excluding low pEW(He I IR) values.

Our models, on the other hand, show a correlation between the pEW(He I IR) and $F_{\rm EUV}/F_{\rm bol}$ measurements. Nevertheless, this need not necessarily be a discrepancy. We do not know

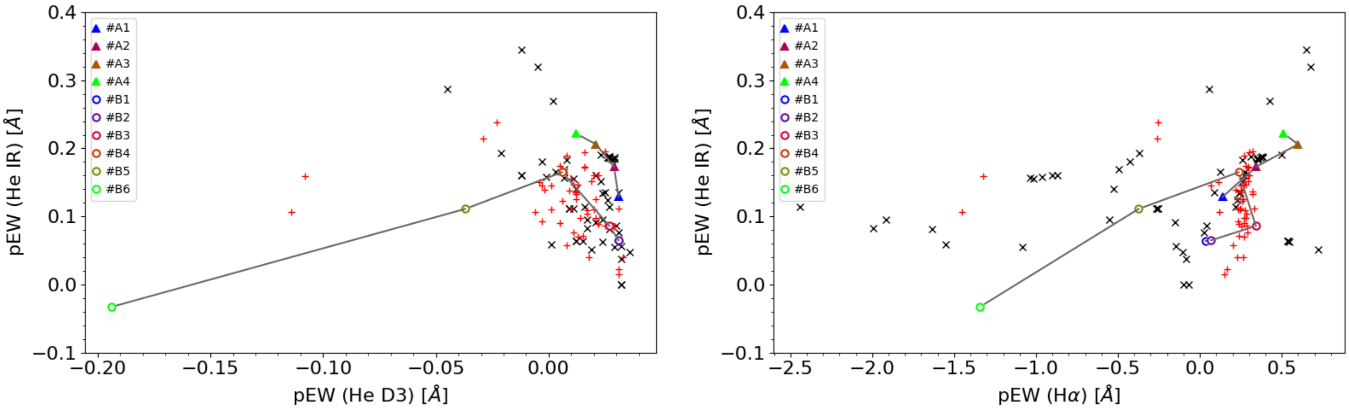

Fig. 6. pEWs of the He I IR line as a function of the pEWs of the He I D_3 (*left panel*), and Hα (*right panel*) lines. Black crosses represent the nonflaring models from Hintz et al. (2019). Series A and B are depicted by color-coded squares (the color-coding corresponds to that of Fig. 2). CARMENES observations of the investigated M2–M3 V stars are flagged by red pluses. In the observed pEW(He I D_3) of the stellar sample, we add an offset of 0.06 Å because these measurements are influenced by a decline in flux in the respective normalization reference bands from the blue to the red continuum.

which $F_{\rm EUV}/F_{\rm bol}$ values the observations span, but when we take only the nonflaring measurements into account, they are probably covered by a subset of models from the zoom-in (lower panel in Fig. 5). When only the models with $0.04{\times}10^{-4} < F_{\rm EUV}/F_{\rm bol} < 0.1{\times}10^{-4}$ are considered, the situation starts to look similar to the observations: while the upper envelope of the pEW(He I IR) values is quite constant, the lower envelope shows some rise. Moreover, the spread in pEW(He I IR) seen for the models for a distinct $F_{\rm EUV}/F_{\rm bol}$ value should dilute a possible correlation even more in the observations because they are additionally prone to measurement errors, errors arising from using X-ray fluxes as approximation for $F_{\rm EUV}$, and from nonsimultaneous measurements in X-ray and pEW(He I IR).

Nevertheless, Fuhrmeister et al. (2019) also found some saturation limit that depended on spectral type, which is about $\rm pEW_{sat}$=0.25 Åfor spectral types M2.0–2.5 V and $\rm pEW_{sat}$=0.2 Å for M3.0–3.5 V stars. This agrees with the overall saturation limit found by the models, although individual models predict even deeper He I IR lines. The EUV radiation where the response of the He I IR line saturates in our model series B may be connected with a change in formation mechanism, that is, the collisional excitation becomes dominant because the models B5 and B6 are flare models and the observations by Fuhrmeister et al. (2019) with positive pEW(He I IR) are connected with flaring events. Omitting the EUV radiation in the models also supports this conclusion because an inactive chromosphere model without EUV radiation does not show any signal of the He I IR line, and an active model tends to show the He I IR line in emission.

3.3. He I *IR in relation to other chromospheric lines*

In Fig. 6 we show the pEW measurements of the stars and our models for the He I IR line as a function of pEW(He I D_3) and pEW(Hα). The models show the He I IR line from the state of absorption to being indistinguishable from the surrounding photospheric background, which may indicate a very weak or a filled-in line. In the original model suite, the He I IR line emission is only found in combination with Paβ line emission, which led to their exclusion (Sect. 2.6). This is in line with observations, where He I IR line emission was observed during flares (Schmidt et al. 2012; Fuhrmeister et al. 2008).

In the measurements of the He I D_3 line we found an offset between the observations and the model values. The surrounding continua exhibit a decline from the blue to the red reference bands for the observations, which affects the normalization in the calculations of the pEW values of these lines. Therefore we added an offset of 0.06 Å to the pEW measurements of the observations. The behavior of the He I D_3 line is easiest to interpret because it only slightly starts to rise above the continuum with increasing depth of the He I IR line for the models as well as for the observations. The series of models created here also shows this trend for all models of series A and for models B1 – B4, that is, for all the quiescent models of the new series. The flare models B5 and B6 show increasing fill-in of the He I IR line, while the line emission of He I D_3 strengthens further. The same applies to the two most active stars of the observed sample. Furthermore, within the inactive range of the models and observations, the He I IR sensitivity to the density shift is notably higher than that of the D_3 line. This is also confirmed by the respective line evolution shown in Fig. 3. This is in line with expectations because the lower level of the D_3 line is the upper level of the He I IR line. The population of the excited D_3 level lags the population of the excited He I IR level.

The Hα line behavior in the models shows that no combination of a deep He I IR line and Hα clearly in emission appears to be possible. Nevertheless, the model series A and B and the measurements of the observed stars show the same trend: Hα behaves similarly to the He I IR line: first the line deepens before some fill-in begins that eventually drives the lines into emission.

We also studied the relationship of pEW(He I IR) to pEW(Na I D_2) and pEW(Ca II IRT). For these lines, the models seem to show no dependence on the pEW(He I IR). Nevertheless, the observations show that both lines only fill in with increasing activity. For a weak He I IR line, measurements of the Ca II IRT or Na I D_2 line therefore determine if the He I IR line is intrinsically weak or filled in.

For all lines, the observed pEW combinations are generally well reproduced by the models. Only the observations of the two active stars TYC 3529-1437-1 and LP 733-099 show a combination in the pEW(He I IR) versus pEW(He D_3) plane that is not covered by the models. Furthermore, the models hardly reproduce the pEW measurements of the stars in the very inactive regime of the pEW(He I IR) versus pEW(Hα) space. For some

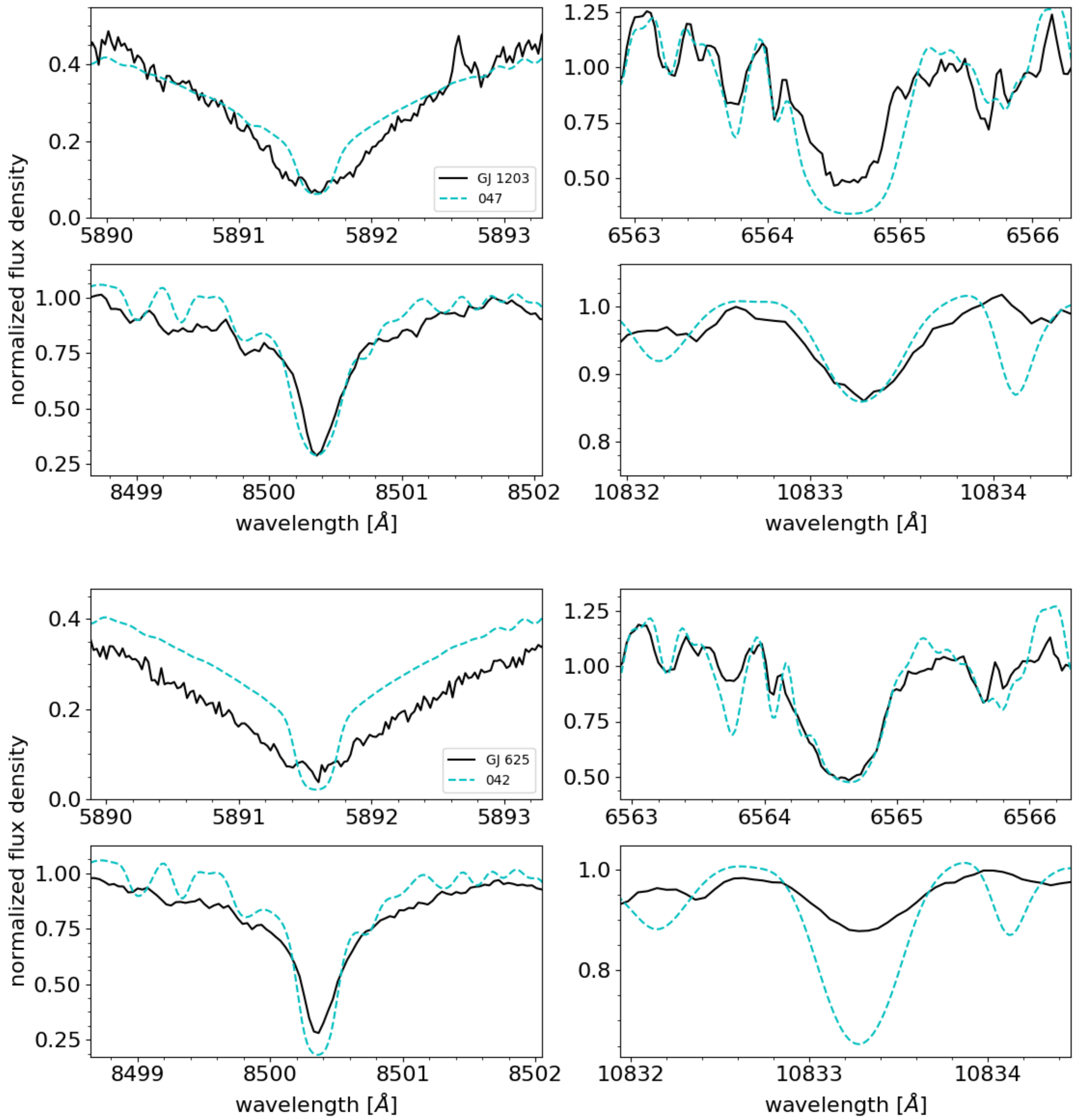

Fig. 7. *Upper panel:* Comparison of the best-fit model spectrum (dashed cyan line, model 047) to an observed spectrum (solid black line) of GJ 1203 optimized for the lines of Na I D_2 (*top left panel*), Hα (*top right panel*), and the bluest Ca II IRT line (*bottom left panel*). In the range of the He I IR line (*bottom right panel*), the observed CARMENES template obtained with SERVAL is shown. The emission line redward of the Na I D_2 line in the observation of GJ 1203 is an airglow line. *Bottom panel:* Same as in the upper plot for GJ 625 (model 042).

discussion on these aspects, see Sect. 3.4. However, the quiescent models of series A and B mainly follow the observations of the inactive stars.

3.4. Predicting the He I IR line from previous best-fitting models

On the basis of the chromospheric modeling as done in Hintz et al. (2019), we here determined how well the models reproduce the He I IR line. In that study, only the Na I D_2, Hα, and the bluest Ca II IRT line were used to identify best-fit models for all stars by minimizing a modified χ^2 value (χ^2_m) for these three lines.

Examples of the inactive stars (with single-model fits) can be found in Fig. 7 for GJ 1203 and GJ 625. Here we show the three lines that were used before and the predicted line shape of the He I IR line, which is reproduced well for GJ 1203 and overpredicted for GJ 625. However, all of our best-fit models show the He I IR line in absorption and therefore reproduce this characteristic of the observed stellar sample. As an indicator for the goodness of the prediction of the respective models in the range of the He I IR line, we calculated reduced χ^2 values in the wavelength interval 10 833.306 ± 0.5 Å ($\chi^2_{\text{He I IR}}$). The two different χ^2 quantities, $\chi^2_{\text{He I IR}}$ and χ^2_m, are not directly comparable. Here we analyze the prediction of the modeled He I IR line, therefore we only compare the $\chi^2_{\text{He I IR}}$ values (see Table 2). From visual inspection, we specified a $\chi^2_{\text{He I IR}} \leq 2$ to flag a model prediction of the He I IR line to be adequate for an observation. Approximately for half of the listed stars, the best-fit model prediction is appropriate according to this selection criterion. When the model pre-

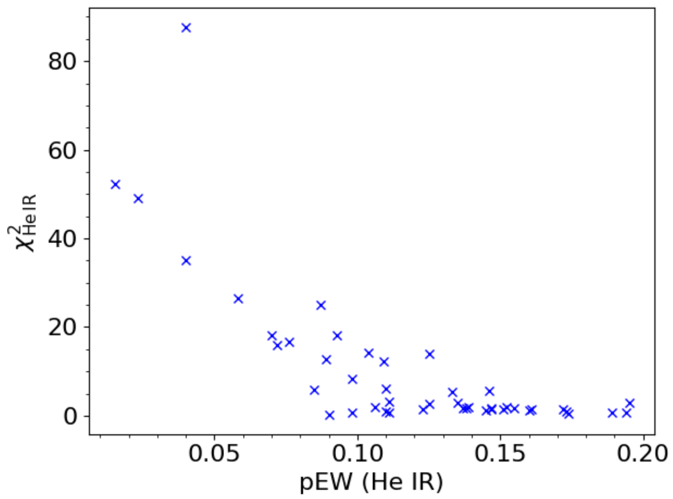

Fig. 8. Measurements of the pEW (He I IR) plotted against the corresponding $\chi^2_{\rm He\,I\,IR}$ values for the inactive stars from Table 2.

diction strongly differs, that is, $\chi^2_{\rm He\,I\,IR} > 10$, the He I IR line absorption is clearly overpredicted, as shown in Fig. 7 for GJ 625.

Because Hintz et al. (2019) identified only five best-fit models in their the whole sample of inactive stars in our previous study, we now determine which of those five models describes the He I IR line best and then recompute the χ^2_m values for this model. These results are shown in Table 2. The He I IR line is best predicted by models 029 and 047 for all but three stars. These models in many cases describe the He I IR line better and show only a marginally worse new χ^2_m value. A prominent example is GJ 3452. On the other hand, the description of the two most inactive stars, Ross 730 and HD 349726, within the He I IR line is poor for any of the five best-fit models. This leads us to the general assumption that the He I IR line prediction becomes worse when the line is shallow, as is shown in Fig. 8. This may be caused by a lack of appropriate inactive models in our model suite or may indicate that our ansatz with a 100% filling factor for the chromospheres fails and even atmospheres of the most inactive stars are partially filled with plage regions. The cases for which the original best fits already yield an adequate He I IR line description can by construction lead to an even better description, but it considerably worsens the χ^2_m in most cases. This shows that more than one individual line needs to be used for chromospheric model fitting, as reported by Hintz et al. (2019).

Hintz et al. (2019) found that in the case of the active stars, linear-combination fits of two models (one inactive and one more active model) were necessary to obtain appropriate models. In Fig. 9 we illustrate the best linear combination fit for TYC 3529-1437-1. In the combination fits of the active stars, the line in the active component tends to go into emission, but the combination still shows the He I IR line in absorption. Table 3 lists our information about the He I IR line prediction of the combination fits of the active stars. Interestingly, the He I IR line can be well reproduced by the best-fit model combinations without including this line in the fitting procedure, as is evident from the $\chi^2_{\rm He\,I\,IR}$ values.

4. Summary and conclusions

We presented a theoretical study of the He I IR line in M2–3 V stars with PHOENIX. Our study was based on a set of chromospheric PHOENIX models computed in our previous study, Hintz et al. (2019), and new systematic series of chromospheric models. Following the approach of previous M-dwarf star studies, all our models (previous and new models) were created by parameterizing the semiempirical solar VAL C temperature structure. The model spectra were then used to fit observed CARMENES spectra of M2–3 V stars in the Na I D$_2$, Hα, and the bluest Ca II IRT lines. A statistical analysis reveals the best fits. Here, we extended the study to investigate the behavior of the He I IR line.

Table 2. Best-fit models for the inactive stars from Table A.1 of Hintz et al. (2019) and the calculated reduced χ^2 value (Col. 4) in the He I IR line.

Stars	Model	χ^2_m	$\chi^2_{\rm He\,I\,IR}$	Model [a]	χ^2_m [a]	$\chi^2_{\rm He\,I\,IR}$ [a]
Wolf 1056	047	2.75	1.80	029	4.73	0.62
GJ 47	047	2.53	1.79	029	4.14	0.38
BD+70 68	080	2.26	0.72	079	2.74	0.72
GJ 70	079	2.29	1.95	029	4.85	0.41
G 244-047	042	3.45	5.73	029	4.22	0.95
VX Ari	079	3.61	6.10	047	4.11	0.73
Ross 567	042	2.75	18.21	047	3.26	0.49
GJ 226	047	1.80	1.67	029	4.52	0.48
GJ 258	047	3.83	1.36	029	5.27	0.46
GJ 1097	042	4.04	12.79	047	4.34	0.47
GJ 3452	042	2.37	18.09	047	2.99	0.33
GJ 357	042	2.63	35.03	047	3.25	1.85
GJ 386	047	2.78	1.51	029	4.00	0.78
LP 670-017	080	4.51	5.92	047	4.53	0.37
GJ 399	079	2.54	1.89	029	5.10	0.62
Ross 104	079	2.59	2.58	029	4.44	0.46
Ross 905	042	2.84	12.23	047	2.94	0.75
GJ 443	080	2.04	1.39	029	7.48	0.74
Ross 690	079	2.41	5.27	047	2.81	1.31
Ross 695	042	2.91	87.59	047	3.16	5.80
Ross 992	079	2.85	1.67	029	5.18	0.42
θ Boo B	047	2.55	0.78	047	2.55	0.78
Ross 1047	047	3.16	0.94	029	4.41	0.72
LP 743-031	080	3.38	14.27	047	4.69	0.97
G 137-084	080	2.66	1.96	029	4.97	0.36
EW Dra	080	2.31	0.46	080	2.31	0.46
GJ 625	042	2.41	25.02	047	2.43	0.63
GJ 1203	047	2.50	0.24	047	2.50	0.24
LP 446-006	047	2.82	1.11	029	3.72	1.03
Ross 863	079	3.11	3.08	029	4.02	0.60
GJ 2128	042	2.45	16.69	047	2.58	0.41
GJ 671	042	3.30	15.92	047	3.55	0.31
G 204-039	080	2.79	1.34	029	5.82	0.38
Ross 145	042	3.28	26.56	047	4.19	0.71
G 155-042	042	3.54	8.40	047	3.56	0.76
Ross 730	029	2.82	52.27	047	6.02	15.92
HD 349726	029	2.83	49.21	047	5.61	14.22
GJ 793	080	3.01	1.17	029	7.02	0.37
Wolf 896	047	2.59	2.83	079	2.66	0.73
Wolf 906	079	2.43	0.92	029	5.29	0.65
LSPM J2116 +0234	079	3.08	1.54	029	5.10	0.57
BD-05 5715	080	2.90	0.69	080	2.90	0.69
Wolf 1014	042	3.32	13.91	047	4.21	0.94
G 273-093	047	1.97	0.74	047	1.97	0.74
Wolf 1051	080	2.31	2.94	029	6.39	0.68

[a] Columns 5–7 list the results of the model with the best He I IR line prediction within the subsample of the five best-fitting models for the inactive stars. For stars whose original model already resulted in an adequate description of the He I IR line, we mark the He I IR line best-fit model in gray.

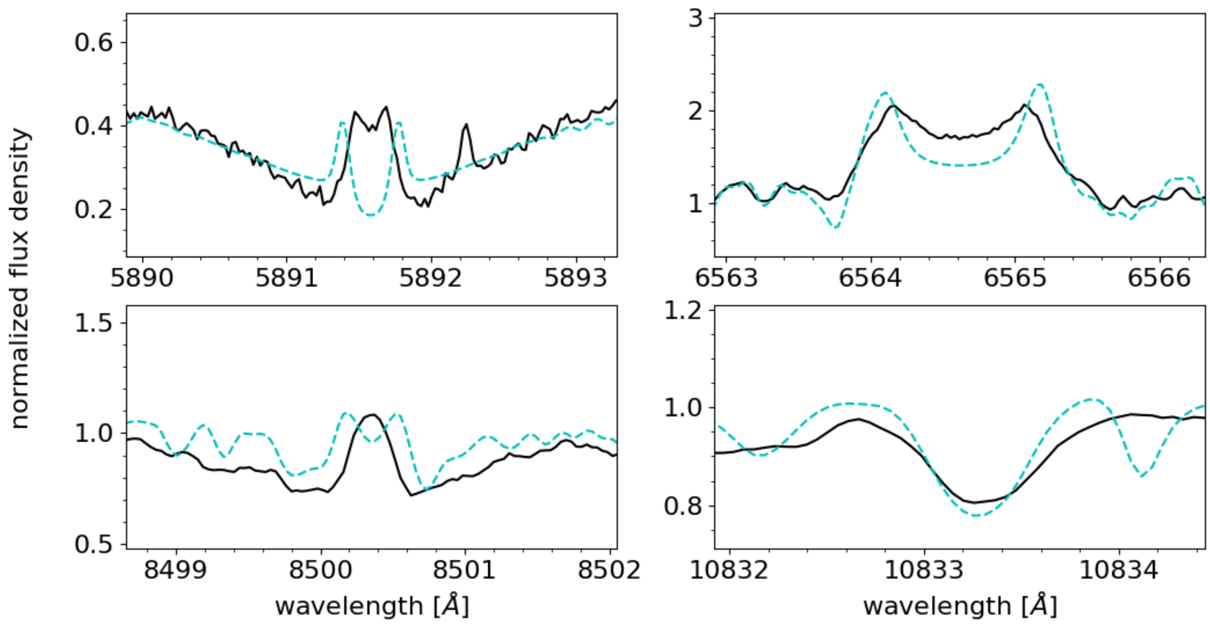

Fig. 9. Comparison of the best linear combination fit (dashed cyan line, from Hintz et al. (2019)) to an observed spectrum (solid black) TYC 3529-1437-1 optimized for the lines of Na I D_2 (*top left panel*), Hα (*top right panel*), and the bluest Ca II IRT line (*bottom left panel*) and extended to the He I IR line (*bottom right panel*). The linear combination consists of 74.9% of inactive model 079 and 25.1% of active model 149.

Table 3. Best-fit models of the active stars in a linear-combination fit with filling factors (FF) and the calculated χ^2 value (Col. 5) in the He I IR line.

Stars	Inactive model	FF	Active model	FF	χ^2_m	$\chi^2_{\mathrm{He\,I\,IR}}$
G 234-057	080	0.90	139	0.10	3.58	1.54
GJ 360	080	0.82	132	0.17	5.13	0.70
LP 733-099	079	0.68	149	0.32	16.13	0.48
TYC 3529-1437-1	079	0.75	149	0.25	14.25	0.50

Our new model series were computed by shifting an inactive model structure in column mass density. In these series, denser chromospheres correspond to higher activity levels. From low to high activity levels, our models predict that the He I IR line first goes into absorption and then reaches a maximum depth, after which fill-in sets in. Our models reproduce the point of maximum He I IR line absorption at $\sim$ 300 mÅ. The Hα line shows the same qualitative behavior, but reaches the turning point at lower activity levels. In contrast, the Na I D_2 and the bluest Ca II IRT lines only show fill-in with increasing activity levels. Furthermore, the He I D_3 line never shows absorption in our models, but directly goes into emission with increasing activity levels.

By investigating the He I IR line as a function of the EUV radiation field arising from the models themselves, we find that the most inactive models are highly sensitive to an increase in EUV radiation, which produces a strong rise in the pEW(He I IR). With further increases of the EUV radiation, the line absorption tends to saturate. The detailed response of the radiation field and the He I IR line to density shifts of the atmospheric structure depends on the configuration of the chromosphere.

Suppressing EUV emission and thus the PR mechanism altogether, we showed that collisional excitation gains in importance for the formation of the He I IR line as activity levels increase beyond the point of maximum He I IR line absorption. Our investigation of chromosphere models showed that the PR mechanism and collisional excitation both contribute to the He I IR formation, with the PR mechanism dominating the low-activity regime. This is in line with former results on the He I IR line formation in the Sun.

The whole stellar comparison sample shows the He I IR line in absorption. We showed that the best-fit models for inactive stars selected by Hintz et al. (2019) based on optical activity indicators often also predict the He I IR line quite well. In other cases, an appropriate inactive model can be found that fits both the optical and He I IR lines well. For active stars, a linear combination of an active and inactive component is required to obtain a good approximation, as reported in Hintz et al. (2019).

Our current study demonstrates that one-dimensional PHOENIX model atmospheres with a parameterized temperature structure reproduce the observed behavior of the He I IR line in M2–3 V stars. Its strong response to EUV irradiation in the low-activity regime makes the He I IR line a promising proxy of this otherwise inaccessible wavelength range there. The comparably weak response of the line to changes in the EUV radiation field that start already at moderate activity levels is favorable for planetary transmission spectroscopy of active stars, where constant reference spectra are crucial.

Acknowledgements. CARMENES is an instrument for the Centro Astronómico Hispano-Alemán de Calar Alto (CAHA, Almería, Spain). CARMENES is funded by the German Max-Planck-Gesellschaft (MPG), the Spanish Consejo Superior de Investigaciones Científicas (CSIC), the European Union through FEDER/ERF FICTS-2011-02 funds, and the members of the CARMENES Consortium (Max-Planck-Institut für Astronomie, Instituto de Astrofísica de Andalucía, Landessternwarte Königstuhl, Institut de Ciències de l'Espai, Institut für Astrophysik Göttingen, Universidad Complutense de Madrid, Thüringer Landessternwarte Tautenburg, Instituto de Astrofísica de Canarias, Hamburger Sternwarte, Centro de Astrobiología and Centro Astronómico Hispano-Alemán), with additional contributions by the Spanish Ministry of Science [through projects AYA2016-79425-C3-1/2/3-P, ESP2016-80435-C2-1-R, AYA2015-69350-C3-2-P, and AYA2018-84089], the German Science Foundation through the Major Research Instrumentation Programme and DFG Research Unit FOR2544 "Blue Planets around Red Stars", the Klaus Tschira Stiftung, the states of Baden-Württemberg and Niedersachsen, and by the Junta de Andalucía. D.H. acknowledges funding by the DLR under DLR 50 OR1701. B.F. acknowledges funding by the DFG under Cz 222/1-1 and Schm 1032/69-1. S.C. acknowledges support through DFG projects SCH 1382/2-1 and SCHM 1032/66-1. We thank the anonymous referee for the comprehensive review.

References

Andretta, V. & Giampapa, M. S. 1995, ApJ, 439, 405
Andretta, V. & Jones, H. P. 1997, ApJ, 489, 375
Avrett, E. H., Fontenla, J. M., & Loeser, R. 1994, in IAU Symposium, Vol. 154, Infrared Solar Physics, ed. D. M. Rabin, J. T. Jefferies, & C. Lindsey, 35
Ayres, T. R. 1979, ApJ, 228, 509
Caballero, J. A., Guàrdia, J., López del Fresno, M., et al. 2016, in Proc. SPIE, Vol. 9910, Observatory Operations: Strategies, Processes, and Systems VI, 99100E
Fuhrmeister, B., Czesla, S., Hildebrandt, L., et al. 2019, A&A, 632, A24
Fuhrmeister, B., Liefke, C., Schmitt, J. H. M. M., & Reiners, A. 2008, A&A, 487, 293
Hauschildt, P. H. 1992, J. Quant. Spectr. Rad. Transf., 47, 433
Hauschildt, P. H. 1993, J. Quant. Spectr. Rad. Transf., 50, 301
Hauschildt, P. H. & Baron, E. 1999, Journal of Computational and Applied Mathematics, 109, 41
Hintz, D., Fuhrmeister, B., Czesla, S., et al. 2019, A&A, 623, A136
Husser, T.-O., Wende-von Berg, S., Dreizler, S., et al. 2013, A&A, 553, A6
Leenaarts, J., Golding, T., Carlsson, M., Libbrecht, T., & Joshi, J. 2016, A&A, 594, A104
Liebert, J., Kirkpatrick, J. D., Reid, I. N., & Fisher, M. D. 1999, ApJ, 519, 345
Loyd, R. O. P., France, K., Youngblood, A., et al. 2016, ApJ, 824, 102
Nagel, E. 2019, PhD thesis, University of Hamburg
Nortmann, L., Pallé, E., Salz, M., et al. 2018, Science, 362, 1388
Passegger, V. M., Schweitzer, A., Shulyak, D., et al. 2019, A&A, 627, A161
Paulson, D. B., Allred, J. C., Anderson, R. B., et al. 2006, PASP, 118, 227
Peacock, S., Barman, T., Shkolnik, E. L., et al. 2019, ApJ, 886, 77
Quirrenbach, A., Amado, P. J., Ribas, I., et al. 2018, in Society of Photo-Optical Instrumentation Engineers (SPIE) Conference Series, Vol. 10702, Society of Photo-Optical Instrumentation Engineers (SPIE) Conference Series, 107020W
Salz, M., Czesla, S., Schneider, P. C., et al. 2018, A&A, 620, A97
Sanz-Forcada, J. & Dupree, A. K. 2008, A&A, 488, 715
Schmidt, S. J., Kowalski, A. F., Hawley, S. L., et al. 2012, ApJ, 745, 14
Spake, J. J., Sing, D. K., Evans, T. M., et al. 2018, Nature, 557, 68
Takeda, Y. & Takada-Hidai, M. 2011, PASJ, 63, 547
Vaughan, Jr., A. H. & Zirin, H. 1968, ApJ, 152, 123
Vernazza, J. E., Avrett, E. H., & Loeser, R. 1981, ApJS, 45, 635
Zarro, D. M. & Zirin, H. 1986, ApJ, 304, 365
Zechmeister, M., Reiners, A., Amado, P. J., et al. 2018, A&A, 609, A12
Zirin, H. 1975a, NASA STI/Recon Technical Report N, 76
Zirin, H. 1975b, ApJ, 199, L63

Appendix A: Reviewed former model set

Here, we list the parameters of the models from Hintz et al. (2019) that we review in this work according to our selection criteria in Sect. 2.6. The non-listed models either show the line of Paβ in obvious emission or their onset of the transition region falls below a temperature of T_{top} = 6000 K.

Table A.1. Reviewed former model set and parameters from Table C.1 in Hintz et al. (2019) for the models that fulfill our selection criteria as described in Sect. 2.6.

Model	m_{min} [dex]	m_{mid} [dex]	T_{mid} [K]	m_{top} [dex]	T_{top} [K]	∇_{TR} [dex]
001	-4.0	-4.3	5500	-6.0	6000	7.5
005	-3.5	-3.8	5500	-5.5	6000	7.5
009	-3.2	-3.6	5500	-5.1	6000	7.5
014	-3.1	-3.3	5500	-5.0	6000	8.5
016	-3.0	-3.6	5500	-5.0	6000	7.5
020	-3.0	-3.3	5500	-5.0	6000	7.5
021	-3.0	-3.3	5500	-5.0	6000	7.5
023	-2.8	-3.6	5500	-5.0	6000	7.5
025	-2.8	-3.3	5500	-5.0	6000	7.5
028	-2.6	-3.2	4500	-4.5	6000	8.5
029	-2.6	-3.2	4500	-4.5	7000	8.5
031	-2.6	-3.0	4500	-4.5	6000	8.5
032	-2.6	-3.0	4500	-4.5	7000	8.5
037	-2.6	-2.8	4500	-4.5	6000	8.5
038	-2.6	-2.8	4500	-4.5	7000	8.5
040	-2.5	-3.6	5500	-5.0	6000	7.5
041	-2.5	-3.6	5500	-5.0	6200	7.5
042	-2.5	-3.6	5500	-5.0	6500	7.5
044	-2.5	-3.3	5500	-5.0	6000	7.5
046	-2.5	-2.8	5500	-4.5	6000	7.5
047	-2.5	-2.7	6500	-5.0	7000	9.2
049	-2.1	-2.6	6500	-4.5	7000	7.5
050	-2.1	-2.6	6500	-4.0	7000	9.2
055	-2.1	-2.3	5000	-4.0	6000	9.5
056	-2.1	-2.3	5500	-5.0	6000	7.5
057	-2.1	-2.3	5500	-4.5	6000	7.5
059	-2.1	-2.3	5500	-4.0	6000	9.5
060	-2.1	-2.3	6500	-5.0	7000	9.2
061	-2.1	-2.3	6500	-4.5	7000	9.2
062	-2.1	-2.3	6500	-4.2	7000	8.2
063	-2.1	-2.3	6500	-4.0	7000	9.0
064	-2.1	-2.3	6500	-4.0	7000	9.2
065	-2.0	-2.5	6500	-5.0	8000	9.2
066	-2.0	-2.5	6500	-4.5	8000	9.2
068	-2.0	-2.3	6500	-5.0	7000	9.2
069	-2.0	-2.3	6500	-4.5	7000	9.2
070	-2.0	-2.3	6500	-4.0	7000	9.2
071	-2.0	-2.2	6500	-5.0	7000	9.2
072	-2.0	-2.2	6500	-4.5	7000	9.2
073	-1.9	-2.3	6500	-4.0	7000	9.2
078	-1.8	-2.3	6500	-4.0	7000	9.0
079	-1.5	-2.5	5000	-4.0	7500	8.5
080	-1.5	-2.5	5500	-4.0	7500	8.5
081	-1.5	-2.5	6000	-4.1	7500	8.5
083	-1.5	-2.5	6000	-4.0	7500	8.5
095	-1.5	-2.3	6500	-4.5	7000	9.0
096	-1.5	-2.3	6500	-4.5	8000	9.2
097	-1.5	-2.3	6500	-4.0	7000	9.0
107	-1.0	-3.5	4000	-5.0	8000	9.5
108	-1.0	-3.5	4000	-4.5	8000	9.5
109	-1.0	-3.0	4000	-5.0	8000	9.5
110	-1.0	-3.0	4000	-4.5	8000	9.5
111	-1.0	-3.0	4000	-4.0	8000	9.5
124	-1.0	-2.5	4000	-4.0	8000	9.5
131	-1.0	-2.5	5200	-3.7	8000	9.5
152	-1.0	-2.0	4000	-4.0	8000	9.5
155	-1.0	-1.5	4000	-4.0	8000	9.5
159	-0.3	-3.0	4000	-4.5	8000	9.5

Chapter 4

Summary and outlook

4.1 Summary

In this thesis, chromosphere models have been computed that are capable of simultaneously reproducing chromospheric lines of different atomic species. In order to cover a large number of M dwarfs observed with the CARMENES instrument, the chromospheric modeling in this thesis focused on a sample of 50 M2–3 V stars and aimed at an appropriate reproduction of three chromospheric lines. These lines were the Na I D_2, Hα, and bluest Ca II IRT line, whose spectral ranges are all covered by the VIS channel of CARMENES. The atmosphere code PHOENIX was used to construct the model chromospheres. Parameterized temperature rises were attached to an underlying photosphere model appropriate for the spectral type range of the stellar sample. The created model chromospheres have linear temperature gradients in the logarithm of the column mass density. The chromospheric parameters were adjusted to simultaneously fit the considered lines. While the parameters of the lower chromosphere strongly influenced the shape of the Na I D_2 and Ca II IRT lines, the Hα line particularly depended on the parameters of the upper chromosphere and transition region. This is in agreement with the line formation regions of the average quiet Sun derived with the VAL C model. Inactive stars in the sample could be adequately fitted by single-model fits exhibiting a temperature gradient that is steeper in the lower than in the upper chromosphere. To obtain all three lines in emission, it was necessary to design models with steeper temperature gradients in the upper chromosphere than in the lower chromosphere. Furthermore, to adequately fit the active stars in the stellar sample, linear-combination fits consisting of one inactive and one active model component had to be applied. From this approach, it was also possible to derive surface filling factors. In the linear-combination fits of the active stars, the inactive components still covered the majority of the stellar surfaces. Applying the linear-combination method to all stars showing variability yielded an increase of the active component with increasing activity states in general.

On the basis of the model set created in the first publication, the second step was to investigate how the He I IR line behaves with regard to the activity state and to draw conclusions on the responsible line formation mechanisms. To simulate different activity states of prescribed chromospheric structures, two previous best-fit models of inactive stars were modified by shifting the whole temperature profile in column mass density. With this approach the previous model set was amended to enable the investigation of the formation mechanisms of the He I IR line. Due to the fact that PHOENIX calculates the EUV radiation within a model computation, the strength of the He I IR line, as given by the pseudo-equivalent width, could be investigated as a function of the integrated EUV flux related to the bolometric flux. The respective analysis of nonflaring models and new computed model series simulating different activity states revealed strengthened line depths with slowly increased EUV radiation for the most inactive models. The modeled He I IR line approached the highest line depth of about 350 mÅ. This measurement of the upper limit of the He I IR line absorption is in agreement with the highest observed line depth of the whole CARMENES M-dwarf survey by Fuhrmeister et al. (2019). For even higher activity states, the EUV radiation further increases while the He I IR line starts to fill in. The deepening of the line for the inactive models indicates a strengthening of the PR mechanism while exceeding the point of highest line absorption hints at an increased contribution of the collisional excitation mechanism to the line formation.

The results of the present thesis show that one-dimensional modeling is capable of adequately reproducing observed chromospheric lines for different activity states. This fact indicates that one-dimensional modeling of chromospheres gives an at least time-averaged impression of the chromospheric temperature structure. Furthermore, chromospheric line modeling, such as carried out for the He I IR line in this thesis, offers the possibility to study line formation mechanisms.

4.2 Outlook

There are further problems and questions arising from the one-dimensional chromospheric modeling conducted in this thesis. I address some of these in the following.

Investigations of other M dwarfs

Since modeling the M-dwarf range M2 – M3 V yielded appropriate results in the examined chromospheric lines, this study could be extended to other M-dwarf subtypes. Adjusting the VAL C-like structure adequately reproduced the lines of the inactive M dwarfs, therefore the more inactive M-subtype range, that is, earlier than M2, may be expected to exhibit similar temperature structures in the chromosphere. However, the structural parameters would have to be carefully adjusted to fit the considered lines altogether. On the other hand, the active stars required linear combinations of two model components, the active one of which tended to deviate from the VAL C-like structure. This indicates that later M dwarfs will presumably come along with more complexity than in the case of inactive stars.

Partial frequency redistribution

Recent PHOENIX studies predicting the radiation from the EUV range in M dwarfs investigated PRD treatment and showed its influence on the resonance lines of Lyα (Peacock et al. 2019a), Ca II K, and Mg II k (Peacock et al. 2019b). A PRD treatment influences the coherent scattering, which in turn significantly contributes to the formation of resonance lines. Especially, the wings of the lines turned out to be affected by including PRD. For instance, the Ca II K continuum increased in comparison to the CRD treatment, while the total line flux clearly declined. Treating the Ca II K line in PRD worsened the model prediction of the observed line, while the CRD model better reproduced the depicted observation, although the observed line was broader and stronger. Due to interstellar contamination of the observations in the UV range, model comparisons in Lyα and Mg II k appeared difficult to monitor. Significant effects assuming PRD on the UV continuum were only found for Lyα that may consequently alter the shape of other lines depending on UV irradiation. Thus, it may be worthwile to also test the PRD treatment for models created within this thesis.

Three-dimensional chromosphere models

Chromospheres are highly heterogeneous and three-dimensional models can enable investigations of structured chromospheres. There occasionally exist three-dimensional models capable of resolving the structure of the modeled stars. For instance, Wedemeyer et al. (2004) simulated the three-dimensional atmosphere of the Sun using the CO^{5}BOLD code. This atmosphere model ranges from the upper convection zone to the middle chromosphere. Because of high computational costs, the model was computed assuming a grey (frequency independent) LTE atmosphere. In this model, acoustic waves are formed in the convection zone and rise up to the chromosphere, where they cause a heterogeneous structure. The modeled solar chromosphere exhibits cold as well as hot regions, which therefore indicates that an averaged temperature rise rather constitutes a one-dimensional simplification than the true structure of the atmosphere.

Wedemeyer et al. (2013) computed chromosphere models for analogues of the M dwarf AD Leo with different magnetic fields by using the CO^{5}BOLD code. Creating synthetic intensity maps (e. g., of the Ca II K line) revealed a complex and heterogeneous surface structure of this type of an M dwarf. On the basis of a snapshot of a CO^{5}BOLD model of AD Leo from Wedemeyer et al. (2013), De Gennaro Aquino (2016) computed a three-dimensional PHOENIX chromosphere model taking into account abundant species in NLTE. Because of decreasing density and thus increasing importance of radiative rates, an NLTE treatment was found to be essential in simulating the upper atmosphere. A three-dimensional model grid would produce more realistic models and enable time resolved investigations. This procedure may thus give a precise insight into the actual resolved atmospheric structure of M dwarfs. However, it is time consuming with current facilities to compute three-dimensional models since such a model requires computation time of the order of millions of CPU hours. Therefore, one-dimensional chromosphere models are still useful to generate average pictures for samples of stars.

Chromospheric activity in observations

The new ground based instrument Echelle SPectrograph for Rocky Exoplanets and Stable Spectroscopic Observations (ESPRESSO; Pepe et al. 2014) at the European Southern Observatory Very Large Telescope recently started its observations. It operates in the wavelength range from 3800 Å to 7880 Å, and provides high-precision radial velocity measurements of the order of $10\,\mathrm{cm\,s^{-1}}$. ESPRESSO is dedicated to the search of rocky exoplanets in the habitable zones of nearby dwarf stars of spectral types G to M. Although the main focus is a radial velocity survey of only quiet stars, the activity-induced radial velocity jitter, albeit small for this sort of stars, may still hamper the search for exoplanets orbiting them (e. g., Oshagh et al. 2017). Activity-related modeling may thus help to extract planetary signals in stellar observations and to reveal especially low-mass exoplanets.

With respect to observations of interactions between active stars and the exoplanets orbiting them, the launch of the new space telescope Star-Planet Activity Research CubeSat (SPARCS; Ardila et al. 2018) may give fundamental new insights into the impacts of stellar activity on the habitability of these planets. SPARCS has a 9-cm telescope and two photometric UV detectors. The detectors operate in the near- and far-UV range with central wavelengths of 2800 Å and 1620 Å, respectively. Therefore, the wavelength bands contain indicators from the chromosphere and transition region. It is planned to observe short- and long-term variability and study quiescent and flaring states of M dwarfs in the spectral range of M0 – M6. If this mission is successful, it will reveal realistic limitations on the habitability of exoplanets in the habitable zones of M-dwarf stars and will also provide more comprehensive data for chromospheric modeling.

References

Allard, F. & Hauschildt, P. H. 1995, ApJ, 445, 433

Alonso-Floriano, F. J., Morales, J. C., Caballero, J. A., et al. 2015, A&A, 577, A128

Amado, P. J. & CARMENES Consortium. 2017, in Highlights on Spanish Astrophysics IX, ed. S. Arribas, A. Alonso-Herrero, F. Figueras, C. Hernández-Monteagudo, A. Sánchez-Lavega, & S. Pérez-Hoyos, 599–609

Andretta, V. & Jones, H. P. 1997, ApJ, 489, 375

Anglada-Escudé, G., Amado, P. J., Barnes, J., et al. 2016, Nature, 536, 437

Ardila, D. R., Shkolnik, E., Scowen, P., et al. 2018, arXiv e-prints, arXiv:1808.09954

Arlt, R. 2011, Astronomische Nachrichten, 332, 805

Avrett, E. H. & Loeser, R. 1992, Astronomical Society of the Pacific Conference Series, Vol. 26, The PANDORA Atmosphere Program (Invited Review), ed. M. S. Giampapa & J. A. Bookbinder, 489

Ayres, T. R. 1979, ApJ, 228, 509

Ayres, T. R., Marstad, N. C., & Linsky, J. L. 1981, ApJ, 247, 545

Babcock, H. W. 1961, ApJ, 133, 572

Balmer, J. J. 1885, Annalen der Physik, 261, 80

Beckers, J. M. 1972, ARA&A, 10, 73

Benz, A. O. 2017, Living Reviews in Solar Physics, 14, 2

Berdyugina, S. V. 2005, Living Reviews in Solar Physics, 2, 8

Bettex, A. 1965, The Discovery of Nature (Simon and Schuster)

Böhm-Vitense, E. 1958, ZAp, 46, 108

Bohr, N. 1913, Philosophical Magazine, 26, 1

Boltzmann, L. 1884, Annalen der Physik, 258, 291

Caballero, J. A., Cortés-Contreras, M., Alonso-Floriano, F. J., et al. 2016a, in 19th Cambridge Workshop on Cool Stars, Stellar Systems, and the Sun (CS19), 148

Caballero, J. A., Guàrdia, J., López del Fresno, M., et al. 2016b, in Proc. SPIE, Vol. 9910, Observatory Operations: Strategies, Processes, and Systems VI, 99100E

Carlsson, M. & Stein, R. F. 1992, ApJ, 397, L59

Carlsson, M. & Stein, R. F. 1995, ApJ, 440, L29

Cincunegui, C., Díaz, R. F., & Mauas, P. J. D. 2007, A&A, 461, 1107

Cram, L. E. & Mullan, D. J. 1979, ApJ, 234, 579

Cranmer, S. R. 2009, Living Reviews in Solar Physics, 6, 3

De Gennaro Aquino, I. 2016, PhD thesis, University of Hamburg

Del Zanna, G. & Mason, H. E. 2018, Living Reviews in Solar Physics, 15, 5

Dirac, P. A. M. 1928, Proceedings of the Royal Society of London Series A, 117, 610

Eversberg, T. & Vollmann, K. 2015, Spectroscopic Instrumentation: Fundamentals and Guidelines for Astronomers

Falchi, A. & Mauas, P. J. D. 1998, A&A, 336, 281

Fontenla, J. M., Linsky, J. L., Witbrod, J., et al. 2016, ApJ, 830, 154

Foukal, P. V. 2004, Solar Astrophysics, 2nd, Revised Edition

Fraunhofer, J. 1817, Annalen der Physik, 56, 264

Freytag, B., Steffen, M., & Dorch, B. 2002, Astronomische Nachrichten, 323, 213

Freytag, B., Steffen, M., Ludwig, H. G., et al. 2012, Journal of Computational Physics, 231, 919

Fröhlich, C. 2002, Advances in Space Research, 29, 1409

Fuhrmeister, B. 2005, PhD thesis, University of Hamburg

Fuhrmeister, B., Czesla, S., Hildebrandt, L., et al. 2019, A&A, 632, A24

Fuhrmeister, B., Schmitt, J. H. M. M., & Hauschildt, P. H. 2005, A&A, 439, 1137

Giampapa, M. S., Worden, S. P., & Linsky, J. L. 1982, ApJ, 258, 740

Gillon, M., Jehin, E., Lederer, S. M., et al. 2016, Nature, 533, 221

Gizis, J. E., Reid, I. N., & Hawley, S. L. 2002, AJ, 123, 3356

Goldberg, L. 1939, ApJ, 89, 673

Gomes da Silva, J., Santos, N. C., Bonfils, X., et al. 2011, A&A, 534, A30

Gustafsson, B., Bell, R. A., Eriksson, K., & Nordlund, A. 1975, A&A, 500, 67

Hale, G. E. & Ellerman, F. 1904, ApJ, 19, 41

Hauschildt, P. H. 1992, J. Quant. Spectr. Rad. Transf., 47, 433

Hauschildt, P. H. 1993, J. Quant. Spectr. Rad. Transf., 50, 301

Hauschildt, P. H., Allard, F., & Baron, E. 1999, ApJ, 512, 377

Hauschildt, P. H. & Baron, E. 1999, Journal of Computational and Applied Mathematics, 109, 41

Heisenberg, W. 1925, Zeitschrift fur Physik, 33, 879

Henry, T. J., Jao, W.-C., Subasavage, J. P., et al. 2006, AJ, 132, 2360

Hintz, D., Fuhrmeister, B., Czesla, S., et al. 2019, A&A, 623, A136

Hintz, D., Fuhrmeister, B., Czesla, S., et al. 2020, arXiv e-prints, arXiv:2005.06246

Houdebine, E. R., Mullan, D. J., Bercu, B., Paletou, F., & Gebran, M. 2017, ApJ, 837, 96

Howard, W. S., Tilley, M. A., Corbett, H., et al. 2018, ApJ, 860, L30

Hubeny, I. & Mihalas, D. 2014, Theory of Stellar Atmospheres

Huggins, W. & Miller, W. A. 1864, Philosophical Transactions of the Royal Society of London Series I, 154, 413

Hussain, G. A. J. 2011, Astronomical Society of the Pacific Conference Series, Vol. 447, Magnetic Braking in Convective Stars, ed. L. Schmidtobreick, M. R. Schreiber, & C. Tappert, 143

Husser, T.-O., Wende-von Berg, S., Dreizler, S., et al. 2013, A&A, 553, A6

Kasting, J. F., Whitmire, D. P., & Reynolds, R. T. 1993, Icarus, 101, 108

Kirchhoff, G. 1860, Annalen der Physik, 185, 275

Kirchhoff, G. & Bunsen, R. 1860, Annalen der Physik, 186, 161

Kopparapu, R. K., Ramirez, R., Kasting, J. F., et al. 2013, ApJ, 765, 131

Kron, G. E. 1952, ApJ, 115, 301

Kuridze, D., Henriques, V., Mathioudakis, M., et al. 2015, ApJ, 802, 26

Kurucz, R. L. 1970, SAO Special Report, 309

Labrosse, N. & Gouttebroze, P. 2001, A&A, 380, 323

Leighton, R. B. 1959, ApJ, 130, 366

Linsky, J. L. 1980, ARA&A, 18, 439

Linsky, J. L. 1985, Sol. Phys., 100, 333

Linsky, J. L. 2017, ARA&A, 55, 159

Lockwood, G. W., Skiff, B. A., & Radick, R. R. 1997, ApJ, 485, 789

Lorrain, P. & Koutchmy, S. 1996, Sol. Phys., 165, 115

Mauas, P. J. D. 2000, ApJ, 539, 858

Mauas, P. J. D. & Falchi, A. 1994, A&A, 281, 129

Mauas, P. J. D. & Falchi, A. 1996, A&A, 310, 245

Mayor, M. & Queloz, D. 1995, Nature, 378, 355

Mestel, L. 1968, MNRAS, 138, 359

Milkey, R. W., Heasley, J. N., & Beebe, H. A. 1973, ApJ, 186, 1043

Mittag, M., Schmitt, J. H. M. M., & Schröder, K.-P. 2013, A&A, 549, A117

Nagel, E. 2019, PhD thesis, University of Hamburg

Nagel, E., Czesla, S., Schmitt, J. H. M. M., et al. 2019, A&A, 622, A153

Newton, I. 1704, Opticks (Dover Press)

Nortmann, L., Pallé, E., Salz, M., et al. 2018, Science, 362, 1388

Oshagh, M., Santos, N. C., Figueira, P., et al. 2017, A&A, 606, A107

Parker, E. N. 1955a, ApJ, 122, 293

Parker, E. N. 1955b, ApJ, 121, 491

Passegger, V. M., Reiners, A., Jeffers, S. V., et al. 2018, A&A, 615, A6

Passegger, V. M., Schweitzer, A., Shulyak, D., et al. 2019, A&A, 627, A161

Pauli, W. 1925, Zeitschrift fur Physik, 31, 765

Peacock, S., Barman, T., Shkolnik, E. L., Hauschildt, P. H., & Baron, E. 2019a, ApJ, 871, 235

Peacock, S., Barman, T., Shkolnik, E. L., et al. 2019b, ApJ, 886, 77

Pepe, F., Molaro, P., Cristiani, S., et al. 2014, Astronomische Nachrichten, 335, 8

Pizzolato, N., Maggio, A., Micela, G., Sciortino, S., & Ventura, P. 2003, A&A, 397, 147

Planck, M. 1901, Annalen der Physik, 309, 553

Planck, M. & Masius, M. 1914, The Theory of Heat Radiation (Blakiston)

Pradhan, A. K. & Nahar, S. N. 2011, Atomic Astrophysics and Spectroscopy (Cambridge University Press)

Quirrenbach, A., Amado, P. J., Ribas, I., et al. 2018, in Society of Photo-Optical Instrumentation Engineers (SPIE) Conference Series, Vol. 10702, 107020W

Radick, R. R., Lockwood, G. W., Skiff, B. A., & Baliunas, S. L. 1998, ApJS, 118, 239

Rauscher, E. & Marcy, G. W. 2006, PASP, 118, 617

Reiners, A., Zechmeister, M., Caballero, J. A., et al. 2018, A&A, 612, A49

Ribas, I., Tuomi, M., Reiners, A., et al. 2018, Nature, 563, 365

Robrade, J. & Schmitt, J. H. M. M. 2005, A&A, 435, 1073

Rutten, R. J. 2003, Radiative Transfer in Stellar Atmospheres

Rydberg, J. R. 1893, Annalen der Physik, 286, 625

Salz, M., Czesla, S., Schneider, P. C., et al. 2018, A&A, 620, A97

Sanz-Forcada, J. & Dupree, A. K. 2008, A&A, 488, 715

Schatzman, E. 1962, Annales d'Astrophysique, 25, 18

Schmitt, J. H. M. M., Fleming, T. A., & Giampapa, M. S. 1995, ApJ, 450, 392

Schmitt, J. H. M. M. & Liefke, C. 2004, A&A, 417, 651

Schöfer, P., Jeffers, S. V., Reiners, A., et al. 2019, A&A, 623, A44

Schrijver, C. J. 1987, A&A, 172, 111

Schrijver, C. J., Dobson, A. K., & Radick, R. R. 1989, ApJ, 341, 1035

Schrödinger, E. 1926, Physical Review, 28, 1049

Schroeder, D. J. 1967, Appl. Opt., 6, 1976

Schroeder, D. J. 1970, PASP, 82, 1253

Schulze-Makuch, D., Méndez, A., Fairén, A. G., et al. 2011, Astrobiology, 11, 1041

Schweitzer, A., Passegger, V. M., Cifuentes, C., et al. 2019, A&A, 625, A68

Secchi, A. 1877, Le soleil, Le soleil No. Vol. 2 (Gauthier-Villars)

Segura, A., Walkowicz, L. M., Meadows, V., Kasting, J., & Hawley, S. 2010, Astrobiology, 10, 751

Sheeley, N. R., J. & Harvey, J. W. 1981, Sol. Phys., 70, 237

Short, C. I. & Doyle, J. G. 1997, A&A, 326, 287

Skumanich, A. 1972, ApJ, 171, 565

Stauffer, J. R. & Hartmann, L. W. 1986, ApJS, 61, 531

Stefan, J. 1879, Über die Beziehung zwischen der Wärmestrahlung und der Temperatur, Sitzungsberichte der Kaiserlichen Akademie der Wissenschaften in Wien (Aus der k.k. Hof-und Staatsdruckerei)

Suárez Mascareño, A., Rebolo, R., & González Hernández, J. I. 2016, A&A, 595, A12

Suárez Mascareño, A., Rebolo, R., González Hernández, J. I., & Esposito, M. 2015, MNRAS, 452, 2745

Ulmschneider, P. 1971, A&A, 12, 297

Ulmschneider, P. & Kalkofen, W. 1977, A&A, 57, 199

Valentinuzzi, M. E. 2019, IEEE Pulse, 10, 23

Vernazza, J. E., Avrett, E. H., & Loeser, R. 1981, ApJS, 45, 635

Walkowicz, L. M. & Hawley, S. L. 2009, AJ, 137, 3297

Weber, E. J. & Davis, Leverett, J. 1967, ApJ, 148, 217

Wedemeyer, S., Freytag, B., Steffen, M., Ludwig, H.-G., & Holweger, H. 2004, A&A, 414, 1121

Wedemeyer, S., Ludwig, H. G., & Steiner, O. 2013, Astronomische Nachrichten, 334, 137

Wheatley, P. J., Louden, T., Bourrier, V., Ehrenreich, D., & Gillon, M. 2017, MNRAS, 465, L74

Wien, W. 1893, Eine neue Beziehung der Strahlung schwarzer Körper zum zweiten Hauptsatz der Wärmetheorie, Sitzungsberichte der Preussischen Akademie der Wissenschaften

Wilson, O. C. 1973, Summary, Vol. 317, 305

Wilson, O. C. 1978, ApJ, 226, 379

Wood, B. E. 2004, Living Reviews in Solar Physics, 1, 2

Youngblood, A., France, K., Loyd, R. O. P., et al. 2017, ApJ, 843, 31

Zechmeister, M., Dreizler, S., Ribas, I., et al. 2019, A&A, 627, A49

Zechmeister, M., Reiners, A., Amado, P. J., et al. 2018, A&A, 609, A12

Zirin, H. 1975, ApJ, 199, L63

Acknowledgements

First of all, I would like to thank my supervisor Prof. Jürgen Schmitt for providing me the opportunity to work in his group, his great support, and many good advices throughout this work. I had a really great time as a PhD student. I would also like to thank him for giving me strength to get through the most terrible time of my life.

I gratefully thank Birgit Fuhrmeister for her great support with PHOENIX and many other things during my work.

I would also like to thank Stefan Czesla for many fruitful discussions and his great advices.

I thank Andreas Schweitzer for his help with any sort of problem with PHOENIX.

Furthermore, I would like to thank Vera Maria Passegger and Volker Perdelwitz for proofreading this thesis.

I also thank all my colleagues from the Observatory Bergedorf and the CARMENES consortium for making my time as a PhD student a really great time in my life.

I would like to dedicate this thesis to my mother Erika who sadly passed away during my time as a PhD student. I thank my parents Erika and Werner, my brother Frederik and his girlfriend Dörte, and all my friends for giving me strength and support throughout this time. Finally, I gratefully thank my girlfriend Johanna for her support and many other things.

Eidesstattliche Versicherung / Declaration on oath

Hiermit versichere ich an Eides statt, die vorliegende Dissertationsschrift selbst verfasst und keine anderen als die angegebenen Hilfsmittel und Quellen benutzt zu haben.
Die eingereichte schriftliche Fassung entspricht der auf dem elektronischen Speichermedium.
Die Dissertation wurde in der vorgelegten oder einer ähnlichen Form nicht schon einmal in einem früheren Promotionsverfahren angenommen oder als ungenügend beurteilt.

Ort, Datum

Unterschrift des Doktoranden